Scott Polar Research Institute

Quantification of the Impact of Supraglacial Lakes and Slush on Surface Energy Balance of Ice Shelves

Nivlisen Ice Shelf, East Antarctica

Naomi Lefroy

Submission for Master of Philosophy in Polar Studies
2019-2020

Contents

Statement

I confirm that the content within this MPhil Dissertation is my own work, written in my own words and involves no plagiarism. I confirm that this dissertation, at 19,782 words, does not exceed 20,000 words in length (excluding abstract, tables, figure captions and end matter, following MPhil Handbook Guidelines).

Acknowledgements

I am grateful for the support of my supervisor who helped to refine the idea for this dissertation as well as providing ongoing support through the process. I also valued the contributions of various PhD students through the process who discussed different methods with me and provided valuable advice on debugging Google Earth Engine. This dissertation would not have been possible without the generous grant provided by Dr Bratton, an Alumnus of Cambridge University.

A special mention goes to all of the other MPhil students who have made this year so enjoyable. Despite our final term being interrupted by the outbreak of COVID-19, I am very grateful for the two terms we shared in Cambridge. I would also like to thank my family and fiancé for their support and encouragement.

List of Figures

List of Tables

Abstract

Supraglacial lakes (SGLs) and slush are prevalent features of Antarctic ice shelf surface hydrology and efficiently transfer energy to the ice by melt-albedo feedbacks (Dell et al., 2020; Moussavi et al., 2020). There have been few efforts to quantify the energy exchanges between supraglacial meltwater, atmosphere, and ice (Jakobs et al., 2019), despite suggestions that low albedo surface features are melt hotspots (Miles et al., 2016). This study aims to quantify the extra energy absorbed by SGLs and slush on Nivlisen Ice Shelf (NIS), East Antarctica, over the austral summers of 2017-2020.

First, a new method is developed for defining SGL, slush, and ice extent using a Principal Components Analysis (PCA) on spectral data derived from Sentinel-2 and Landsat 8 imagery. A surface energy balance (SEB) model is developed, following Buzzard et al. (2018) and Law et al. (2020), and applied across the extracted supraglacial feature extents using Global Forecast System meteorological data.

The SEB model calculates the mean daily energy absorbed by lake and slush areas as ~ 8.7 MJ/m^2 and ~ 0.54 MJ/m^2 for the austral summers of 2017-2020. Modelled energy balance at lake and slush regions is most sensitive to incident shortwave radiation, although local ice shelf processes affect spatial variability of sensible and latent heat fluxes. The results of the SEB model are validated by comparing modelled cumulative energy absorption at SGLs with inferred energy transfer derived from SGL volume. The Nash-Sutcliffe Efficiency value of 0.922 implies that the modelled energy absorption matches the inferred dataset well. Furthermore, high agreement (62 %) between the supraglacial feature masks, produced using different satellite data, supports further use of the PCA in Antarctic hydrological research.

Overall, despite the low spatial coverage of SGLs at ~ 1.6 % of the total area, water coverage on NIS represents a substantial means of energy absorption. A significant finding of this study is that exclusion of slush in previous energy balance calculations is likely to have underestimated the net transfer of energy to Antarctic ice shelves. Total extra energy absorbed across the slush region in 2019 is equivalent to that absorbed by SGLs, suggesting that slush extent can be a significant control on energy absorption.

The confirmed significance of slush and SGLs for energy absorption, and the validity of the SEB model, support the application of methods developed in this study at pan-Antarctic scales. Quantification of the ice sheet-scale energy absorption by SGLs and slush would provide a baseline to gauge meltwater and sea level rise contribution under different atmospheric forcing projections.

1. Introduction

1.1 Rationale

Antarctic Ice Sheet (AIS) mass loss has increased over the last decade and now accounts for 0.6 mm/yr of sea level rise (Shepherd et al., 2018). Mass loss from the Greenland Ice Sheet (GrIS) dominated the cryospheric sea level contribution in the 1990s with AIS mass loss at only 40 ± 9 Gt/yr (1979–1990) (Rignot, 2019). However, both GrIS and AIS have demonstrated accelerated mass loss since 2000 with current negative mass balances of -286±20 Gt/yr and -252±26 Gt/yr respectively (Shepherd et al., 2018; Rignot, 2019). A large proportion of Antarctica's accelerated mass loss is related to the growing extent and intensity of surface meltwater production (Trusel et al., 2012; Bell et al., 2018). At present, 3-4 % of AIS experiences surface melt which is set to at least double by 2050 as atmospheric warming accelerates, firn capacity decreases through wind-driven densification (Ligtenberg, 2011), and nunatak exposure increases (Kingslake et al., 2017; Bell et al., 2018). Increasing surface melt has led to the development of pervasive surface meltwater systems which occur in a variety of forms across Antarctic ice shelves (Dell et al., 2020; Arthur et al., 2020; Moussavi et al., 2020). The development of these features emphasises the importance of developing a holistic understanding of Antarctic supraglacial hydrology in the context of anthropogenic climate change.

Improved understanding of supraglacial hydrology is critically important for constraining feedbacks between hydrology and dynamics, quantifying surface energy transfers, and projecting mass balance. The development of supraglacial hydrological systems, which favour through-ice shelf hydrofracture, may cause collapse (Glasser and Scambos, 2008), persistent acceleration, and mass loss from unbuttressed tributary glaciers (Berthier et al., 2012). Supraglacial hydrology formation and evolution can be understood by quantifying energy exchanges between the atmosphere and buttressing ice shelves (Jakobs et al., 2019). The impact of meltwater on energy balance is likely to be highest around grounding line areas of ice shelves. High net longwave radiation around nunataks, and high sensible heat transfer from adiabatic warming by katabatic and foehn winds, contribute to increased likelihood of meltwater formation at ice shelf grounding lines (Lenaerts et al., 2017; Dell et al., 2020). Blue ice, slush and supraglacial lakes (hereafter 'SGLs' or 'lakes') all have lower albedo than surrounding snow or ice and therefore enhance shortwave radiation transfer to the ice shelf (Zatko and Warren, 2015; Bell et al., 2018). These features form proximate to one another exerting a disproportionate effect on surface energy balance (SEB) despite relatively small coverage (Kingslake et al., 2017). The positive feedback between reduced albedo and increased melt makes SGLs and slush particularly significant for SEB.

Whilst previous research attributes enhanced ablation to lower albedo of surface meltwater, there have been few efforts to quantify energy exchanges between SGLs, the atmosphere, and ice (Jakobs et al., 2019; Law et al., 2020). The ways in which future warming will influence SGL evolution, and development of surface-to-bed linkages by hydrofracture, also remain poorly constrained (Leeson et al., 2015; Banwell et al. 2016; Koziol et al., 2017). Predictions that AIS surface hydrology will increasingly resemble that of Greenland (Bell et al., 2018) lack robust quantitative evidence and have understudied implications for ice sheet-wide mass loss predictions. The significance of supraglacial ice shelf features to mass balance contributes to this evident research gap.

Existing research on mass balance contribution focuses on West Antarctica and the Antarctic Peninsula, leaving major uncertainties in AIS-wide predictions of direct and committed sea level rise (e.g. Rignot et al., 2006; Berthier et al., 2012; Rott et al., 2018). To improve predictions of future ice shelf stability, AIS mass loss, and associated sea level rise, surface meltwater processes on East Antarctic ice shelves must be better understood. Satellite-based observations and previous energy balance modelling have suggested that melt in East Antarctica is currently intermittent and relatively low (Picard et al., 2007; Tedesco, 2009; Luckman et al., 2014; Kuipers Munneke et al., 2018). However, more recent studies have mapped extensive supraglacial hydrological features which form in the austral summer on East Antarctic ice shelves such as the Roi Baudouin Ice Shelf, Amery Ice Shelf, and Nivlisen Ice Shelf (Stokes et al., 2019; Arthur et al., 2020; Moussavi et al., 2020). East Antarctic ice shelves are therefore useful for considering the importance of the positive melt-albedo feedback in accelerating energy transfer to underlying ice. Nivlisen Ice Shelf (70 °S, 12 °E) is illustrative of the increasingly prevalent surface melt on the EAIS and is used in this study to develop a surface energy balance (SEB) model which quantifies extra energy absorbed by lake and slush features (Figure 1).

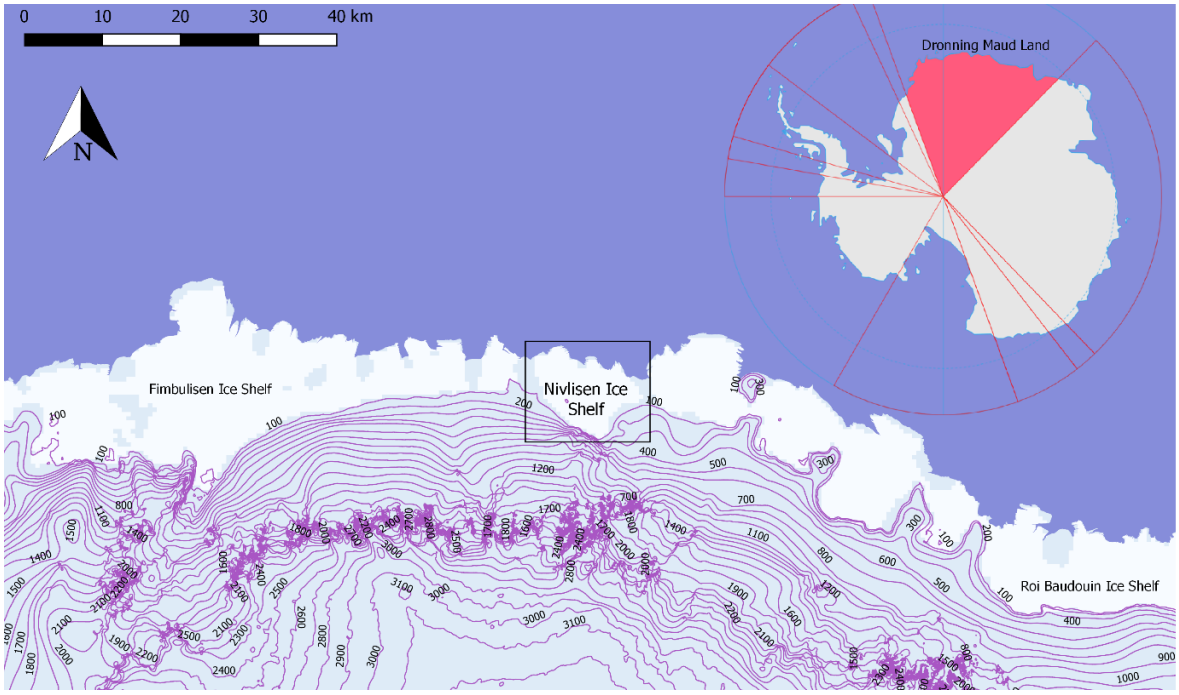

Figure 1a. Dronning Maud Land coast, with ice shelves (white) (from ALBMAP with 5km resolution) and elevation contours (RAMP2 Contours, 100m). Nivlisen Ice Shelf study area outlined in black box. Dronning Maud Land Sector, Antarctica, (top right) from Norwegian Polar Institute accessed at www.npolar.no/en/ on 23/12/19. Datasets from Quantarctica dataset accessed on 23/12/2019.

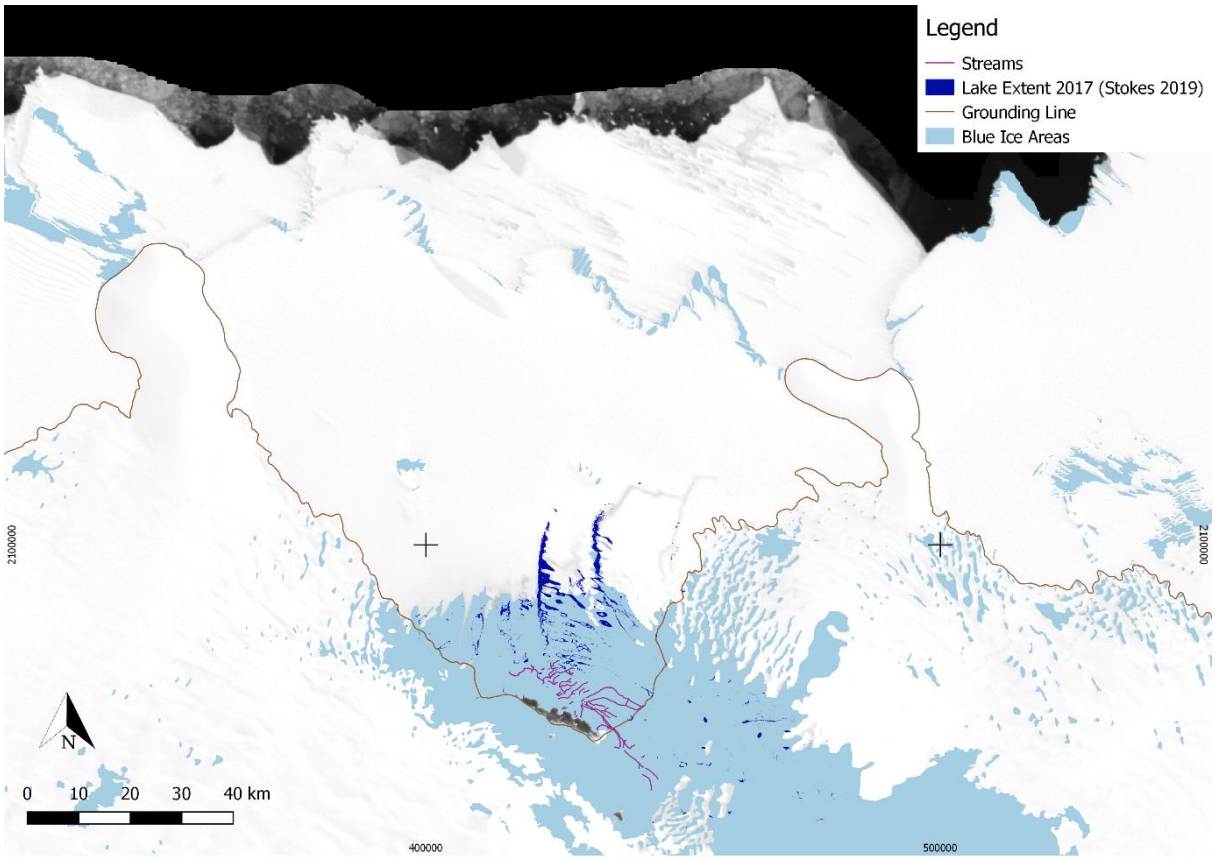

Figure 1b. Supraglacial features of Nivlisen Ice Shelf (70°S, 11°E), LIMA Mosaic Landsat imagery, 15 m resolution, false-colour, pan-sharpened, derived from bands 4, 3, 2. Tiles are mosaiced from scenes captured in 1999-2002. Blue ice (pale blue), grounding line (red) and streams (purple) determined

from Quantarctica dataset, accessed on 23/12/2019. Blue ice and stream features mapped according to Sentinel-2 image captured on 31/01/2019. Supraglacial lakes (dark blue) from Stokes et al., 2019.

This study focuses on the energy balance contribution of two supraglacial meltwater features which are extensive across Antarctic ice shelves – supraglacial lakes and slush (Buzzard et al., 2018; Bell et al., 2018; Stokes et al., 2019). Accurate delineation of supraglacial features is useful to constrain relative SEB contribution from slush and lake features, yet to be quantified on AIS (Trusel et al., 2015; Bell et al., 2018). A new method for lake classification on Nivlisen Ice Shelf is applied and a first attempt to quantify slush extent from spectral data is outlined. In light of SGL-drainage triggered ice shelf collapse (Banwell and MacAyeal, 2015) and observations of increased surface melt extent (Bell et al., 2018; Stokes et al., 2019), the SEB model developed here is a timely addition to emerging literature on AIS supraglacial hydrology.

1.2 Approach and Aims

This study aims to code a computationally efficient SEB model in Google Earth Engine (GEE) Editor to quantify the extra energy absorbed by lakes and slush on Nivlisen Ice Shelf over austral summers of 2017-2020. Near-grounding line negative mass balance of the Nivlisen Ice Shelf (70 °S, 12 °E), Dronning Maud Land, East Antarctica, is sufficient to form SGLs and is therefore suitable to test SEB model accuracy (Figure 1). If successful for Nivlisen Ice Shelf, the model has potential applicability to calculate total extra energy absorbed by surface meltwater on other Antarctic ice shelves. Accurate quantification of SGL and slush energy balance provides a baseline to gauge evolution of meltwater contribution under different radiative forcing pathways and to reduce uncertainties in sea-level rise projections.

This study makes a first step towards this by addressing the following objectives:

(1) Delineate lake and slush area of Nivlisen Ice Shelf, East Antarctica
(2) Develop a surface energy balance model (following Law et al., 2020) in Google Earth Engine
(3) Quantify extra energy absorbed by different supraglacial features on Nivlisen over austral summers of between 2017 – 2020
(4) Validate modelled energy absorption at lakes with observed lake volume between 2017 – 2020

Classification of lake and slush extent, using a Principal Component Analysis (PCA) of Landsat 8 and Sentinel-2 spectral properties in objective (1), advances previous single or band-ratio thresholding techniques (Fitzpatrick et al., 2013; Bell et al., 2017; Dell et al., 2020). The PCA identifies useful band

information which subsequently informs extraction of thresholds from spectral reflectance histograms. The SEB is applied to lake and slush extents, determined by threshold spectral reflectance values for Landsat 8 and Sentinel-2 images (Du et al., 2016). The PCA-histogram method, as it shall hereafter be referred to, is automated and considers all useful band information, minimising error and data wastage. Objective (2) adapts the one-dimensional numerical energy-balance model, GlacierLake developed by Law et al. (2020), for the GEE environment considering surface energy exchanges. GlacierLake is most sensitive to the proportion of shortwave radiation absorbed at the surface which indicates its utility for achieving objective (3).

Given that it takes 3.4 x 10^5 J/kg of latent heat to melt ice at 0 °C, the volume of liquid water on Nivlisen Ice Shelf is used to infer how much energy has been transferred to the ice shelf (Objective 4). Lake water volume is calculated using a physically-based water-depth model (Sneed and Hamilton, 2007, Tedesco et al., 2012; Pope et al., 2016). Approximating water storage in slush regions is complex given non-linear variation of snowpack porosity with several physical properties (e.g. Techel and Pielmeier, 2011; Kinar and Pomeroy, 2015). Therefore, modelled energy transfer is validated with inferred energy transfer from lake volume only. Section 1.3 outlines the justification for applying the SEB model to Nivlisen Ice Shelf, East Antarctica, as a reference case study for model development.

1.3 Reference Case Study for Model Development

Several East Antarctic ice shelves experience upwards of 60 days a year of melting, facilitating consistent SGL and slush formation around the grounding line (Kingslake et al., 2015; Lenaerts et al., 2017; Bell et al., 2018). Nivlisen Ice Shelf (NIS) is selected for the development of the SEB model as it is (i) illustrative of the increasingly prevalent surface melt on the EAIS, (ii) has large enough lakes to be detectable in satellite imagery and (iii) is close to the Novolazarevskaya Weather Station.

Nivlisen Ice Shelf (70 °S, 12 °E), Dronning Maud Land, East Antarctica, covers ~7,300 km^2 between the Djupranen and Leningradkollen ice rises (Figure 1a; Lindbäck et al., 2019). A series of smaller ice rises and rumples, proximate to the present-day ice shelf front, are thought to have a stabilising effect (Borstad et al., 2013; Holland et al., 2015). Furthermore, NIS has been relatively protected from thinning by basal melt due to the bathymetric Astrid ridge which diverts warm circumpolar deep water into the Weddell Gyre (Thompson et al., 2014). The present stability of NIS is of significance given that it buffers a ~27,700 km^2 drainage basin with a potential global sea level rise of 8 cm (Rignot et al., 2013).

NIS has large surface mass balance transitions from negative mass balance at the grounding line to 1.8 ± 0.3 Gt/yr (1979–2010) near the ice front (Horwath et al., 2006). Near the grounding line, ~1,200 km^2 of blue ice and the Shirmacheroasen nunataks lower albedo and enhance ablation sufficiently to form SGLs and streams that occasionally drain into crevasses (Figure 1b; Horwath et al., 2006; Kingslake et al., 2015). Favourable conditions for the formation of SGLs and slush on NIS are also generated by foehn winds warming the ice shelf surface (Matsuoka et al., 2015). Foehn winds are warm downslope winds in the lee of topography which flush away cool air and generate high melt rates, as observed on Larsen C (Kuipers Munneke et al., 2012a). The ice surface slopes of 9°, calculated using REMA DEM from the EAIS continental plateau towards the Dronning Maud coast, are sufficiently steep to drive foehn winds (Howat et al., 2019). These conditions for generating surface melt are also present at other ice shelves in Dronning Maud Land. Therefore, NIS is used as an indicator of the future supraglacial hydrology of East Antarctic ice shelves.

Despite the importance of supraglacial water storage on the ice shelves for direct (meltwater runoff) and indirect (accelerated tributary glaciers after ice shelf collapse) mass loss, few studies have investigated implications of Antarctic supraglacial hydrological systems (Langley et al., 2016; Bell et al., 2018; Dell et al., 2020; Moussavi et al., 2020). The following section outlines previous research which has contributed to this growing area of understanding. Current knowledge of Antarctic supraglacial hydrology will be outlined before previous methods for supraglacial feature delineation and SEB modelling are evaluated.

2. Literature Review

2.1 Theory

The nature of supraglacial hydrology is determined by the energy available for melt (sum of radiative, convective, and conductive heat fluxes) and the meltwater pathway across the ice sheet (Figure 2). The end-member state of meltwater, its location and permanency, is significant for mass redistribution, ice dynamics, and contribution to sea level rise (Bell et al., 2018). Where there is high porosity unsaturated firn, meltwater can percolate to form slush, or refreeze within the upper ice shelf, creating ice lenses (Alley et al., 2019). Where the firn pack is already saturated, meltwater can flow laterally or form ponds in topographic depressions (Dell et al., 2020). Meltwater retained on the ice shelf surface generates extra loading, with implications for the stress regime and enhanced solar radiation absorption (Banwell and MacAyeal, 2015; Gardner and Sharp, 2010). Meltwater also accumulates in crevasses, thereby increasing hydrostatic pressure in the crevasse tip, facilitating further fracture propagation and increasing vulnerability to ice shelf collapse (Van der Veen, 2007). This process of hydrofracturing is a precursor to Antarctic ice shelf disintegration as demonstrated by the Larsen B collapse in March 2002 (Rignot et al., 2004; Glasser and Scambos, 2008). Therefore, surface melt accumulation contributes to multiple positive feedback processes which play a crucial role in the ice shelf hydrological system.

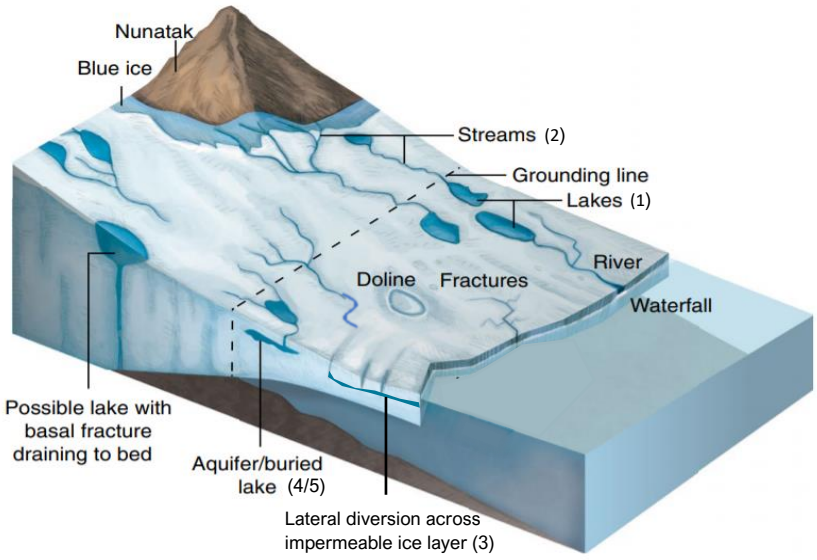

Figure 2. Typical supraglacial features and transport processes on an ice shelf. (1) Accumulation as supraglacial (SGL) lakes (Selmes et al., 2011; Banwell et al., 2013); (2) supraglacial run off (Bell et al., 2017; Smith et al., 2015); (3) snowpack percolation and lateral diversion (Chandler et al., 2013); (4) snowpack percolation and storage in firn aquifers (Forster et al., 2014), or subsurface lakes (Lenaerts et al., 2016); (5) snowpack percolation and refreezing (Harper et al., 2012). Dolines are locally uplifted, empty depressions, interpreted as evidence of surface lakes that have drained through ice shelves via ice fractures. Adapted from Bell et al., 2018.

In contrast to the extensive research in Greenland (Selmes, 2011; Leeson et al., 2012; Fitzpatrick et al., 2014), there are no comprehensive observations of SGLs on a pan-Antarctic scale. A recent regional study uses Sentinel-2A and Landsat 8 to capture the first consistent observations of East Antarctic SGLs which form in clusters near the grounding line (Stokes et al., 2019). Grounding line lake clustering may be explained by the lower elevation and removal of snow cover by katabatic winds, enhancing localised albedo-driven melt (Langley et al., 2016). Whilst ~85 % of Antarctic SGLs form in low elevation (<100 m) and low slope (<1 °) regions, they can exist 500 km inland and at elevations of >1,500 m (Trusel et al., 2015) due to proximity to low albedo nunataks (Bell et al., 2018). Whilst the current distribution of Antarctic SGLs has not been systematically documented to the same extent as GrIS SGLs, implications of the presence of supraglacial melt must be considered.

Supraglacial lakes form in regions of highest surface melt during summer months and pool in topographic depressions (Lenaerts et al., 2017). Depressions form on floating ice in relation to processes including basal crevassing, grounding-line flexure, and incomplete rebound from previous lake drainage events (Banwell and MacAyeal, 2015). Relative uniformity of depressions on floating regions indicates that lakes are formed by similar magnitudes of flexure forces (Banwell et al., 2014). Ice-shelf slopes of approximately 10^{-4} (equivalent to 5 m vertical change across 50 km) are not conducive to large cross-shelf transport suggesting that ice shelf SGLs predominantly grow *in situ* by albedo-melt feedbacks (Banwell et al., 2014). Quantifying the energy absorbed at SGLs on ice shelves is essential for predictions of lake growth and evolution.

Supraglacial lakes present a mechanism of energy transfer from the atmosphere to the ice which is poorly studied. SGLs release heat to warm underlying ice, even as surface energy input decreases at the end of the melt season, with implications for ice rheology and fracture mechanics (Koenig et al., 2015). Such cryo-hydrologic warming serves as a source of latent heat that contributes to surface energy balance, as well as heat transfer through the ice shelf (Phillips et al., 2010). However, incident solar radiation is the largest contributor to austral summer energy balance which generates melt (van den Broeke et al., 2011; Law et al., 2020). Summer melt effectively stores excess solar energy as liquid water which later supplies latent heat to underlying ice in autumn and winter via refreezing (Jakobs et al., 2019; Arthur et al., 2020).

SGLs have lower albedo than surrounding snow or ice and are therefore assumed to become hotspots of enhanced melting (Miles et al., 2016; Shukla et al., 2018). The melt-albedo positive feedback is originally driven by meltwater refreezing in the snowpack which generates larger grains (~1.0 mm) than new snow (~0.1 mm). Larger grain size snow reduces backscattering of photons, and

therefore albedo, especially for light of near infrared wavelengths (Wiscombe and Warren, 1980; Jakobs et al., 2019). Increased absorption of incoming radiation facilitates greater energy transfer to the ice shelf surface and therefore generates more melt. The strength of the feedback is likely to be dependent on the intensity and duration of melt in relation to fresh snowfall events. Jakobs et al. (2019) make a first attempt to model the melt-albedo feedback at Neumayer station (EAIS) and confirm that, without accounting for this positive feedback, total melt would be 3 times lower. Quantification of the energy balance contribution of supraglacial features is essential for confirming the significance of the melt-albedo feedback.

Implications of lower albedo SGLs for energy exchanges are conceptually included in previous mass-balance studies. A one-dimensional model developed for GrIS demonstrates that subaqueous lake-bottom ablation is enhanced by 110-170 % (1991-2001) compared to bare ice ablation (Luthje et al., 2006). Supraglacial ponds on mountain glaciers are modelled to efficiently convey atmospheric energy to the interior of glaciers and rapidly promote the downwasting process (Miles et al., 2016). Ablation rates at, and proximate to, SGLs on mountain glaciers are typically one or two orders of magnitude greater than sub-debris ice melt rates, implying that SGLs are melt hotspots for debris-covered glaciers (Benn et al., 2012). Miles et al. (2016) developed a free-convection model to quantify the extra amount of energy transferred by a pond on Lirung Glacier, Nepal. Sufficient energy is transferred to melt 38.4 m^3/day of additional ice which is expected to cause significant subsidence of the glacier surface and erode the englacial drainage system (Miles et al., 2016). Whilst it is assumed that SGLs on the AIS will have similarly significant implications for mass loss, this is yet to be modelled and quantified.

Much of the literature which emphasises the importance of surface lakes for energy balance has been conducted on Arctic sea ice (e.g. Pirazzini, 2009; Flocco et al., 2012). Prolific lake formation on Arctic sea ice is confirmed by SHEBA (Surface HEat Budget of the Arctic) to have a significant effect on overall SEB (Perovich et al., 2007). The proportion of solar energy absorbed by sea ice over the melt season is strongly related to date of melt onset (Perovich et al., 2007). Under the Community Climate System Model 4, melt ponds across Arctic sea ice contribute an extra 10 W/m^2/day over the month of July (Holland et al., 2010). Although the direct radiative effects of ponds are proportionally small (~1.1W/m^2 over each lake), modification of surface albedo by a positive feedback generates a net 10 W/m^2 response. The radiative effects of melt ponds in a warming climate point to the importance of developing models capable for accurate simulation of the melt-albedo feedback. Predictions of expanding lake extent on ice sheets under warming atmospheric temperatures indicate that future SEB models will be inaccurate without a parameterisation of the extra energy contributed by surface meltwater.

Whilst existing literature demonstrates the importance of lakes for local energy balance, estimates of the impact of reduced albedo on *overall* ice shelf energy budget are suggested to be small due to low spatial coverage (Tedesco et al., 2012; Poinar et al., 2015; Law et al., 2020). Given that lakes' minimum albedo (when they are deepest) is obtained towards the end of the melt season when incoming shortwave radiation flux is waning, the enhanced ablation is constrained (Leeson et al., 2015). Therefore, many numerical models implicitly discount the melt-albedo feedback (e.g. Van den Broeke et al., 2008; Ettema et al., 2010). For example, Leeson et al. (2015) simulated that, by 2100, the increase in volume of surface melting across the GrIS would reach a modest upper limit of 6.61–8.54 Gt/yr – only double the SGL volume in 2015. They proposed that frequent lake drainages limit the impact of the melt-albedo feedback on ice-sheet mass balance and thus discounted variation in surface albedo. To resolve questions of the significance of the melt-albedo feedback, robust quantitative evidence of extra energy transferred at SGLs on AIS is required.

Slush is another pervasive supraglacial feature on Antarctic ice shelves (Buzzard et al., 2018) which has a lower albedo than that of snow/ice and should be accounted for in SEB modelling (Rosel et al., 2011). Slush is a prolific transitional material found in the ablation zone which forms as porous firn becomes saturated by run-off or as snow is deposited in open water (Kuipers Munneke et al., 2014; Zatko and Warren, 2015). Given high liquid water content, slush is predicted to have similarly low visible-near infrared (VNIR) spectral reflectance as SGLs (Rosel and Kaleschke, 2011). Yang and Smith (2012) indicate that previous spectral classifications only partially discern slush from lakes and may fail in saturated slush areas. Slush extent must be determined both for accurate lake delineation but also to allow quantification of slush SEB contribution.

Broad spatial coverage of slush on ice shelves was documented by the first Antarctic explorers as "thaw-water" which made traverse difficult (T.W.E. David, 1909; Bell et al., 2018). Despite the prevalence and persistence of slush, little research has been conducted to consider its implications for the broader ice shelf system. Slush areas are of interest for quantifying SEB contribution, in isolation and in relation to SGLs (Kingslake et al., 2017), as well as predicting ice shelf flexure response (MacAyeal and Sergienko, 2013; Leeson et al., 2020). It is characteristic for SGLs on Antarctic ice shelves to form over regions of water-saturated slush (Buzzard et al., 2018). Not only is slush a precursor for lake formation, but the co-existence of these low-albedo supraglacial features may generate a disproportionate effect on mass loss (Kingslake et al., 2017).

Given proximity of SGLs, slush, and nunataks on Antarctic ice shelves, it is hypothesised that ice shelf thinning generates a positive nunatak-melt-thinning feedback (Kingslake et al., 2017). As ice shelves thin, greater proportions of exposed rock enhance melt due to lower albedo. Enhanced surface run-

off increases thinning and the likelihood of shelf collapse if water accesses areas vulnerable to hydrofracture (De Rydt et al., 2015). Whilst water stored in slush is unlikely to generate sufficient water pressure to drive hydrofracture, prolific slush extent enhances rock-melt-thinning feedbacks and increases sites favourable for SGL formation.

Large volumes of water stored in SGLs and slush have implications not only for enhanced energy absorption but also for ice shelf stability. Evolution of supraglacial systems which efficiently transport meltwater off ice shelves may reduce instability, as seen on Nansen Ice Shelf (Bell et al., 2018). Contrastingly, a pan-Antarctic survey of surface drainage systems from visible satellite imagery (1947 – 2015) suggests that accumulation of meltwater can trigger ice shelf collapse (Kingslake et al., 2017). SGL filling and drainage induces localised flexure, generating fractures and triggering neighbouring lake drainage in a chain reaction (Banwell and MacAyeal, 2015). The near-synchronous drainage of ~3,000 melt ponds and subsequent collapse of Larsen B Ice Shelf a few days later, is a frequently cited example of this behaviour (Glasser and Scambos, 2008). Where water is routed into upper firn, firn permeability will control the extent of lateral transport relative to vertical seepage into subsurface aquifers (Kuipers Munneke et al., 2012). Surface melt delivered to impermeable ice areas is likely to run-off downslope or pool in topographic depressions. Therefore, small variability in supraglacial properties and ice shelf topography strongly impact drainage efficiency and ice shelf stability.

Extensive coverage, and relative lack of research, make EAIS lakes and slush of particular interest for quantifying energy exchanges. Quantification of the contribution of slush and SGLs to surface energy balance and prediction of long-term ice shelf stability require a robust method for delineating slush and lake extent. A variety of methods have been applied for remote supraglacial feature extraction which use data obtained from aircraft or satellites. Despite previous work to determine lake extent from spectral properties, as outlined in the following section, slush regions remain unclassified. Therefore, this study makes a first step, through development of an automated spectral classification, to delineate lake and slush extent on NIS drawing on methods previously applied in the sea ice literature (Rosel and Kaleschke, 2011; Flocco et al., 2012).

2.2 Approaches for Supraglacial Lake Identification

2.2i Remote Sensing Instruments

Satellite-based remote sensors have transformed our understanding of ice-sheet hydrology. The sensors applied in water-body extraction can be divided into optical sensors, measuring reflection of VNIR radiation, and radar, recording radio wave returns.

Space-borne radar imaging instruments are useful for detecting supraglacial hydrology given their ability to derive backscatter returns from the shallow sub-surface (Rees, 2013). Datasets from radar satellite sensors, such as RADARSAT-1 (1995-2013), can function in any lighting or cloud conditions and reliably monitor surface features over their lifetime.

Mapping of supraglacial hydrology lends itself to optical remote sensing given water's distinct VNIR spectral signature. MODIS optical data have been widely used to document lake formation and drainage given daily repeat-pass measurements, but the coarse spatial resolution (250 m) limits utility for mapping smaller lakes (Fitzpatrick et al., 2014). Landsat 8 and Sentinel-2 optical sensors have high spatial resolutions (15-30 m) and have been used to derive and validate automated lake-tracking algorithms (Williamson et al., 2017; Dell et al., 2020). Despite unequivocal utility of high-resolution optical data, image acquisition in high-latitude regions is sparse due to frequent cloudy days, low revisit times, and pixel saturation. Pixel saturation, where the incident light at a pixel causes one of the sensor channels to respond at its maximum value, prevents detection of spectral change (Zhang, 2004; Burton-Johnson et al., 2016). Given these limitations, the following section outlines approaches to maximise the utility of available satellite optical imagery using digital post-processing to ensure accurate surface feature mapping.

2.2ii Previous Methods for Supraglacial Lake Extraction from Images

Post-processing of satellite imagery is key for extracting information about supraglacial hydrology. The most common methods for extracting information about water bodies are single and band-ratio thresholds, image segmentation, and target detection methods (Jawak, 2015).

Post-processing usually involves thresholding of a distribution of image spectral reflectance across wavelengths, given differential attenuation of wavelengths in water (e.g. Selmes et al., 2011; Williamson et al., 2017). The Normalised Water Difference Index (NDWI), a ratio involving red (B4, 0.64–0.67 µm) and blue (B2, 0.45–0.51 µm) bands, is widely used to detect surface lakes (Eq. 1) (Doyle et al., 2013; Moussavi et al., 2016; Macdonald et al. 2018; Williamson et al. 2018b; Dell et al., 2020).

$$NDWI = \frac{B2 - B4}{B2 + B4} \quad (1)$$

Red and blue bands are chosen given high reflectivity of water in the blue band and the contrast between ice and water in the red band (Yang and Smith, 2012). The thresholding of the ratio of blue to red surface reflectance is used to define water-covered pixels in a scene based on the principle that red wavelengths are attenuated more strongly than blue (Box and Ski, 2007). Higher NDWI thresholds may underestimate lake extents whilst lower thresholds may incorrectly identify blue ice,

nunataks, or shadows as SGLs (Burton-Johnson, 2016). NDWI-based indices are adjustable to remove background noise, whilst not affecting the target extraction, and are computationally efficient. However, such ratios must be manually adjusted for cloud cover and to remove coastal water, which introduces subjectivity error (Pope et al., 2016). Furthermore, if the common NDWI is always used for lake extraction, a large proportion of valuable spectral data remains unused.

Given that a single spectral index does not demarcate lakes effectively in different environments, a combination of indices yields better results (Sun et al., 2012; Watson et al., 2018). For example, the red-blue NDWI is most successful for lakes on land whilst the green-NIR NDWI is most accurate for East Antarctic ice shelf features (Yang and Smith, 2012; Stokes et al., 2019). The green-SWIR NDWI is found to be a particularly successful spectral index for Sentinel-2 data, enhancing water bodies and suppressing built-up features more efficiently than red-blue NDWI (Du et al., 2016). This is related to high green band resolution (10 m) and streamlined pan-sharpening methods for downscaling the SWIR band. Testing of various spectral indices for a given study-site and satellite data is time-consuming and subject to user bias.

Accuracy of supraglacial feature extraction may be enhanced using other pixel properties in combination with spectral information (Jawak, 2015). For example, to overcome the challenges in discriminating streams from slush, a joint spectral-shape classification is applied for WorldView 3 images over Greenland's ablation zone (Yang and Smith, 2012). This joint classification procedure is 26% more accurate than NDWI classification when validated against manually digitised stream features. However, such morphological methods would be unsuccessful for slush and lake areas given lack of distinctive feature geometries.

To date, only Miles et al. (2017) have developed a method to distinguish between lake and slush regions on ice sheets. Miles et al. (2017) use an NDWI threshold to generate a binary combined lake-slush mask from Landsat 8 images. This mask was applied to Sentinel-1 radar images and histograms of backscatter across the lake-slush regions, returning a bimodal distribution which suggested a threshold value for the transition between lake to slush (Miles et al., 2017). Despite this extensive method to separate lake and slush regions, slush zones were subsequently eliminated in the analysis.

Classification techniques, developed in the sea ice literature, involve consideration of multiple bands to differentiate between surface features with similar spectral signatures whilst also accurately removing the surrounding ocean (Flocco et al., 2012). Rosel and Kaleschke (2011) extract melt ponds by performing a PCA on spectral information from MODIS data which identifies spectral bands that best resolve surface differences. The two orthogonal principal components, which describe most

dataset variability, are plotted in a new co-ordinate system to show clustering of pixels which represent melt ponds (Figure 3). However, even the automated PCA method produces a small error of 0.35% related to misclassified pixels on class edges (Rosel and Kaleschke, 2011). The trade-off between retaining all useful information and maximising computational efficiency can be balanced through the application of PCA. Therefore, this report makes a first attempt to classify lake *and* slush extents on the NIS using the PCA method outlined in Section 3.1.

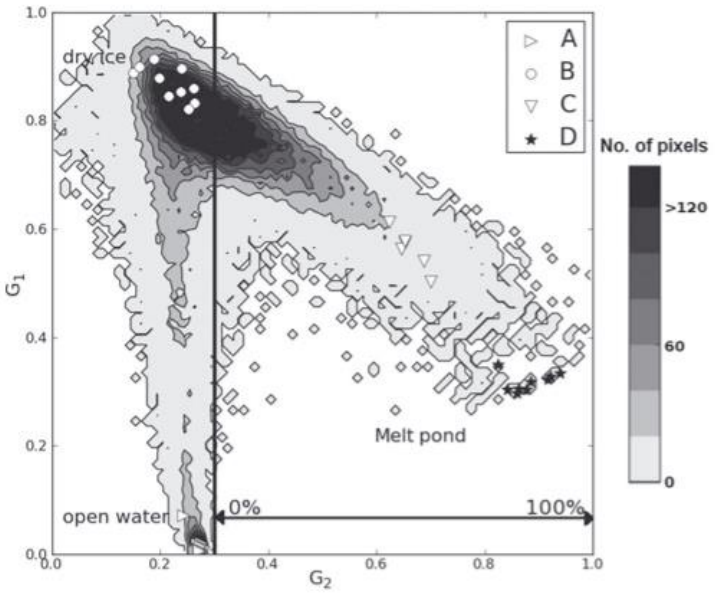

Figure 3. Extracted principal components plotted in transformed co-ordinate system to identify dataset clustering. PCA applied to Landsat 7 ETM+ scene (120° W, 80° N) from 19 July 2001 with manually delineated training pixels represented by A-D. A – open water pixels, B – dry ice, C- wet slush, D – melt ponds. Source: Rosel and Kaleschke, 2011.

2.3 Current Supraglacial Lake Energy Balance Models

The SEB model presented here draws on previous efforts but aims to improve accuracy of the inter-annually variable lake/slush extent input domain. Buzzard et al. (2018) presented a physically comprehensive model for lake development on Antarctic ice shelves accounting for firn compaction, saturation, and refreezing. Building on this, Law et al. (2020) developed the GlacierLake model which not only accounts for persistent latent heat contribution of buried lakes throughout the winter, but also has rapid execution times facilitating extensive model sensitivity testing. Results from GlacierLake are found to be most sensitive to the proportion of shortwave radiation absorbed at the surface. The model applied here simplifies the surface fluxes from Buzzard et al. (2018) and Law et

al. (2020) to maximise computational efficiency whilst retaining model sensitivity to absorbed shortwave radiation.

Considering the above, this study contributes to three current research gaps: it provides (1) a new automated method for delineation of lake and slush extent, (2) the first SEB model coded in GEE, and (3) a first quantification of extra energy contribution of lakes and slush to AIS energy balance.

The remainder of the dissertation is structured as follows:

- the PCA-histogram method for extracting lake and slush regions from Landsat 8 and Sentinel-2 imagery is explained,
- a physical description of the model is presented, outlining calculation of different energy fluxes,
- the results of the numerical implementation of the model to Nivlisen Ice Shelf are reported and,
- sensitivity and validation are performed to assess model performance and discuss applicability in future research.

3. Methods

There are three main components to the methods applied in this study: i) detecting lake and slush areas; ii) calculating surface energy balance contribution of lake and slush; and iii) validating the lake SEB using total lake volume (Figure 4). First, the selected satellite data, used as the basis for feature delineation and SEB modelling, are outlined and justified for the purposes of this study.

Figure 4. Flow chart of overall method applied in this study for quantification of energy contribution of SGL and slush areas on Nivlisen Ice Shelf.

3.1 Lake and Slush Identification

3.1i Remote Sensing Data

To produce an estimate for the slush and lake extent on East Antarctic ice shelves requires a satellite-based dataset with high-latitude coverage and sufficient spatial resolution to identify smaller lakes. On this basis, Landsat 8 and Sentinel-2 data were chosen, available in GEE as calibrated top-of-atmosphere (TOA) reflectance products.

The Multi-Spectral Instrument on Sentinel-2 provides optical imagery of high spatial (10 m) and temporal (10-day revisit) resolutions with satisfactory coverage over Antarctica (Table 1; Du et al., 2016). Sentinel-2 is the most reliable multispectral sensor at distinguishing spectral signatures of SGLs and snow, on par with high resolution sensors such as WorldView and RapidEye (Watson et al., 2018). The Sentinel-2 TOA reflectance values are divided by the quantification value of 10,000 to convert numbers into values that lie within the expected zero to one range. For the training of the new lake-slush classification developed in this study, Sentinel-2 scenes of NIS between September 2016 and March 2020 were identified in GEE (Table S1).

In the Sentinel-2 dataset, band 1 is reflected by aerosols and band 9 by atmospheric water vapour whilst band 10 identifies cirrus clouds (Konig et al., 2019). Given that bands 1, 9, and 10 are not indicative of surface characteristics, they are not considered in this study. Furthermore, a cloud mask is generated by thresholding the image property 'CLOUDY_PIXEL_PERCENTAGE' which identifies a pixel as cloudy based on the SWIR band. A 20 % cloudy pixel threshold is set to ensure that the region of interest is not obscured.

Sentinel-2 bands	Wavelength Range (µm)	Central wavelength (µm)	Resolution (m)
Band 1 Coastal aerosol	0.43 - 0.45	0.44	60
Band 2 Blue	0.45 - 0.52	0.49	10
Band 3 Green	0.54 - 0.57	0.56	10
Band 4 Red	0.65 - 0.68	0.67	10
Band 5 Vegetation red edge	0.69 - 0.71	0.71	20
Band 6 Vegetation red edge	0.73 - 0.74	0.74	20
Band 7 Vegetation red edge	0.77 - 0.79	0.78	20
Band 8 NIR	0.78 – 0.90	0.84	10
Band 8A Vegetation red edge	0.85 – 0.87	0.87	20
Band 9 Water vapour	0.93 – 0.95	0.95	60
Band 10 SWIR Cirrus	1.36 – 1.39	1.38	60
Band 11 SWIR	1.56 – 1.65	1.61	20
Band 12 SWIR	2.10 – 2.28	2.19	20

Table 1. Sentinel-2 band characteristics. The satellite carries a single multispectral instrument with 13 spectral channels which all collect data using the push-broom concept. The sensor records ten electromagnetic bands (0.494 – 0.945 µm wavelengths), a panchromatic band (0.443 – 0.496 µm), two infrared bands (1.613 – 2.202 µm) and cloud masks for opaque (QA60) and cirrus clouds (B10). Sentinel-2 satellite is part of the Earth Observation Mission developed by the European Space Agency and was launched on 23rd Jan 2015.

Landsat 8 data is used in conjunction with Sentinel-2 for: i) high cross-compatibility between satellites, ii) longer continuous data record and iii) high spatial and temporal resolution. The Operational Land Imager (OLI) sensor is an improvement on Landsat 7's Enhanced Thematic Mapper Plus (ETM+) based on radiometric resolution, signal-to-noise ratio and dynamic range (Pope et al.,

2016; Williamson et al., 2017). Landsat 8 scenes are available over the high latitude polar regions with 30 m spatial resolution and 16-day revisit interval (Roy et al., 2014). Landsat 8 OLI is used as a level-2 Top of Atmosphere reflectance (TOA) product. Pope et al. (2016) ran a sensitivity analysis of path radiance to atmospheric gases, using a radiative transfer model, and demonstrated that atmospheric correction is not required for Landsat 8 Tier 2 data. However, the TOA reflectance sensitivity is not processed for thermal bands which means these bands cannot be used for SEB calculations (Chander et al., 2009). Furthermore, bands 1, 8, and 9 describe properties not related to surface characteristics or, in the case of the panchromatic band (band 8), describe combined information from blue, green and red visible bands. Therefore, these bands are not considered for the development of the Landsat 8 PCA.

Landsat 8 scenes with < 20% cloud cover collected between November 2016 and February 2020 covering the ice shelf extent were identified in GEE (Table S2). Each downloaded Landsat scene is corrected using a cloud mask which is generated using the Simple Cloud Score Algorithm (ee.Algorithms.Landsat.simpleCloudScore) in GEE. This algorithm assigns a cloud score to individual pixels based on blue band reflectance relative to other visible bands, brightness in NIR and SWIR bands, as well as the temperature according to thermal band 10 (Hall et al., 2010).

Landsat 8 bands	Wavelength (μm)	Resolution (m)	Radiometric rescaling coefficients
Band 1 Coastal aerosol	0.43-0.45	30	0.0001
Band 2 Blue	0.45-0.51	30	0.0001
Band 3 Green	0.53-0.59	30	0.0001
Band 4 Red	0.64-0.67	30	0.0001
Band 5 Near infrared	0.85-0.88	30	0.0001
Band 6 Shortwave infrared 1	1.57-1.65	30	-
Band 7 Shortwave infrared 2	2.11-2.29	30	0.0001
Band 8 Panchromatic	0.52-0.90	15	-
Band 9 Cirrus	1.36-1.38	15	-

Table 2. Landsat 8 band characteristics. The Landsat 8 OLI multispectral instrument has improved radiometric precision over a 12 bit range. The 12 bit data is scaled to 16 bit integers and delivered as level-2 data Top of Atmosphere (TOA) reflectance. Landsat 8 data is produced by the U.S. Geological Survey (USGS) and was launched on 11th Feb 2013.

The Landsat 8 and Sentinel-2 scenes are clipped to the 1206 km^2 lake-covered region of NIS in GEE – this region will henceforth be referred to as the *study-site region* (Figure 5). All subsequent methods are applied to the study-site region unless specified otherwise. With these two datasets, input satellite imagery for the SEB model is available at least every 3-22 days over the months of November to February of 2017-2020.

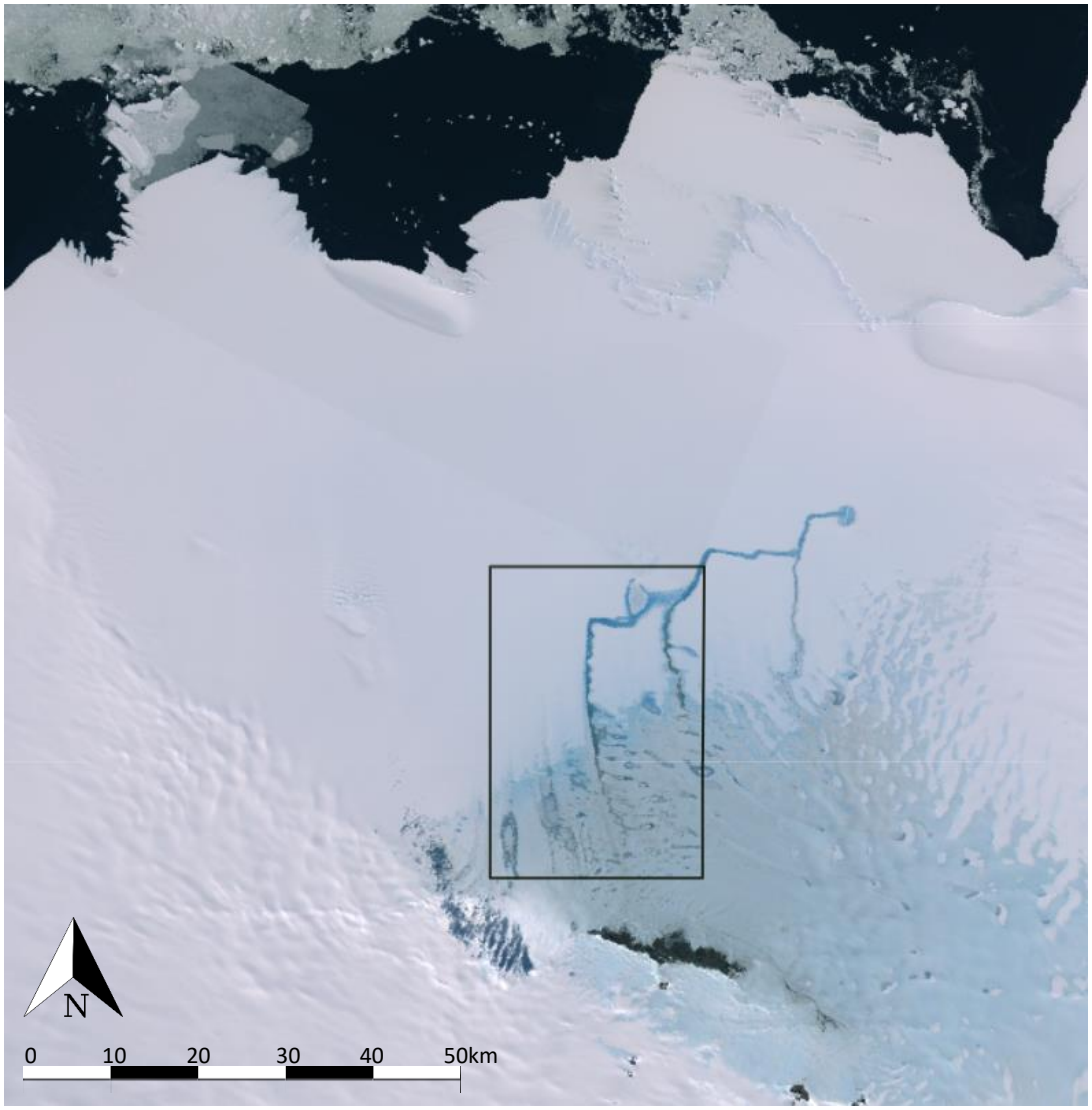

Figure 5. Study-site region (black rectangle) covering 1206 km^2 of Nivlisen Ice Shelf (70°S, 12°E). Composite of three RGB Landsat 8 images 168-109 17/02/2019, 166-110 19/02/2019 and 166-109 19/02/2019.

3.1ii Principal Components Analysis

Previous single- or ratio-based spectral band methods for determining supraglacial features are complicated by similar spectral characteristics, extensive cloud cover, and sparse satellite data availability (Miles et al., 2016). User-defined band thresholds are subject to human error, and manual delineation methods are inappropriate for classification over broad regions. Therefore, a new method is developed here using Principal Components Analysis (PCA) and histogram data to generate a multi-band classification for lake and slush extent. This is the first automated method for lake *and* slush spectral differentiation for Antarctic ice shelves.

The approach is comprised of four steps to delineate lake and slush extents by identifying which pixel properties are useful in predicting different surface characteristics. The steps are as follows:

1. Filter Sentinel-2 and Landsat 8 collections over the NIS study-site with <20% cloud cover for austral summers of 2017-2020 (Table S1-S2). Extract spectral band reflectances for the study site region across all available images.
2. Apply PCA to pixel spectral array to convert correlated data to uncorrelated composite principal components (PCs).
3. Plot histograms of spectral reflectance for best performing bands identified by PCA (Figure 6) and extract turning points in the distribution which distinguish supraglacial features (Figure 7).
4. Incorporate thresholds from best-performing bands into the GEE lake/slush extent code (Appendix – Code 2). Test the sensitivity of estimated lake and slush extents in the most recent Sentinel-2 and Landsat 8 images to ±10% variability of spectral reflectance thresholds.

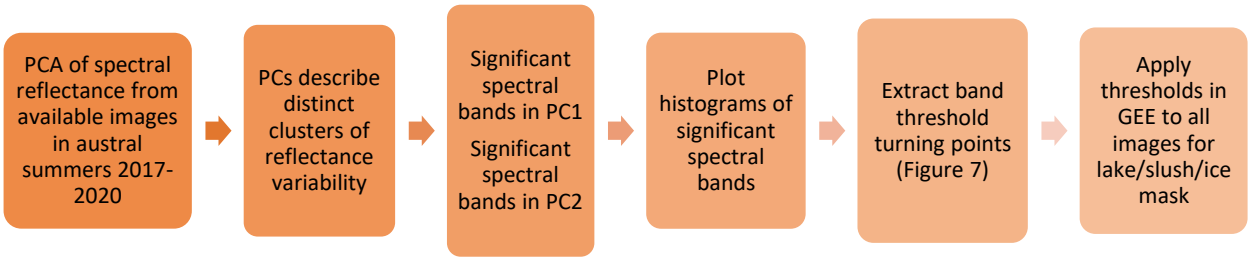

Figure 6. Workflow of the PCA-histogram method to extract spectral band thresholds for supraglacial feature mapping. PCA of spectral data from all available images in austral summers 2017-2020. Histograms of significant spectral bands are plotted based on data from most recent Landsat 8 and Sentinel-2 images. Extracted spectral thresholds are then applied to other images.

The PCA is a method of data reduction, performed in the SPSS environment, that aims to identify a small number of derived variables from a larger number of original variables (Pallant, 2005). Each input variable is a measure of pixel reflectance for each satellite spectral band with a specific range of wavelengths.

The sequence of steps undertaken for a PCA are as follows:

1. Selection of input variables based on the spectral bands of Sentinel-2 and Landsat 8 multispectral instrument (Table 1-2). Spectral bands which describe reflectance derived from atmospheric properties are not included as they do not represent surface characteristics. These are bands 1, 9 and 10 for Sentinel-2 and bands 1, 8 and 9 for Landsat 8.
2. Assessment of data suitability for PCA using the Kaiser-Meyer-Olkin (KMO) measure of sampling adequacy and Bartlett's test of sphericity (Jolliffe and Cadima, 2015). Given that the acceptable KMO range is from 0.0 to 1.0, values of 0.841 and 0.632 for Sentinel-2 and

Landsat 8 respectively suggest the adequacy of the dataset size for a PCA (Table 3; Babel et al., 2014). The Bartlett's sphericity test value (Table 3) is significant at the 5% level confirming that the original spectral bands are uncorrelated and suitable for dataset structure detection (Pallant, 2005).

3. Determination of the dominant PCs for describing spectral dataset variability using the Kaiser criterion to retain components with eigenvalues > 1.0. This ensures that the extracted components explain more of the variance in the dataset than any one of the original variables by itself.

Statistical Test		Sentinel-2	Landsat 8
KMO Measure of Sampling Adequacy		0.841	0.632
Chi-Square		639107.63	12870571.00
Bartlett's Test of Sphericity	df	55	21
	Sig.	0.000	0.000

Table 3. Kaiser-Meyer-Olkin and Bartlett tests to demonstrate suitability of Sentinel-2 and Landsat 8 datasets for Principal Components Analysis. KMO tests the ratio of item correlations to partial item correlations. The partial item correlations should be similar to raw correlations given the assumption that common factors are the source of variance for different surface types. Bartlett Sphericity Test determines suitable dataset structure.

The merits of the PCA include increased interpretability of large datasets, reduction of data loss, and *a priori* definition of uncorrelated variables (Jolliffe and Cadima, 2015). Specifically, the automated classification method removes the error associated with pareidolia (tendency for the human eye to incorrectly perceive a stimulus as a feature). Furthermore, it has potential for broad application due to the ability to calculate slush extent without the requirement of complex radiometric, topographic or speckle corrections.

The PCA identifies which spectral bands contribute the most to variability in reflectances, and extracts clusters which can be interpreted to confirm the presence of distinct supraglacial features. The interpretation of the PCs which describe distinct parts of the ice shelf spectral variability is aided by training pixels. Training pixels are taken from manually delineated SGL, slush, and snow features on NIS from Landsat 8 image 165-110 acquired on 14/01/2020 and Sentinel-2 image 929-941 acquired on 31/01/2019 (Figures S5-9).

Training pixels aid *qualitative* interpretation of the extracted PCs and the automated method (Figure 6) uses information from the PCA for *quantitative* delineation of supraglacial features. Within each PC, the statistically significant spectral bands are identified and the frequency distribution of pixel-by-pixel reflectance for each band is plotted. Histograms of the constituent PC bands are then analysed in Python to extract turning points in the frequency distribution.

Histograms of spectral reflectance for each significant PC band are generated for the study-site region from the most recent images extracted from Sentinel-2 (929-941, 31/01/2019) and Landsat 8 (165-110, 14/01/2020). The frequency distribution of reflectance values for each band is expected to represent variation from different surface features within the overall spectral signature (Figure 7). For a trimodal histogram distribution, with lower lake spectral reflectance values and higher slush and ice spectral reflectance values, the minima are extracted as threshold values (Appendix – Code 4).

The Python script for analysing spectral band frequency distributions and extracting thresholds goes through a series of processing steps (Figure 7). The histograms group pixels into bins of equal-sized reflectance ranges. Iterations through adjacent bins identify the greatest difference between bins (above a threshold prominence) as a minima or maxima (Figure 7a). The prominence value removes noise in the distribution so that only major turning points are identified. The distinct slush and snow peaks are easily identified using this method whilst the plateau of low spectral reflectance values, representing SGL pixels, remain uncategorised.

The threshold spectral band reflectance, which represents the transition from lake to slush, is where the low-reflectance plateau terminates. The plateau value is set as the average pixel number for 100 bins on the plateau. The plateau termination is where the difference between the number of pixels in one bin and the plateau average exceeds 10% of the plateau average (Figure 7b). This must be consistently true for 20 adjacent bins to confirm plateau termination. The code outputs minima across the whole frequency distribution which are threshold reflectance values identifying different supraglacial meltwater features (Figure 7c).

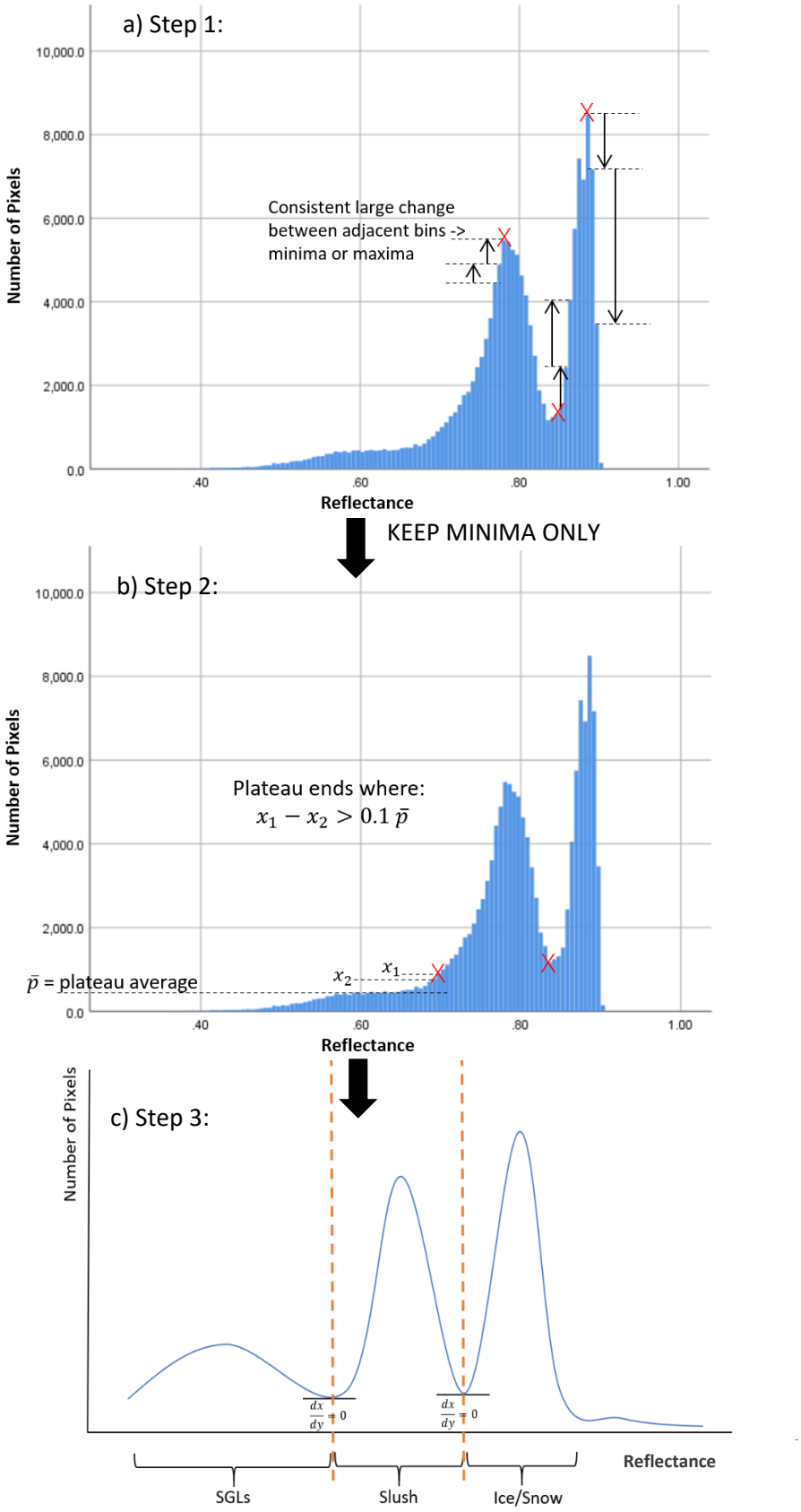

Figure 7. Python script processing steps applied to each spectral band identified by PCA as significant. Input is typical trimodal frequency distribution of spectral reflectance for each band. Step 1: code identifies maxima and minima, only keeps minima. Step 2: plateau termination into first prominent peak identified. Step 3: threshold spectral reflectance values extracted.

The accuracy of the extracted thresholds is tested across all images (Tables S1-S2) to ensure that the thresholds are useful for delineating extents irrespective of timing of image capture. The sensitivity of calculated lake and slush areas to band thresholds is evaluated across all austral summer images by varying each band threshold by ± 10% (Section 4.2i).

A multi-class confusion matrix is also generated as a measurement of PCA-histogram performance in delineating SGL, slush, and ice pixels using different satellite data. Supraglacial feature masks for Landsat 8 (ID: 165-110 08/01/2018 and 167-110 24/12/2018) and Sentinel-2 (ID: 080-919 11/01/2018 and 080-929 22/12/2018) images, captured within 2-3 days of each other, are compared pixel-by-pixel over a 15 km^2 region on NIS. Pixels which are identified in both satellite images as belonging to the same supraglacial class increase the measured precision of the PCA-histogram method. These results (Section 4.2) indicate the validity of using the derived Landsat 8 and Sentinel-2 feature masks as an input domain for the SEB model, described in the following section.

3.2 Surface Energy Balance Model

3.2i Source Data

To simulate energy balance at lake and slush surfaces on the NIS, the model is forced using Global Forecast System (GFS) meteorological data. The Global Forecast System is a model which outputs gridded meteorological variables at 0.25 arc degrees resolution every 6 hours (NOAA, 2015). The GFS provides measurements of temperature (°C), specific humidity (g/kg), wind speed (m/s), and downward shortwave radiation flux (W/m^2) since 01/07/2015.

Although GFS data is forecasted without reanalysis, it is favoured over ERA-5 data which is yet to have uploaded radiation data into Earth Engine. The Novolazarevskaya automatic weather station (70°46’04” S, 11°49’54” E) has recorded *in situ* weather data on NIS since 1961 providing a useful validation dataset for forecast data. However, the weather station data is recorded too infrequently for initial model development.

3.2ii Model Development

Google Earth Engine (GEE) is used to develop and implement the SEB model. GEE is a cloud-based geospatial processing platform which contains archived remotely sensed images and has computational power to optimise synchronous dataset processing (Gorelick et al., 2017). Furthermore, functions in GEE use per-pixel algebraic functions which make it applicable irrespective of region or scale. The framework of the model, sensitivity testing to input meteorological data, and validation are now outlined in turn.

3.2iii Physical Description of the System

Supraglacial lakes are complex systems with multiple boundary exchanges of energy and mass. Energy fluxes that have been previously modelled include atmosphere to lake surface, through-water convection, subaqueous to ice, and energy advected through the system via mass transfers (Figure 8). The point-based energy balance model applied across lake, slush and clean ice regions follows the equations set out by Law et al. (2020) considering only surface energy exchanges.

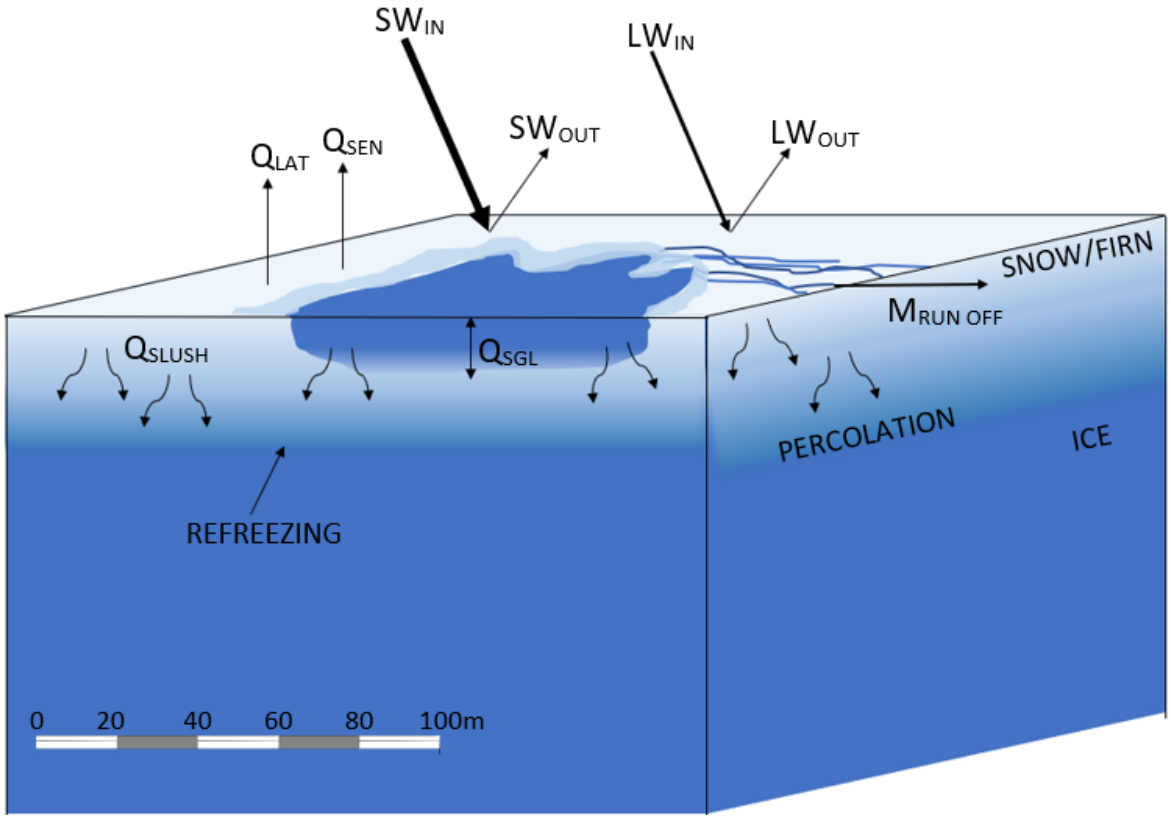

Figure 8. Schematic for supraglacial and englacial energy transfers, mass transfers and physical processes. This study focuses on surface energy exchanges. Processes are incorporated into energy balance following Buzzard et al. (2018). SW – shortwave radiation, LW – longwave radiation, Q_{LAT} – latent heat flux, Q_{SEN} – sensible heat flux.

The energy balance of an infinitesimally thin surface layer is defined as:

$$Q = (1 - \alpha)F_{SW} + \varepsilon F_{LW} - \varepsilon\sigma T^4 + F_{sen} + F_{lat} \quad (1)$$

where Q is total energy per unit area (W/m^2) stored in the surface, F_{SW} is incoming shortwave radiation flux (W/m^2), F_{LW} is incoming longwave radiation flux (W/m^2), F_{sen} is sensible heat flux (W/m^2) and F_{lat} is latent heat flux (W/m^2), α is albedo, ε is emissivity, σ is the Stefan-Boltzmann constant (5.67 × 10^{-8} W/m^{2}K^4) and T is surface temperature (K). Each of the surface energy fluxes are discussed and the equations representing each in the model are outlined.

Shortwave Radiation

Incoming shortwave radiation flux (F_{SW}) is a 6-hourly forecast from GFS data. The value of F_{SW}, obtained closest to Landsat 8 or Sentinel-2 image capture time, is extracted from the GFS dataset to calculate SEB. Incoming shortwave radiation corresponding to each spectral band is calculated using weighting coefficients as specified in Tables 4-5 (Vanino et al., 2018). The weighting coefficient represents the fraction of incident solar radiation that falls within a specified range of wavelengths defined by satellite spectral bands. Shortwave radiation flux is assumed here to be independent of elevation (within a 400 m range) given that it is unlikely to vary significantly across an ice shelf (Luthje et al., 2006; Jakobs et al., 2019).

Broadband surface albedo is calculated as the integration of surface reflectance across the shortwave spectrum (D'Urso and Calera, 2006), as shown in Equation (Eq. 2).

$$\alpha = \Sigma\,|\rho \cdot w| \tag{2}$$

where α is albedo, ρ is surface reflectance for a given band, w is the weighting coefficient (Tables 4-5).

Multiplying reflectance by weighting coefficients gives albedo per pixel for each Sentinel-2 and Landsat 8 image which is used to calculate net shortwave radiation flux (Tables 4-5). The weighting coefficient is calculated, following Vanino et al. (2018), as:

$$w = \frac{\int_{LO}^{UP} R_\lambda \cdot d\lambda}{\int_{0.4}^{2.4} R_\lambda \cdot d\lambda} \tag{3}$$

where R_λ is extra-terrestrial irradiance for wavelength λ (µm); and *UP* and *LO* are upper and lower wavelength bounds for bands, respectively. The values 0.4 µm and 2.4 µm represent the absolute solar spectral irradiance (Thuillier et al., 2003).

Weighting coefficients for Sentinel-2 bands 1, 9 and 10, and Landsat 8 bands 1, 8, and 9 are not used in the calculation of albedo given that these bands do not describe surface reflectances.

Band	Band Name	Centre λ	Spectral Width Δλ	In-band solar spectral irradiance	*w*
		(μm)	(μm)	(W/m^2)	
2	Blue	0.49	0.065	3594	0.1324
3	Green	0.56	0.035	2958	0.1269
4	Red	0.67	0.030	2508	0.1051
5	Red Edge1	0.71	0.015	2319	0.0971
6	Red Edge2	0.74	0.015	1929	0.0890
7	Red Edge3	0.78	0.020	1664	0.0818
8	NIR	0.84	0.115	1392	0.0722
11	SWIR1	1.61	0.090	63	0.0167
12	SWIR2	2.19	0.180	50	0.0002

Table 4. Weighting coefficients of Sentinel-2 spectral bands for the calculation of albedo using Equation 2. Weighting coefficient represents the fraction of solar radiation of a particular wavelength as a proportion of total irradiance (Source: Vanino et al., 2018).

Band	Band Name	Spectral range λ (μm)	Spectral Width Δλ (μm)	*w*
2	Blue	0.45 - 0.51	0.06	0.3
3	Green	0.53 - 0.59	0.06	0.277
4	Red	0.64 - 0.67	0.03	0.233
5	NIR	0.85 - 0.88	0.03	0.143
6	SWIR1	1.57 - 1.65	0.08	0.036
7	SWIR2	2.11 - 2.29	0.18	0.012

Table 5. Weighting coefficients of Landsat 8 spectral bands for the calculation of albedo using Equation 2. Weighting coefficient represents the fraction of solar radiation of a particular wavelength as a proportion of total irradiance (Source: Silva et al., 2016).

Longwave Radiation

The net longwave radiation (F_{LW}) is calculated as the difference between atmospheric incoming longwave radiation (L_{IN}) and outgoing longwave radiation dependent on the temperature of the surface (Steiner et al., 2015; Miles et al., 2016):

$$F_{LW} = L_{IN} - \varepsilon_{surf}\sigma {T_{surf}}^4 \quad (4)$$

where ε_{surf} is emissivity of lake and slush, σ is the Stefan-Boltzmann constant (5.67 x 10^{-8} W/m^2/K^4), and T_{surf} (K) is pixel surface temperature. The emissivity coefficients (ε_{surf}) for lake and slush pixels are 0.97 and 0.94 respectively following calibrated values determined by Law et al. (2020).

Given the lack of incoming longwave radiation forecasts in the GFS dataset, air temperature at 2m is used as a proxy for the incoming longwave radiation (Malakar et al., 2018) according to the Stefan-Boltzmann law (Eq. 5).

$$L_{IN} = \varepsilon_{air}\sigma {T_{air}}^4 \quad (5)$$

where ε_{air} is emissivity of air, T_{air} is the air temperature (K) at 2 m above ice shelf surface.

The incoming longwave radiation is calculated based on clear sky emissivity. Busetto et al. (2013) determine clear sky emissivity using *in situ* pyrgeometers on Dome C, Antarctica, which corroborate calibrated emissivity values.

The right-hand term of equation 4 gives the outgoing longwave radiation. The sum of reflectance in the SWIR bands is converted into radiant flux emitted from a surface per unit area. Surface temperature of each pixel is calculated using Planck's radiance function (Eq. 6) which converts surface reflectance into a temperature (Ghulam, 2010).

$$t(\lambda, L) = \frac{c_2}{\lambda \ln\left(\frac{c_1}{\lambda^5 L} + 1\right)} \quad (6)$$

where *t* is temperature (K), *L* is radiance (W/m^2/sr), c_1 is 1.191 x 10^8 (W/m^2/sr), c_2 is 1.438 x 10^4 (K μm) and λ is wavelength (μm) (Law et al., 2020).

With surface and air temperature data, net longwave radiation for each lake and slush pixel is calculated (Eq. 4) for each available Landsat 8 and Sentinel-2 image in the austral summers of 2017-2020.

Sensible and Latent Heat Fluxes

Sensible heat describes energy transferred or emitted from the ice shelf surface by change in temperature without a change of physical state. Firn or ice surfaces with higher sensible heat fluxes are more sensitive to changes in state and therefore release greater amounts of latent heat. Latent heat does not affect surface temperature, but the energy exchange causes a change of physical state.

Sensible (F_{sen}) and latent heat (F_{lat}) fluxes are calculated as:

$$F_{sen} = \rho_a C_p C_T v(T_a - T_s) \quad (7)$$

where ρ_a (kg/m^3) is the density of dry air, C_p (J/K) is the specific heat capacity of dry air, C_T is a function of atmospheric stability, *v* (m/s^2) is wind speed and T_a and T_s (K) are air and surface temperature respectively (Buzzard et al., 2018).

$$F_{lat} = \rho_a L_f C_T v(q_a - q_s) \quad (8)$$

where L_f (J/kg) is latent heat of fusion of water, q_a and q_s are air and surface humidities (g/kg) (Buzzard et al., 2018).

Sensible and latent fluxes are calculated using the bulk aerodynamic method with an atmospheric stability correction (Eq. 9), as implemented by Reid and Brock (2014) and Miles et al. (2016).

$$\left\{ \begin{array}{ll} C_T = C_{Ts}\left(1 - \dfrac{2bRi}{1 + c|Ri|^{0.5}}\right) & if\ Ri < 0 \\ C_T = C_{Ts}\,(1 + bRi)^{-2} & if\ Ri \geq 0 \end{array} \right\} \quad (9)$$

where the constants are C_{TS} = 1.3 x 10^{-3}, b = 20, and c = 50.986 and Ri is the bulk Richardson number.

The Richardson number (Eq. 10) is the ratio of buoyancy of air, related to temperature and surface roughness, to the flow shear term, providing a measure of dynamic stability (Encyclopaedia Britannica, 2016). Flow shear describes the shear stress between layers of a fluid moving at different speeds.

$$Ri = \frac{g(T_a - T_s)\,z}{T_a v_a^2} \quad (10)$$

where z is height of instruments, equal to 10 m following Law et al. (2020), and other variables defined as above.

Where the air temperature exceeds the surface temperature (Ri > 0), the flow is stable unless disrupted by strong eddies. Where surface temperature exceeds the air temperature (Ri < 0), the air flow becomes dynamically unstable and turbulent. The Richardson number is calculated to be consistently positive over slush areas given that slush has a lower temperature than surrounding atmosphere. Atmospheric stability found over lakes at the grounding line degenerated into instability and turbulence over lakes found further towards the ice-shelf front (Section 5.2). The SEB model accounts for spatial variation by calculating atmospheric stability per image pixel.

The difference between specific humidity of a given supraglacial surface type (q_s) and the air (q_a) is applied in equation 8 to calculate latent heat. Specific humidity of the air (q_a) is extracted from the GFS data at 2 m above ground for 6-hourly intervals on the day of image acquisition. Specific humidity at the surface of lake and slush pixels is calculated by obtaining saturation vapour pressure (Pa), at temperature T (K), and consequently calculating the mixing ratio of water vapour (ω), in the method set out by Law et al. (2020).

The temperature (K) of the surface is calculated following equation 6, using the Planck's irradiance function to convert SWIR band reflectance to temperature. For each pixel with temperature, T (K), saturation vapour pressure, e_s (Pa), is calculated as:

$$e_s(T) = 0.611 \times 10^{\left(\frac{7.5T}{T+273.3}\right)} \quad (11)$$

Saturation vapour pressure, *e* (Pa), at any given pixel is applied to obtain the air mixing ratio, ω :

$$\omega = \frac{eR_d}{R_v(p-e)} \tag{12}$$

where *p* (Pa) is pressure, R_d is the specific gas constant for dry air (J/kg K), and R_v is the specific gas constant for water vapour (J/kg K).

The specific humidity of the surface, q_s, for calculating latent heat can then be calculated from the mixing ratio (Eq. 13).

$$q_s = \frac{\omega}{\omega + 1} \tag{13}$$

Specific humidity of the air and surface, as calculated above, are incorporated into equation 8 to give latent heat. The above steps give values of latent and sensible heat for each pixel for inclusion in the overall surface energy balance calculation.

Using the lake and slush areas delineated by the PCA-histogram thresholding, net energy balance is calculated as the sum of the energy fluxes across the entire lake or slush region for images captured in austral summers of 2017 - 2020. Average SEB for lake and slush areas is calculated as the mean of the energy fluxes per SGL or slush pixel over a given time period.

3.3 Surface Energy Balance Model Verification & Validation

3.3i Model Verification

To confirm that the SEB flux calculation is sensitive to meteorological variation, GFS shortwave radiation, air temperature, wind speed and humidity datasets, are plotted against modelled shortwave and longwave fluxes for images captured at the peak of melt extent (Section 4.3). Sensible and latent heat fluxes are expected to vary by lower magnitudes than shortwave and longwave fluxes given that they are constrained by changing surface conditions. Four measurements of GFS data (6-hourly) from one day either side of Sentinel-2 and Landsat 8 images from mid-melt seasons of 2017-2020 are used to run the SEB model. Time series of output modelled shortwave and longwave radiation and GFS meteorological variability are plotted to highlight any lags between model inputs and outputs. By using the same input reflectance data from satellite images, we assume that the distribution of lake and slush pixels remains unchanged over each 3-day period and that the SEB model is sensitive to variable meteorological conditions.

3.3ii Model Validation

Under the assumption that all radiative energy transferred to melt the ice shelf surface is stored in the internal energy of surface water, total SGL and slush water volume is a proxy for energy transferred. This is a reasonable assumption given that energy transfers from other sources are unlikely to cause surface melt on Antarctic ice shelves (Buzzard et al., 2018). Buzzard et al. (2018) confirm with model sensitivity tests that ocean temperature changes at the bottom of the ice shelf model domain do not affect the ice shelf surface over inter-annual time scales. Heat transfer by precipitation is negligible (Akhoudas et al., 2020) and precipitation that falls as snow remains *in situ* rather than advecting energy into proximate basins. Although such assumptions introduce some uncertainty, calculation of total water volume as a proxy for energy transferred from the atmosphere to ice shelf is a first step for model validation.

Slush Volume

Slush volume is more difficult to calculate than SGL volume given its spatially and temporally variable porosity. Slush is a complex medium with three constituent physical states of water that interact with each other. Liquid water does not penetrate through snow uniformly (Coleou et al., 1998; Schneebeli, 1995) which makes irreducible water content volume at depth difficult to determine.

Although slush properties have been recorded in laboratory studies (e.g. Coléou and Lesaffre, 1998; Marshall and Forster, 2005), sparse *in situ* data of slush liquid water content and, crucially slush depth across East Antarctic ice shelves, prevents validation of laboratory estimates. Future development of and data provision from sophisticated satellite sensors may facilitate direct measurement of slush depth. For example, the Advanced Topographic Laser Altimeter System, on-board ICESat2, has detected previously unimaged sub-surface lake and slush zones with unprecedented resolution by recording individual photon return times (Markus et al., 2017). However, data availability over NIS from such sensors is insufficient to calculate slush depth or porosity. Therefore, the SEB model is validated by comparison of modelled energy transfer at lake pixels to inferred energy transfer from lake volume.

Lake Volume

Considering the control volume of a lake as a reservoir of mass and energy, the internal energy of the pond, S (J), available for melt is calculated:

$$S = c\rho V(T - 273.15) \tag{14}$$

where c (J/kg K) is the specific heat of water, ρ (kg/m^3) is the density of water, T (K) is pond temperature and V (m^3) is pond volume.

Density of lake water on ice sheets is assumed to be 997 kg/m^3 given that it is freshwater with negligible impurities. Lake pixel temperature is calculated using Planck's irradiance function (Eq. 6) to convert irradiance in SWIR bands to temperature.

Lake depth retrieval is based upon the understanding that deep water absorbs more energy than shallow water and will reflect lower proportions of incident radiation (Arnold et al., 2014; Pope et al., 2016; Sneed and Hamilton, 2007; Williamson et al., 2017, 2018b). Pope et al. (2016) determine that optimal supraglacial depth retrieval can be derived from the Bouguer-Lambert-Beer law (Eq. 15) applied independently to red and panchromatic bands which are subsequently averaged. Here, variation in optical properties through water column with depth are approximated by red band spectral reflectance, *L(z, λ)*.

$$L(z,\lambda) = L(0,\lambda)e^{-(gz)} \tag{15}$$

where *L(0, λ)* is spectral reflectance at zero depth, *g* is the spectral attenuation coefficient (m^{-1}) and *z* is depth (m).

Written in terms of reflectance of red wavelengths, total reflectance is used to calculate depth, z, of each lake pixel (Eq. 13).

$$z = \frac{\ln(\alpha - R_\infty) - \ln(R_w - R_\infty)}{-g} \tag{16}$$

where *α* is lake bottom albedo, R_∞ is the reflectance for optically deep water (assumed to be zero following Banwell et al. 2019), R_w is the reflectance from the pixel of interest and *g* (m^{-1}) is the spectral attenuation coefficient.

The attenuation coefficient is related to losses in intensity as light propagates through a water column. Red band wavelengths are used given that longer wavelengths attenuate more rapidly in water, making lake depth estimations less sensitive to error with depth (Tedesco and Steiner, 2011). The recommended g value of 0.7507 m^{-1}, for field spectra which correspond to the Landsat 8 and Sentinel-2 red bands (B4), is applied (Pope et al., 2016; Williamson et al., 2017). Georgiou et al. (2009) suggest that the range of specific spectral attenuation which may occur across different wavelengths leads to a variance of 9.5% in estimated lake depth. This justifies the use of a single spectral band for lake volume estimation.

Lake bottom albedo (*α)* is calculated from the reflectance immediately proximate to identified lake pixels. A mask of non-lake areas is generated based on PCA band thresholds. Red band reflectance from lake-edge pixels is interpolated using a Gaussian function across masked lake areas to give predicted lake base albedo (Appendix – code 5; Banwell et al., 2014). The assumption of Gaussian

variability in base albedo is an improvement on previous studies that use non-variable regional albedo estimates (Sneed and Hamilton, 2007; Morriss et al., 2013). However, the uncertainty resulting from the Gaussian estimation of lake-base albedo has not yet been quantified. The overall assumptions with this physically-based empirical depth calculation, as set out originally by Sneed and Hamilton (2007), are: (i) that the surface is undisturbed by wind, (ii) the SGL is homogenous and (iii) that there is no sediment in the water column.

The internal energy of SGLs across the study site, that is the sum of calculated energy (S) at each SGL pixel, is a proxy for energy transferred to the ice sheet (Eq. 14). Internal energy of the lake-covered area is calculated at each pixel to retain high spatial resolution of temperature data rather than using an ice-sheet average. Similarly, calculated pixel lake depths are multiplied by 900 m^2 for Landsat 8 (30m x 30m) and 225 m^2 for Sentinel-2 (15m x 15m), given the spatial resolution of respective satellite red bands, to quantify SGL volume per pixel. Inferred energy from lake volume is derived from the latest image captured in each austral summer. This is to ensure that peak lake volume is recorded to give an estimate of inferred energy transfer from the whole melt season.

The inferred energy transfer from lake volume is compared to cumulative modelled energy absorbed by lake pixels over the whole austral summer. The cumulative sum of modelled energy transfer is calculated for all satellite images where meltwater is present. For days between satellite image acquisitions, modelled energy absorption is assumed to be equivalent to energy absorption on the nearest day with an available satellite image. This introduces error given that, between satellite image acquisitions, lake area and energy absorption will evolve (Arthur et al., 2020; Moussavi et al., 2020). Research documenting lake evolution has potential for reducing this validation error (Arthur et al., 2020) but the low availability of satellite imagery over NIS provided insufficient information on lake evolution to extrapolate a consistent trendline between images.

Whilst it is expected that there will be some inconsistencies between calculated lake volume and inferred energy transfer (Section 4.4), this approach is a first step towards model validation. A variety of statistical measures, including the Nash-Sutcliffe Efficiency measure, R^2 value and normalised RMSE, are reported to evaluate model performance.

4. Results

4.1 Principal Component Analysis Results

4.1i Spectral Data Extraction and Visualisation

Filtering the Sentinel-2 image collection over Nivlisen Ice Shelf (NIS) extracts 23 images, of which 5 are considered useful for spectral analysis due to presence of lake and slush features and < 20% cloud cover (Table S1). Despite 5-day satellite revisit intervals, time between image acquisition is at best 21 days highlighting issues of data availability due to cloud cover. The higher frequency of Landsat 8 revisit intervals and longer operational period gives 45 useful images from November to February of 2017 – 2020 to supplement the Sentinel-2 dataset and provide a higher temporal resolution dataset.

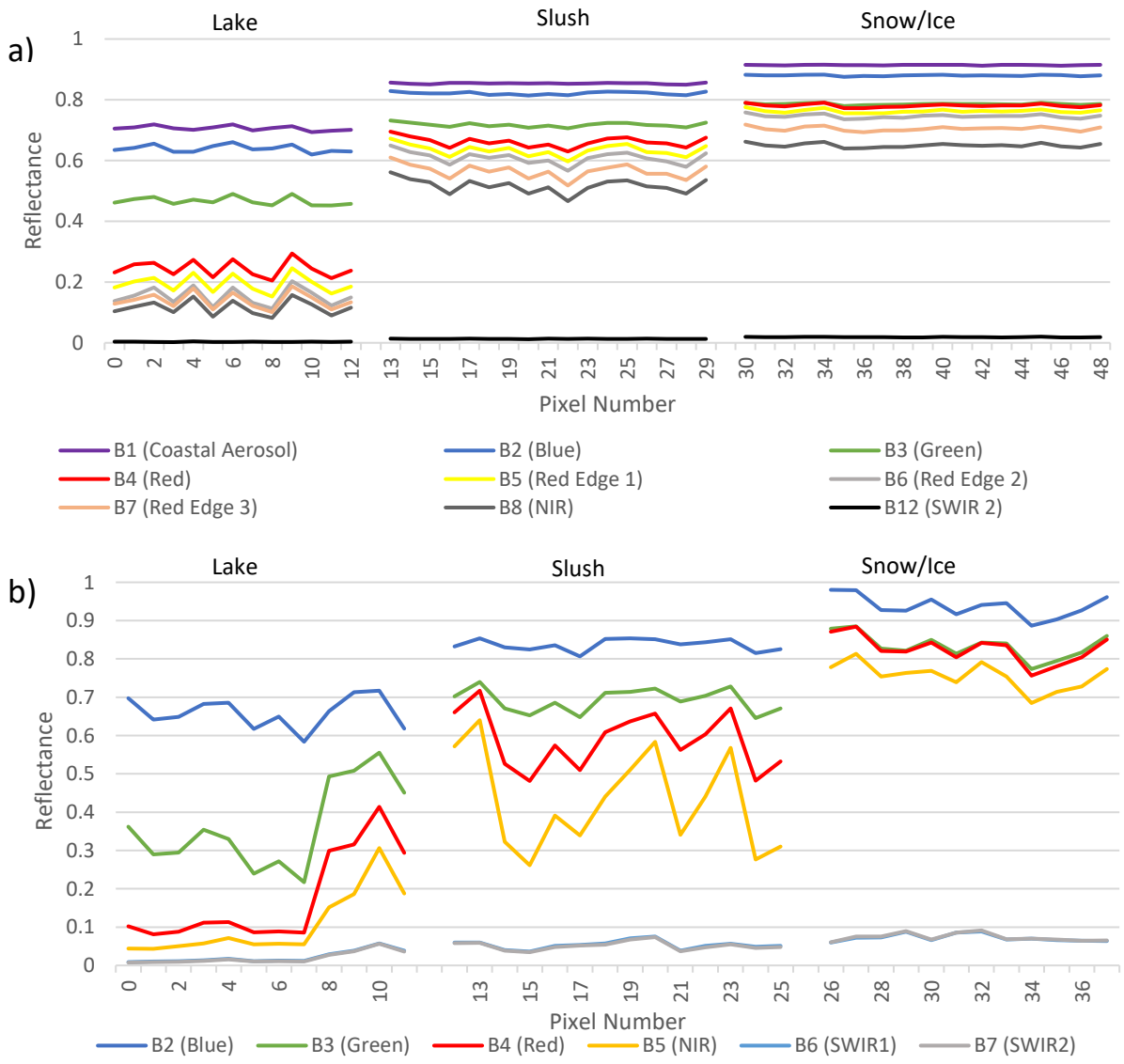

Figure 9a-b. a) Spectral signatures of different surface types derived from training pixels on NIS 31/01/2019 from Sentinel-2 (Table S3, Appendix). b) Spectral signatures of different surface types derived from training pixels on NIS 14/01/2020 from Landsat 8 (Table S4, Appendix).

The training pixels from manually delineated features in extracted Sentinel-2 and Landsat 8 images (Figure 9) enable qualitative PCA cluster interpretation whilst histograms of pixel reflectance describe total study site variability (Figures 10-11). Training pixels representing supraglacial features are manually selected by visual inspection of satellite imagery (Figures S5-9, Appendix). Each supraglacial feature can be attributed to a particular principal component confirmed by training pixel data. Detailed per pixel variation and aggregate patterns in reflectance from different surface types are described below for clean ice, slush, and SGLs in turn.

The spectral signature of clean ice is similar across visible wavelengths but drops in the infrared (Lettang et al., 2013). Extracted histogram spectral data confirms this observation as the peaks in histograms associated with ice pixels reach reflectances of 0.8 for visible wavelengths but only 0.02 in the infra-red wavelengths. Similarly, training pixels for manually-delineated ice regions have reflectance values above 0.8 for visible wavelengths but lower reflectance values for near infrared (NIR) and shortwave infrared (SWIR) (Figure 9). Overall, the majority of incoming shortwave radiation incident on snow and ice surfaces is reflected due to the high albedo of snow.

Slush has slightly lower, but generally similar, reflectance to the clean ice cluster across all wavelengths (Figure 9; Wiscombe and Warren, 1980; Rosel and Kaleschke, 2011). In regions of the ice shelf where snow is exposed to large volumes of liquid water, smaller snow particles melt whilst larger particles agglomerate and grow (Colbeck, 1982). As average grain size increases due to water saturation, reflectance decreases with largest declines in the red band (Lettang et al., 2013). Figure 9b for Landsat 8 images demonstrates blue band reflectance remains relatively high whilst a greater proportion of red wavelengths are absorbed over slush areas. NIR and SWIR reflectances are proxies for emitted thermal radiation and therefore the temperature of supraglacial surface. The higher the reflectance values across infra-red bands relative to visible band reflectance, the larger the amount of emitted infra-red energy indicating warmer temperature of the surface. Training pixels from Landsat 8 images confirm that SWIR reflectance values for slush are similar to that of snow and ice surfaces implying that slush regions are not significantly warmer than surrounding snow (Figure 9b).

Across visible wavelengths, lake pixels have low reflectance relative to slush, represented by the negative tail of histograms (Figures 10-11). For water on ice shelves with low sediment delivery, radiation absorption is lowest at ~500 nm giving lakes their bright blue appearance (Petty, 2006). This is confirmed in this study given that proportion of reflectance from the blue band to all visible bands is highest over SGL pixels for both Sentinel-2 and Landsat 8 training pixels (Figure 9). Whilst ice pixels are characterised by small variation in blue band reflectances, lake pixels cover a wide range of blue spectral reflectance values related to variable lake depth (Sneed and Hamilton, 2007; Figure

10-11). Deeper lakes reflect lower proportions of blue wavelengths and are represented by the extreme low blue reflectance values of the negative tail of histograms (Figures 10-11). Water-covered pixels have proportionally high SWIR reflectance values relative to other wavelengths, indicating that water is an efficient thermal emitter.

The spectral characteristics of clean ice, slush, and SGLs, described by manually-delineated training pixels and histogram data, aid the interpretation of PCA results. Each principal component represents clustering in the overall spectral variability which correspond to distinct supraglacial surface types.

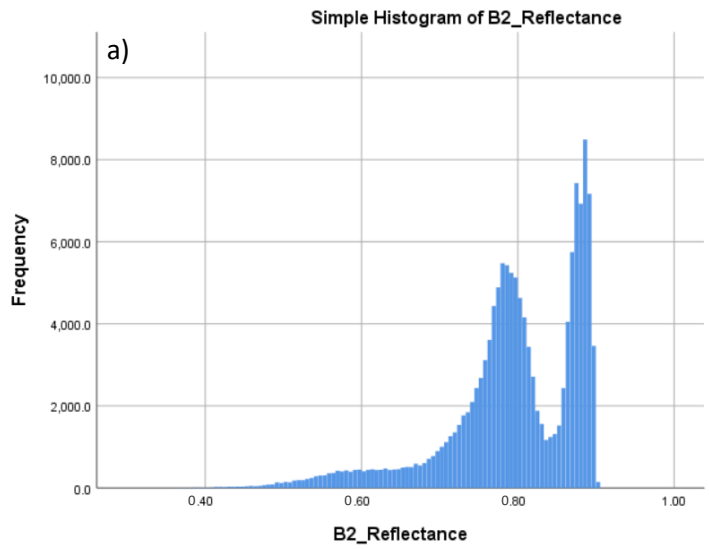
Simple Histogram of B2_Reflectance
a)
Frequency
10,000.0
8,000.0
6,000.0
4,000.0
2,000.0
0.0
0.40
0.60
0.80
1.00
B2_Reflectance

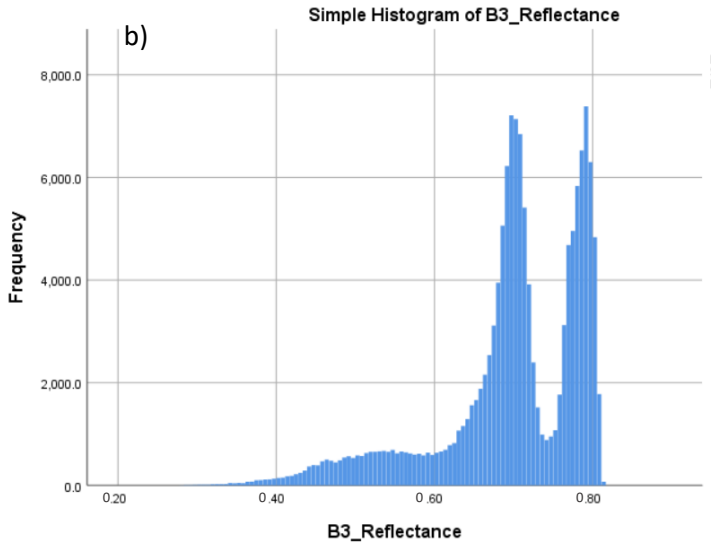
Simple Histogram of B3_Reflectance
b)
Frequency
8,000.0
6,000.0
4,000.0
2,000.0
0.0
0.20
0.40
0.60
0.80
B3_Reflectance

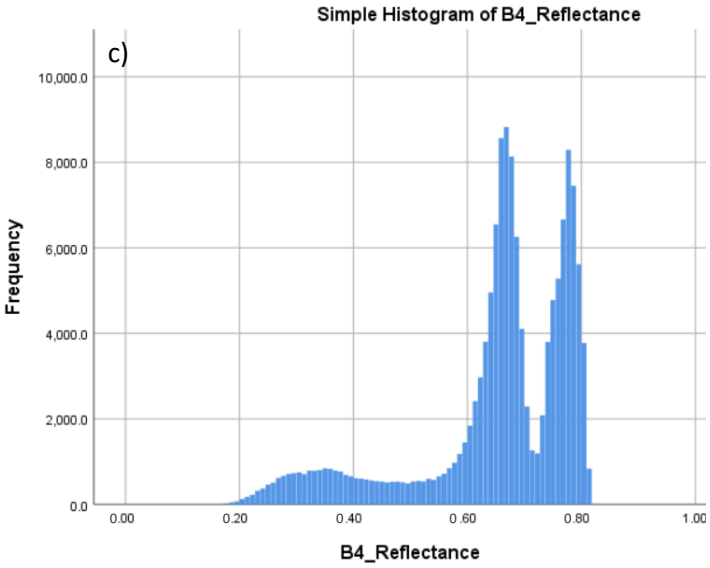
Simple Histogram of B4_Reflectance
c)
Frequency
10,000.0
8,000.0
6,000.0
4,000.0
2,000.0
0.0
0.00
0.20
0.40
0.60
0.80
1.00
B4_Reflectance

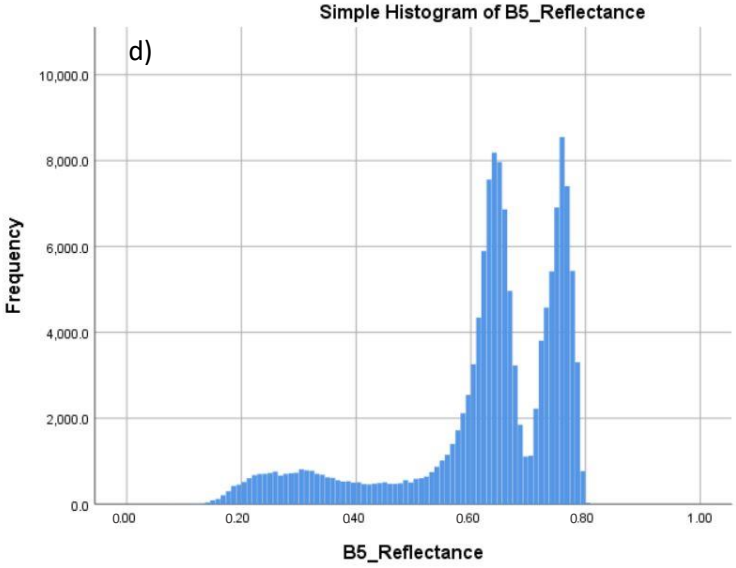
Simple Histogram of B5_Reflectance
d)
Frequency
10,000.0
8,000.0
6,000.0
4,000.0
2,000.0
0.0
0.00
0.20
040
0.60
0.80
1.00
B5_Reflectance

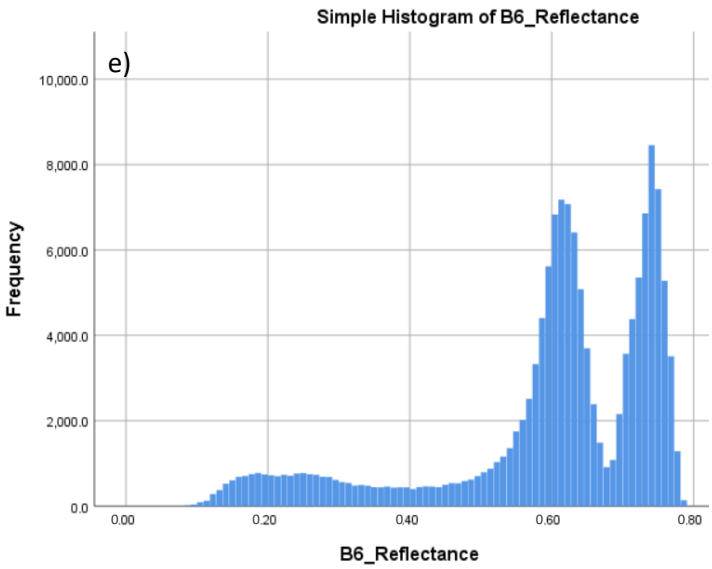
Simple Histogram of B6_Reflectance
e)
Frequency
10,000.0
8,000.0
6,000.0
4,000.0
2,000.0
0.0
0.00
0.20
0.40
0.60
0.80
B6_Reflectance

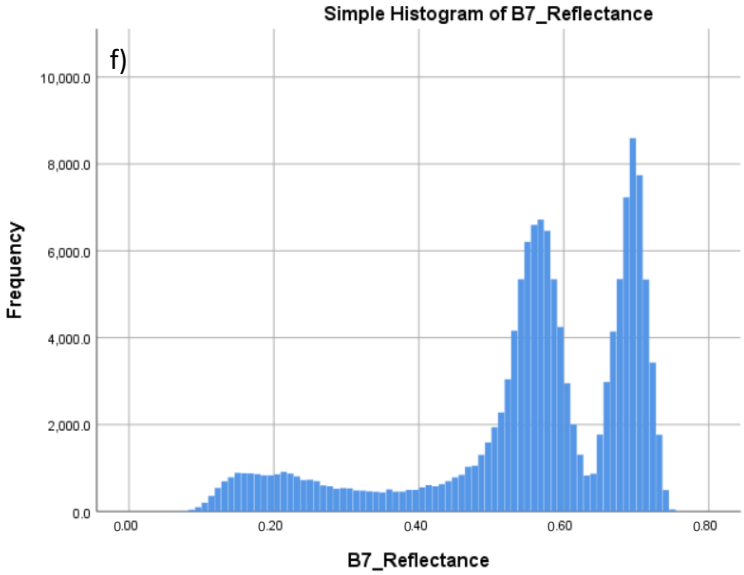
Simple Histogram of B7_Reflectance
f)
Frequency
10,000.0
8,000.0
6,000.0
4,000.0
2,000.0
0.0
0.00
0.20
0.40
0.60
0.80
B7_Reflectance

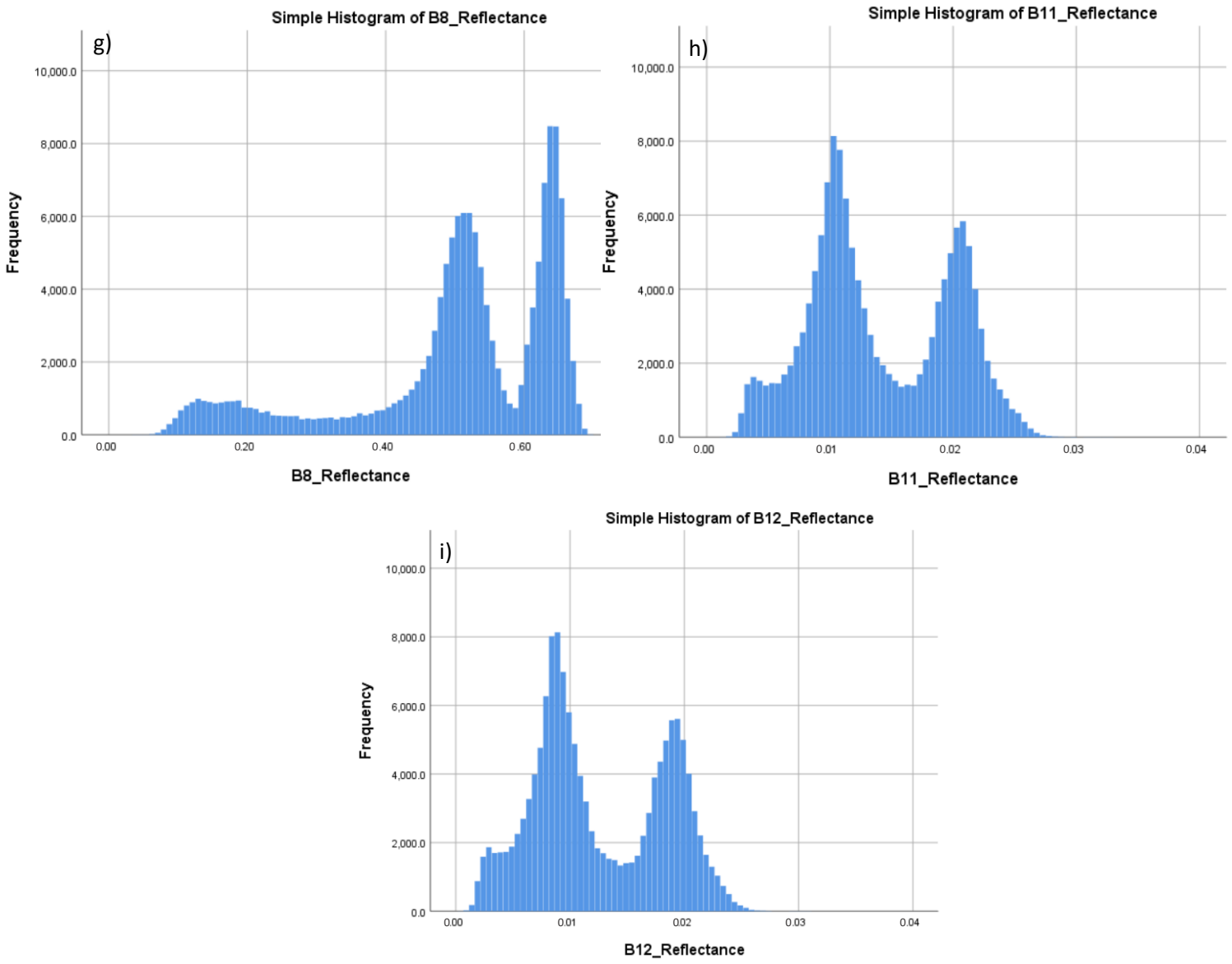

Figure 10a-i (above). Frequency distribution of pixel spectral reflectance data for each Sentinel-2 image band (31/01/2019) over the study-site region. Plotted in SPSS. Bands 1, 9 and 10 are excluded from the analysis given that they describe non-surface reflectance.

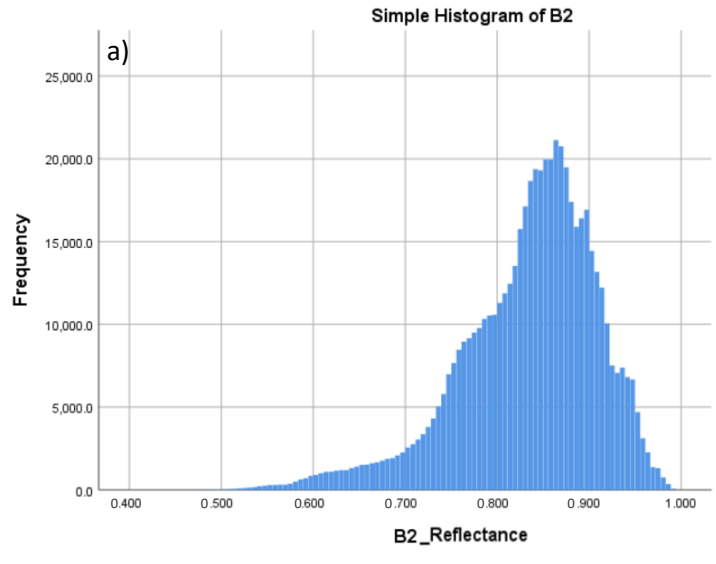
Simple Histogram of B2
a)
Frequency
25,000.0
20,000.0
15,000.0
10,000.0
5,000.0
0.0
0.400
0.500
0.600
0.700
0.800
0.900
1.000
B2_Reflectance

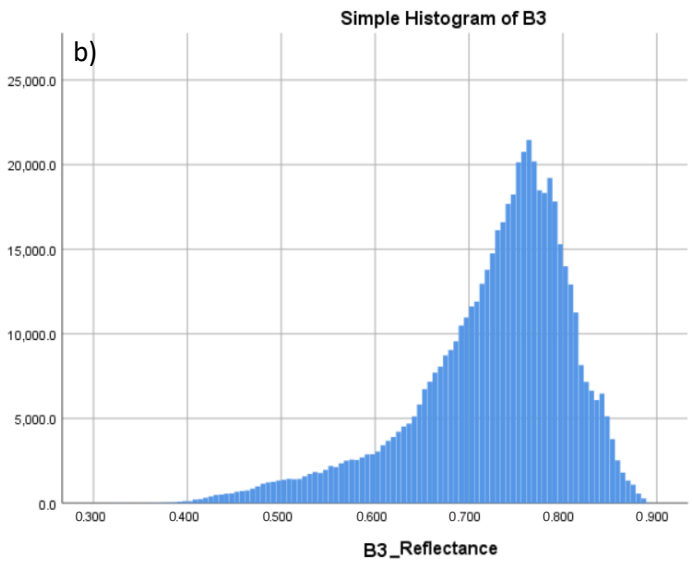
Simple Histogram of B3
b)
25,000.0
20,000.0
15,000.0
10,000.0
5,000.0
0.0
0.300
0.400
0.500
0.600
0.700
0.800
0.900
B3_Reflectance

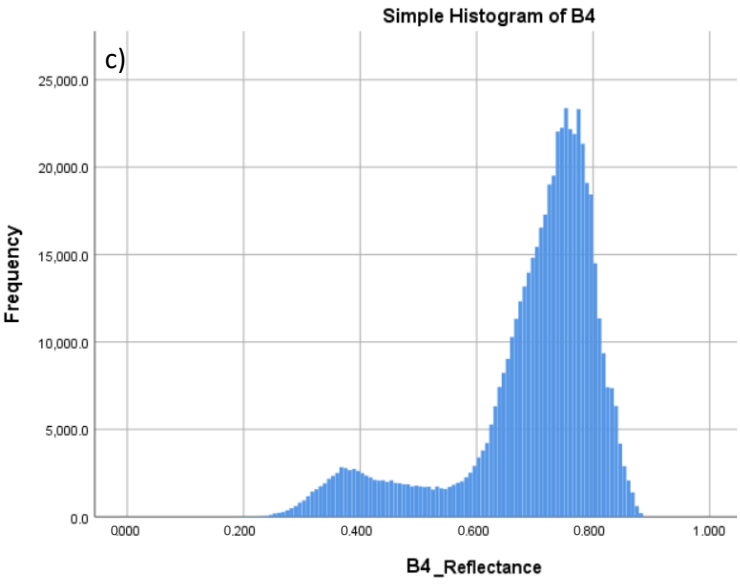
Simple Histogram of B4
c)
Frequency
25,000.0
20,000.0
15,000.0
10,000.0
5,000.0
0.0
0.000
0.200
0.400
0.600
0.800
1.000
B4_Reflectance

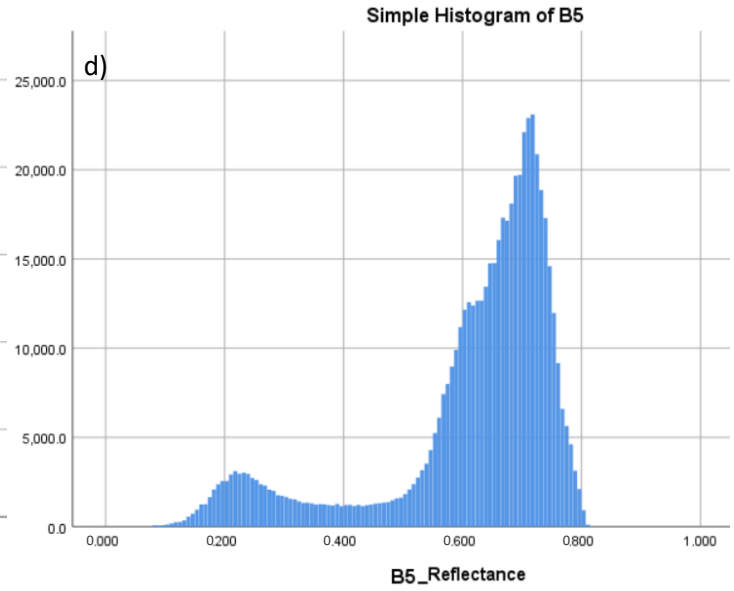
Simple Histogram of B5
d)
25,000.0
20,000.0
15,000.0
10,000.0
5,000.0
0.0
0.000
0.200
0.400
0.600
0.800
1.000
B5_Reflectance

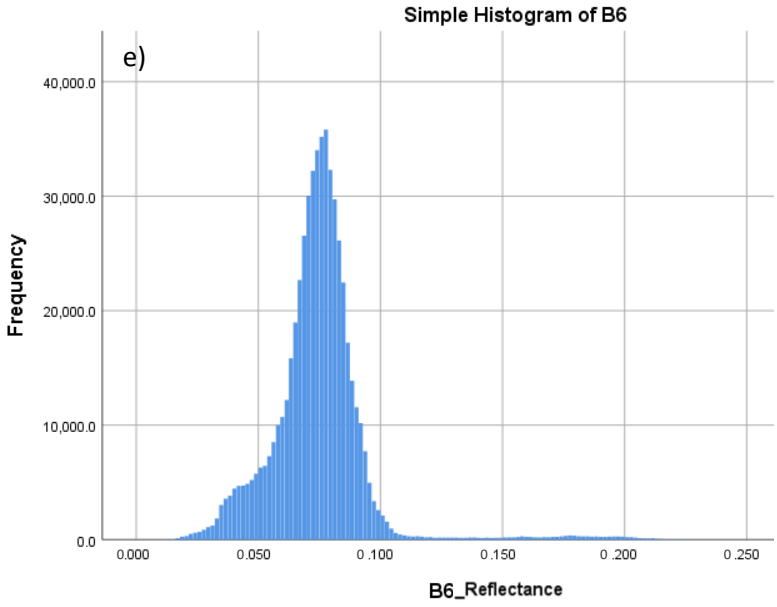
Simple Histogram of B6
e)
Frequency
40,000.0
30,000.0
20,000.0
10,000.0
0.0
0.000
0.050
0.100
0.150
0.200
0.250
B6_Reflectance

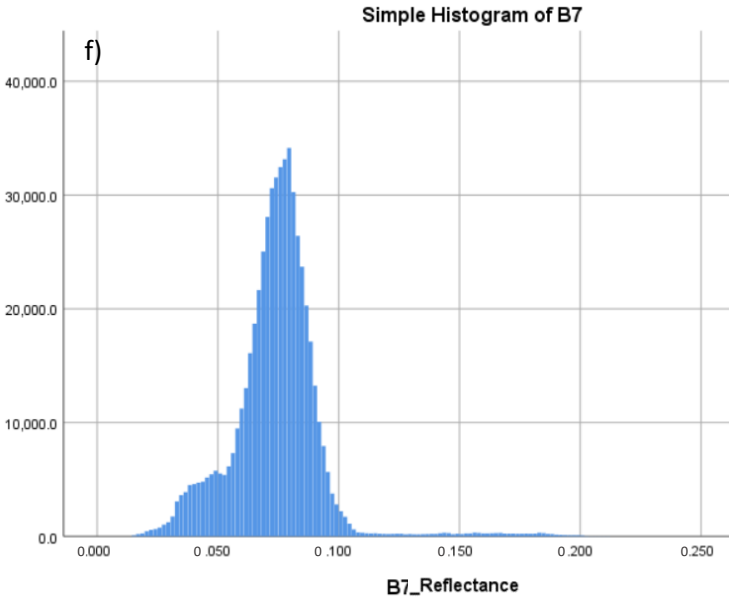
Simple Histogram of B7
f)
40,000.0
30,000.0
20,000.0
10,000.0
0.0
0.000
0.050
0.100
0.150
0.200
0.250
B7_Reflectance

Figure 11a-f (above). Frequency distribution of pixel spectral reflectance data for each Landsat 8 image band (14/01/2020) over the study-site region. Plotted in SPSS. Band 1, 8 and 9 are excluded from the analysis given that they identify non-surface characteristics or surface spectral data which is already given in other bands (e.g. panchromatic band).

4.1ii Principal Components Analysis – Results

The Sentinel-2 PCA identifies seven orthogonal components which define the total spectral variability of the NIS study-site region (Table 6). The first two Principal Components (PCs) are extracted as explanatory variables which explain 71% and 25% of total variance respectively (Table 6). The PCA derived from Landsat-8 images identifies six PCs of which the first two define 77% and 17% of total variance (Table 7). PC1 and PC2 are selected for both Sentinel-2 and Landsat 8 given that these PCs have eigenvalues greater than 1 and therefore explain greater dataset variability than any of the individual original bands.

Values in the component matrix indicate the magnitude and relationship between each of the constituent spectral bands within each PC (Tables 8-9). For Sentinel-2, VNIR bands (B2-4) are strongly positively correlated to PC1 whilst SWIR (B11-12) is weakly correlated, representing slush as bright and cool pixels (Table 8). PC2 represents pixels with low reflectance in the VNIR and high reflectance in the SWIR, indicating the dark but warmer surface of SGLs. Similarly for Landsat 8 (Table 9), PC1 has high reflectance values for all visible bands (B2-5) and slightly lower SWIR (B6-7) reflectance, representing cool and bright pixels (i.e. slush). PC2 responds to pixels with low visible reflectance and is especially sensitive to low blue band (B2) reflectance values (i.e. SGLs).

Whilst PC3 explains 2.6 % and 4.6 % of the Sentinel-2 and Landsat 8 dataset variability respectively, the eigenvalues are less than 1 and therefore PC3 is not considered to be useful for identifying significant spectral bands for feature delineation (Figure 12-13).

The bands listed in Tables 10 and 11 are those extracted by the PCA as significant in contributing to the component variability at the 1% significance level. The histograms of spectral reflectance from each constituent band are plotted and visually inspected for a trimodal distribution (Figures 10-11). Frequency distributions where there were no obvious thresholds across the dataset could not be used for distinguishing supraglacial features. For example, the near-Gaussian distribution of Landsat 8 green band (B3) spectral reflectances cannot be used to extract thresholds for delineation of slush or lake masks (Figure 11b). Sentinel-2 red edge (B8A) and SWIR2 (B12) thresholds were also excluded from the final SGL-slush delineation given that they describe similar dataset variability to the red (B8) and SWIR1 (B11) bands. Overall, the extraction of multiple spectral bands which are useful for distinguishing supraglacial features, confirms that the PCA is an appropriate and computationally efficient method for the purposes of this study.

Total Variance Explained			
Component	Initial Eigenvalues		
	Total	% Variance	Cumulative %
PC1	4.999	71.410	71.419
PC2	1.783	25.470	96.889
PC3	0.185	2.646	99.535
PC4	0.028	0.403	99.937
PC5	0.003	0.044	99.981
PC6	0.001	0.012	99.993
PC7	0.000	0.007	100.000

Table 6. Total explained variance determined by Sentinel-2 Principle Components Analysis in order of explanatory power. PCA results determined from study-site region of Sentinel-2 available image scenes.

Total Variance Explained			
Component	Initial Eigenvalues		
	Total	% Variance	Cumulative %
PC1	4.624	77.068	77.068
PC2	1.077	17.956	95.024
PC3	0.281	4.682	99.706
PC4	0.014	0.227	99.933
PC5	0.003	0.052	99.985
PC6	0.001	0.015	100.000

Table 7. Total explained variance determined by Landsat 8 Principle Components Analysis in order of explanatory power. PCA results determined from study-site region of Landsat 8 available image scenes.

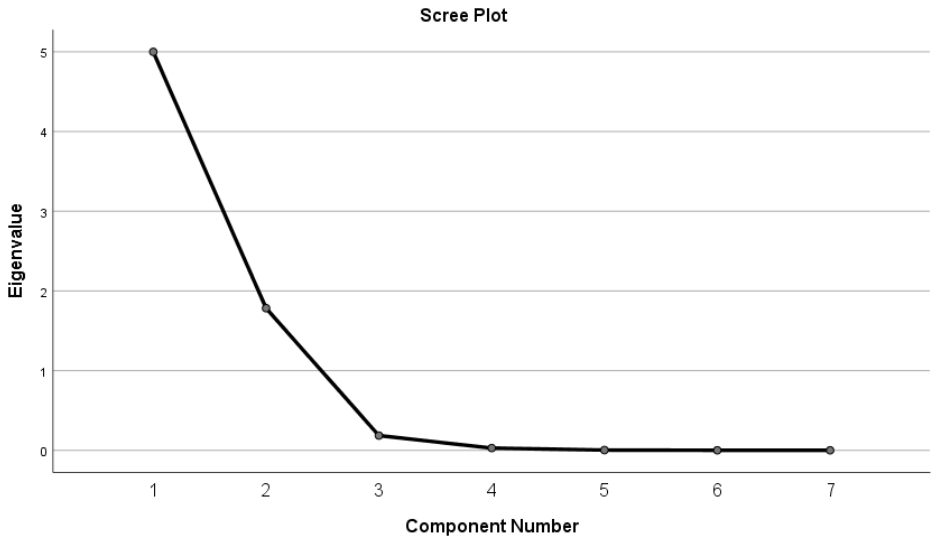

Figure 12. Scree plot of Sentinel-2 PCA eigenvalues. Eigenvalues explain the variance of the data along the new feature axes generated by the PCA. PC1 and PC2 are more successful in explaining more of the variance in the dataset than any of the individual spectral variables.

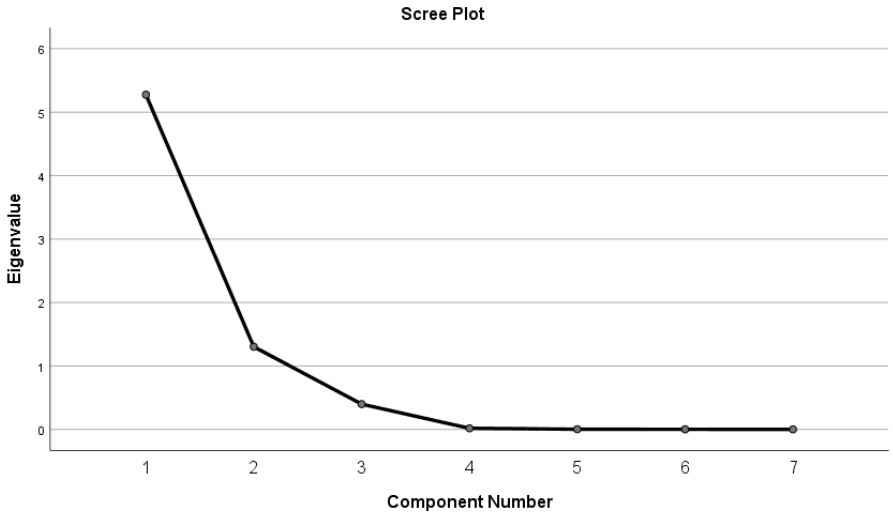

Figure 13. Scree plot of Landsat 8 PCA eigenvalues. Eigenvalues explain the variance of the data along the new feature axes generated by the PCA. PC1 and PC2 are more successful in explaining more of the variance in the dataset than any of the individual spectral variables.

Component Matrix			
		PC1	PC2
B2	Blue	0.936	-0.143
B3	Green	0.970	-0.186
B4	Red	0.967	-0.211
B7	Red Edge	0.976	-0.128
B8	NIR	0.978	-0.105
B11	SWIR1	0.381	0.923
B12	SWIR2	0.440	0.897

Table 8. Rotated component matrix from Sentinel-2 PCA determining the relative contribution of significant spectral variables to the Principle Component. PC1 represents bright and cold pixels whilst PC2 represents warm and dark pixels.

Component Matrix			
		PC1	PC2
B2	Blue	0.823	-0.442
B3	Green	0.944	-0.315
B4	Red	0.950	-0.182
B5	NIR	0.941	-0.122
B6	SWIR 1	0.760	0.635
B7	SWIR 2	0.815	0.573

Table 9. Rotated component matrix from Landsat 8 PCA determining the relative contribution of significant spectral variables to the Principle Component. PC1 represents bright and cold pixels whilst PC2 represents warm and dark pixels.

The spectral reflectance thresholds (Tables 10-11) for constituent bands of PC1 and PC2 are incorporated into GEE code to identify lake and slush pixels over the NIS (Code 1, Appendix). For the 2019 austral summer, Sentinel-2 records maximum lake and slush extents of ~89.4 km^2 and ~155

km^2 respectively, accounting for 7.4% and 12.8% of the study-site area (Table 12; Figure 14). These values are on the same order of magnitude as lake (~45.9 km^2) and slush (~65.5 km^2) area estimates from Landsat 8 images in 2019 (Table 13; Figure 15). Total meltwater coverage in 2017 by SGLs and slush accounts for 1.2 – 1.6 % of NIS's total area (7,300 km^2) which agrees with Dell et al.'s (2020) calculation of 1.6% surface meltwater coverage in 2016-2017.

Delineation of lake and slush regions using the PCA-histogram method can be compared to a band-ratio thresholding method, such as the commonly used blue-red NDWI. Direct comparisons of lake extent calculated by NDWI and PCA indicate that NDWI (threshold = 0.2) consistently underestimates SGL extent by 122 % across all images from 2017 to 2020 (Figure 16). Despite manual selection of NDWI threshold to minimise errors of commission and omission, NDWI is unable to distinguish between shallow water and slush with a lower threshold and fails to identify deep lakes where threshold is too high (Figure 17). The use of thresholding across multiple bands by the PCA is justified despite increased processing complexity.

	B2	B3	B4	B8	B11
Lake	< 0.67	< 0.59	< 0.53	< 0.34	< 0.49
Slush	0.67- 0.83	0.59 – 0.73	0.53 – 0.72	0.34 – 0.58	0.49 – 0.15
Ice	0.83 – 0.90	0.73 – 0.90	0.72 – 0.80	0.58 – 0.70	0.15 – 0.30

Table 10. Reflectance thresholds for surface feature spectral classification from Sentinel-2 images. Thresholds extracted using Python script following the method explained in Figure 7. Values to 2 s.f.

	B2	B4	B5	B6	B7
Lake	< 0.79	< 0.64	< 0.43	< 0.066	< 0.055
Slush	0.79 - 0.86	0.64 - 0.75	0.43 - 0.63	0.066 - 0.070	0.055 - 0.076
Ice	> 0.86	> 0.75	> 0.63	> 0.070	> 0.076

Table 11. Reflectance thresholds for surface feature spectral classification from Landsat 8 images. Thresholds extracted using Python script following the method explained in Figure 7. B3 is excluded because distribution only had one identifiable peak. Values to 2 s.f.

Sentinel-2	2017	2018 (Image 1)	2018 (Image 2)	2019 (Image 1)	2019 (Image 2)
Slush Area (km^2)	36.6	23.5	104.3	86.7	155.0
Lake Area (km^2)	50.3	68.9	8.4	29.3	89.4

Table 12. Lake and slush mask areas (km^2) for Sentinel-2 least cloudy images for mid-austral summer of each year from 2017-2020. Values to 1 d.p.

Landsat 8	2016	2017	2018	2019	2020
Slush Area (km^2)	0.2	17.3	50.2	65.5	51.3
Lake Area (km^2)	20.8	105.2	78.4	45.9	88.2

Table 13. Lake and slush mask areas (km^2) for Landsat 8 least cloudy images for mid-austral summer of each year from 2016-2020. Values to 1 d.p.

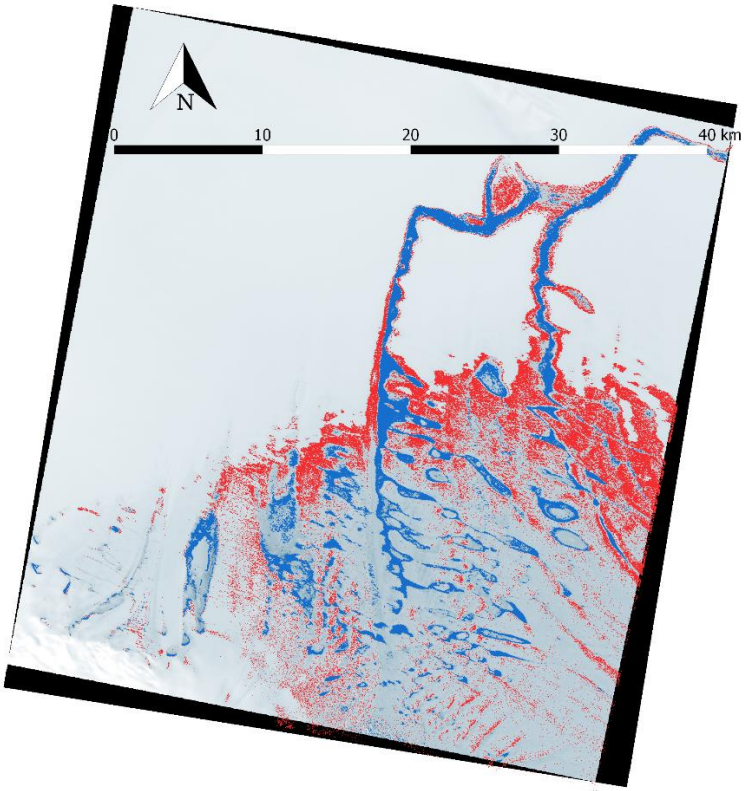

Figure 14. Lake (light blue) and slush (red) masks for NIS at the peak of the 2019 melt season. Background RGB Sentinel-2 image captured on 31/01/2019 (COPERNICUS/S2/20190131T080929_20190131T080941_T32DNG). Masks delineated using spectral thresholds derived from PCA-histogram method (Table 10).

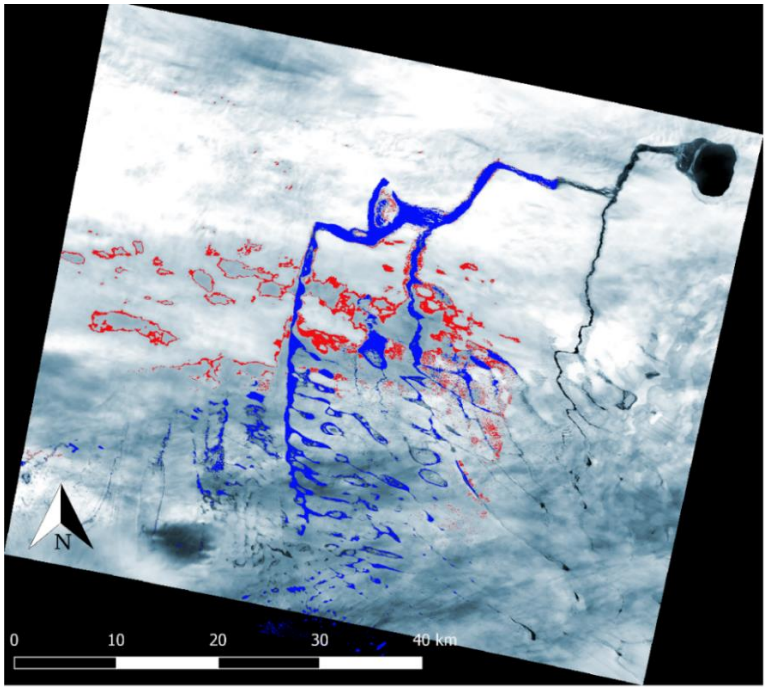

Figure 15. Lake (light blue) and slush (red) masks for NIS at the peak of the 2020 melt season. Background RGB Landsat 8 image captured on 14/01/2020 (LANDSAT/LC08/C01/T2_TOA/LC08_165110_20200114). Masks delineated using spectral thresholds derived from PCA-histogram method (Table 11). Image area extends beyond the mask to remain consistent with masks produced for all satellite and inter-annual acquisitions.

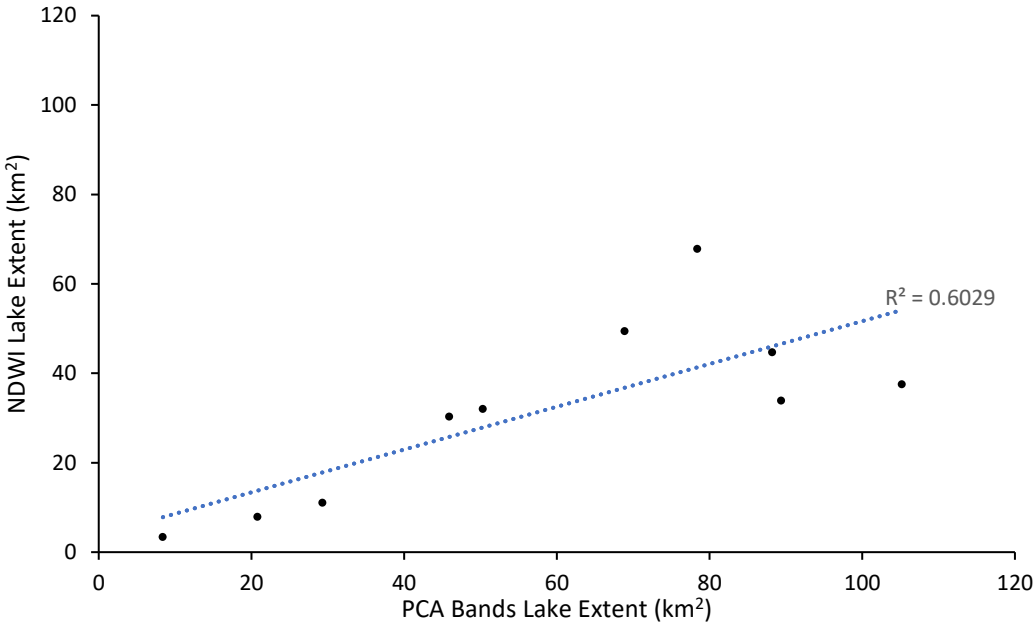

Figure 16. Scatterplot of lake area derived by NDWI (threshold 0.2) and PCA-histogram method to show strength of agreement between outputs. Linear trendline(blue dashed line) demonstrates that NDWI method consistently under-estimates lake area.

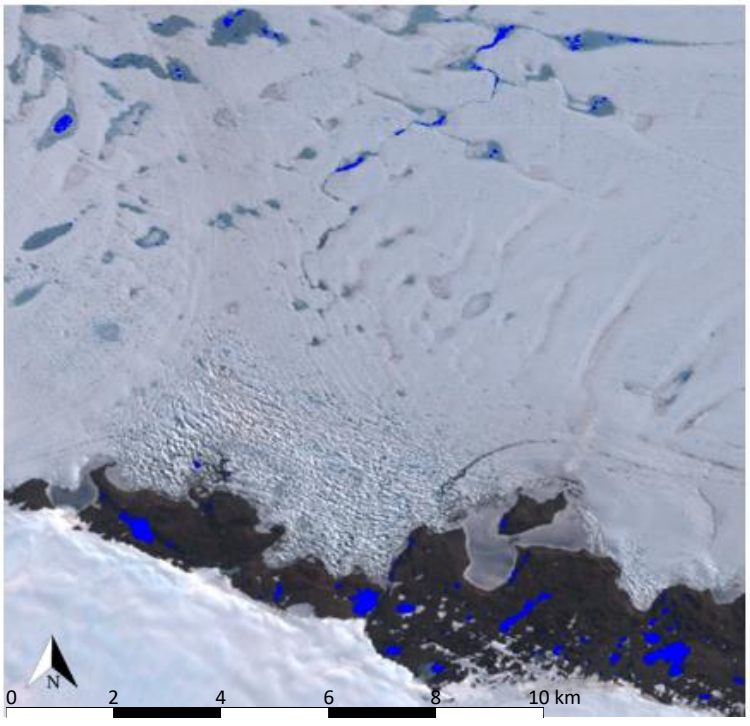

Figure 17. Lake mask (blue) extracted at NIS grounding line using red-blue NDWI threshold of 0.2. Background image is Sentinel-2 RGB false colour composite acquired on 31/01/2019: COPERNICUS/S2/20190131T080929_20190131T080941_T32DNG.

4.2 PCA-Histogram Performance

4.2i Sensitivity Analysis

The sensitivity of calculated lake and slush areas to ±10 % variation in band thresholds was evaluated for images from austral summers of 2017-2020 (Tables 14-15). For Sentinel-2 images, lake area is most sensitive to variation in SWIR (B11) and NIR (B8), varying by up to 31%, whilst slush area responds most to green (B3) and red (B4) bands (Table 14). Lake extent is most sensitive to infrared bands which confirms that PC2, which is most strongly correlated to SWIR (B11), represents lake-covered areas. Lake-covered pixels are also sensitive to the blue band (B2) despite this being a less important variable in the PC2 cluster. The Sentinel-2 PCA component matrix (Table 8) indicates that visible bands are most strongly correlated to the slush cluster (PC1) which explains greatest sensitivity of slush to green (B3) and red (B4) bands (Table 14). It is notable that both slush and lake clusters are defined by, and sensitive to, infrared radiation. Whilst previous literature emphasises use of visible bands (Sun et al., 2012), there is scope for broader investigation into the utility of infrared bands for mapping supraglacial hydrology.

The process of deriving supraglacial feature extents from Landsat 8 images demonstrates that lake area is most sensitive to NIR bands (B5) whereas slush regions respond significantly more to blue (B2) and red (B4) visible bands (Table 15). The PCA for Landsat 8 images calculates PC1, interpreted as slush pixels, to respond most strongly to red (B4) and green (B3) visible bands (Table 9). Meanwhile, the Landsat 8 PC2 is most sensitive to NIR bands (B5) which is reflected in ~20 % increase of lake extent in response to ±10 % variation in NIR bands (Table 15). The sensitivity of lake and slush areas from Landsat 8 images to threshold variability remains within reasonable limits across all tested bands except for the blue band (B2) threshold for slush areas (Table 15). Such large sensitivity of slush area to blue band threshold introduces uncertainty as to whether slush extent is calculated accurately or is artificially overestimated. The frequency distribution of Landsat 8 blue band (Figure 11a) supports this given the lack of a distinct threshold between lake and slush reflectance. This justifies the exclusion of the blue band threshold in delineating slush extent for Landsat 8 images.

		Lake Extent				Slush Extent			
		10%	-10%	Range	% change	10%	-10%	Range	% change
Blue	B2	0.654	0.572	0.082	5.65	5.74	1.52	4.22	-0.261
Green	B3	0.619	0.538	0.081	0.00	5.79	1.46	4.33	37.7
Red	B4	0.620	0.589	0.031	0.16	5.79	2.35	3.44	29.9
NIR	B8	0.811	0.370	0.441	31.0	5.65	4.66	0.989	-1.77
SWIR1	B11	0.143	0.075	0.068	19.2	6.06	5.86	0.202	-0.705

Table 14. Sensitivity of lake and slush extent to variation in Sentinel-2 band thresholds by ±10%. Range of values for upper and lower bounds calculated as well as percentage change from the original thresholds extracted from the histograms. Values highlighted in pale red demonstrate which band causes largest variation in calculated extent. All values to 3 s.f.

		Lake Extent				Slush Extent			
		10%	-10%	Range	% change	10%	-10%	Range	% change
Blue	B2	0.785	0.703	0.0821	10.9	1.87	0.0017	1.87	499
Red	B4	0.751	0.734	0.0169	2.25	1.10	0.388	0.712	97.0
NIR	B5	0.817	0.681	0.137	18.2	0.376	0.0108	0.365	97.2
SWIR1	B6	0.775	0.689	0.085	11.3	0.259	0.0334	0.225	59.8

Table 15. Sensitivity of lake and slush extent to variation in Landsat 8 band thresholds by ±10%. Range of values for upper and lower bounds calculated as well as percentage change from the original thresholds extracted from the histograms. Values highlighted in green demonstrate which band causes largest variation in calculated extent. All values to 3 s.f.

The sensitivity analysis of delineated lake and slush extents to Sentinel-2 and Landsat 8 band thresholds can be used to compare the utility of satellite images for the method developed here. Sentinel-2 based lake and slush extent estimations vary by a maximum of 31% and 38% respectively (Table 14). Lake and slush extent calculated from Landsat 8 images vary by a maximum of 18% and 499% respectively (Table 15). This introduces uncertainty in use of Landsat 8 spectral data but uncertainty is minimised by removing the blue band (B2) from calculations of slush extent based on Landsat 8 images. Significant sensitivity of slush area to a proportionately small change in a single band threshold supports the use of multiple bands in spectral thresholding. Uncertainty in lake and slush delineation using the remaining red, NIR and SWIR1 bands (B4, B5, B6) is low, justifying the continued use of Landsat 8 images. Meanwhile, low sensitivity of feature delineation to Sentinel-2 band thresholds favours use of Sentinel-2 images for accurate monitoring of East Antarctic supraglacial hydrology. However, the lower temporal resolution of Sentinel-2 images must be supplemented with higher frequency images from other satellites.

After rejection of the Landsat 8 blue band (B2), the sensitivity analysis suggests that variation in remaining threshold band values (± 10%) on average has a proportionate effect on the calculation of lake and slush area (± 9.4%) (Table 14-15). Therefore, the method developed accurately identifies supraglacial hydrological features without over-sensitivity to any individual spectral band.

4.2ii Inter-sensor Precision

The confusion matrix measures the frequency of pixels that are identified by both Landsat 8 and Sentinel-2 images, captured within 2-3 days of each other, as belonging in similar or dissimilar supraglacial feature classes (Table 16). The confusion matrix indicates the precision of supraglacial feature delineation by the PCA-histogram method using different input spectral data. Table 17 highlights that the greatest error is associated with the discrepancies in classification of slush pixels between Landsat 8 and Sentinel-2 images. This indicates greater uncertainty when drawing comparisons between the SEB contribution of slush pixels identified by different satellite sensors. However, the overall agreement of feature identification between the two satellite sensors at 62%, calculated as the mean of all class precision values, is sufficiently high to assume that the Landsat 8 and Sentinel-2 records can be combined (Table 17). The comparability of masks generated from different sensors gives a record of NIS's surface with a higher temporal resolution.

Sentinel-2 - 11/01/2018

a)	Lake	Slush	Ice	Total	PR
Lake	31855	3560	0	35415	90%
Slush	6772	4740	50244	61756	8%
Ice	0	23327	119786	143113	84%
Total	38627	31627	170030	237168	
Precision	82%	15%	70%		

Landsat 8 - 08/01/2018

Sentinel-2 - 22/12/2018

b)	Lake	Slush	Ice	Total	PR
Lake	13899	9273	0	23172	60%
Slush	0	145	310	455	32%
Ice	278	0	213263	213541	99%
Total	14177	9418	213573	237168	
Precision	98%	1.50%	99%		

Landsat 8 - 24/12/2018

Table 16a-b. Multi-class confusion matrix of pixel frequency for different supraglacial features identified in 15km^2 training region of Landsat 8 (ID: 165-110 08/01/2018 and 167-110 24/12/2018) and Sentinel-2 (ID: 080-919 11/01/2018 and 080-929 22/12/2018) images. Green-shaded cells indicate true positives i.e. where both sensors identify a pixel in the same class. Precision calculated as True Positive/ (True Positive + False Positive).

Sentinel-2

Landsat 8	Lake	Slush	Ice
Lake	0.82	0.42	0.80
Slush	0.55	0.15	0.53
Ice	0.91	0.50	0.88

Average precision = 0.62

Table 17. Precision matrix for evaluating performance of PCA-histogram feature identification method using different satellite sensors. Precision (to 2 s.f.) calculated as True Positive / (True Positive + False Positive) for each class. Pixel frequency data from Table 16a-b combined to calculate overall precision. Green-shaded cells correspond to precision > 50%. Yellow-shaded cells correspond to precision < 50%.

4.3 Surface Energy Balance Model Results

Austral summertime SEB is dominated by shortwave radiation transferring energy to the ice shelf surface, whereas longwave radiation re-radiates energy from the surface (Figures 18-19). During daylight hours, the latent heat flux becomes a significant source of heat loss in the SEB by evaporation or sublimation. The average energy flux at lake, slush and clean ice pixels is plotted for each meteorological data acquisition time i.e. every 6 hours (Figure 20a-d). This facilitates comparison of the extra energy flux for lakes and slush at different times of day to identify trends in sensitivity to incoming shortwave radiation.

For the majority of the day, clean ice areas have net negative energy balance confirming high reflection of incoming shortwave radiation. However, energy reflected or emitted at each clean ice pixel is on average 2 times less than average absorption at each lake pixel (Figure 23). This demonstrates the importance of considering SGL and slush SEB contribution in relation to clean ice. All values reported in the following section have been differenced with clean ice energy contribution giving extra energy contributed as a result of the presence of meltwater features.

Average extra energy absorbed at lake and slush pixels peaks at 1200 between 150-200 W/m^2 and 0-50 W/m^2 respectively (Figure 20c). As expected, mean energy flux at lake and slush pixels is lowest at midnight varying between -20 to -100 W/m^2 and -80 to -140 W/m^2 respectively (Figure 20a). The greatest magnitude variation in average energy absorbed at pixels occurs at 0600 (Figure 20b). Overall, mean extra energy absorbed by lake and slush pixels at each time of day is similar between years, varying over the course of a day from 0 W/m^2 at night to 250 W/m^2 at peak insolation for lake pixels and 0 W/m^2 at night to 100 W/m^2 at peak insolation for slush pixels. The sum of these instantaneous mean values through time gives an overall daily energy absorption of 8.7 MJ/m^2 and 0.54 MJ/m^2/day for SGL and slush areas.

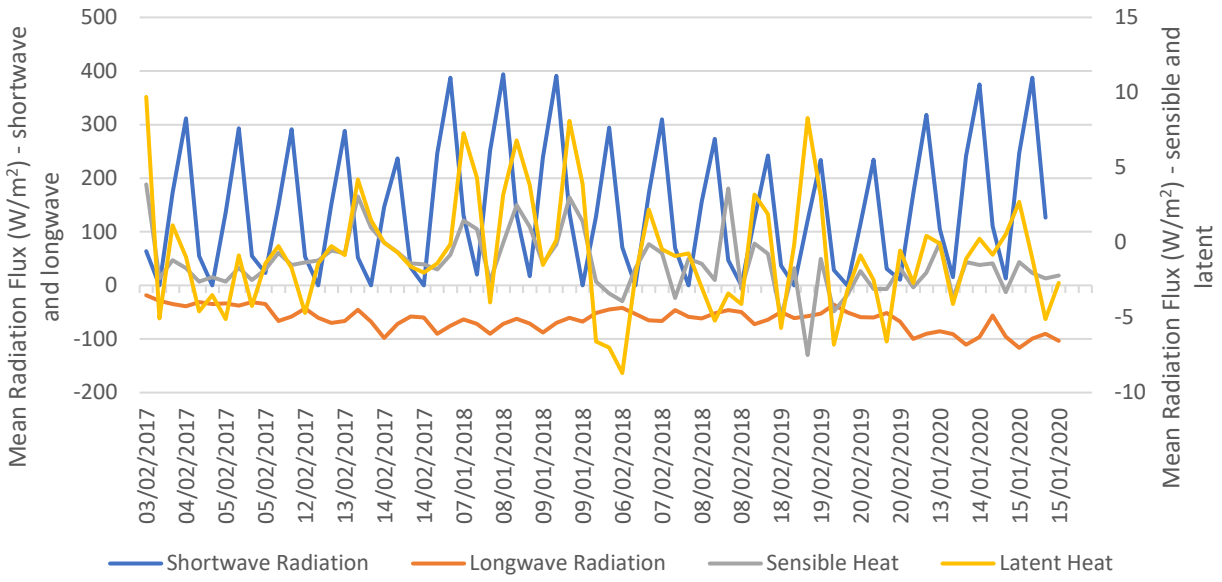

Figure 18. Mean energy balance components at lake pixels on NIS. Instantaneous measurements of each energy flux recorded at 00:00, 06:00, 12:00 and 18:00. Shortwave, longwave (left hand axis), sensible and latent heat (right hand axis) calculated from SEB model for the most recent image from each austral summer 2017 – 2020.

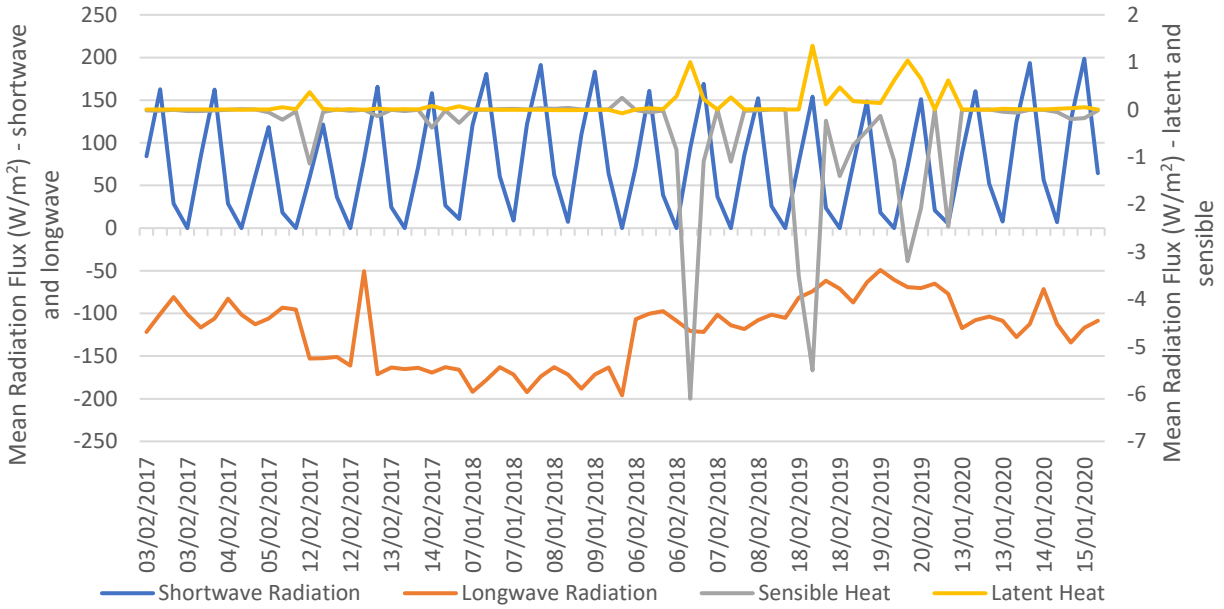

Figure 19. Mean energy balance components at slush pixels on NIS. Instantaneous measurements of each energy flux recorded at 00:00, 06:00, 12:00 and 18:00. Shortwave, longwave (left hand axis), sensible and latent heat (right hand axis) calculated from SEB model for the most recent image from each austral summer 2017 – 2020.

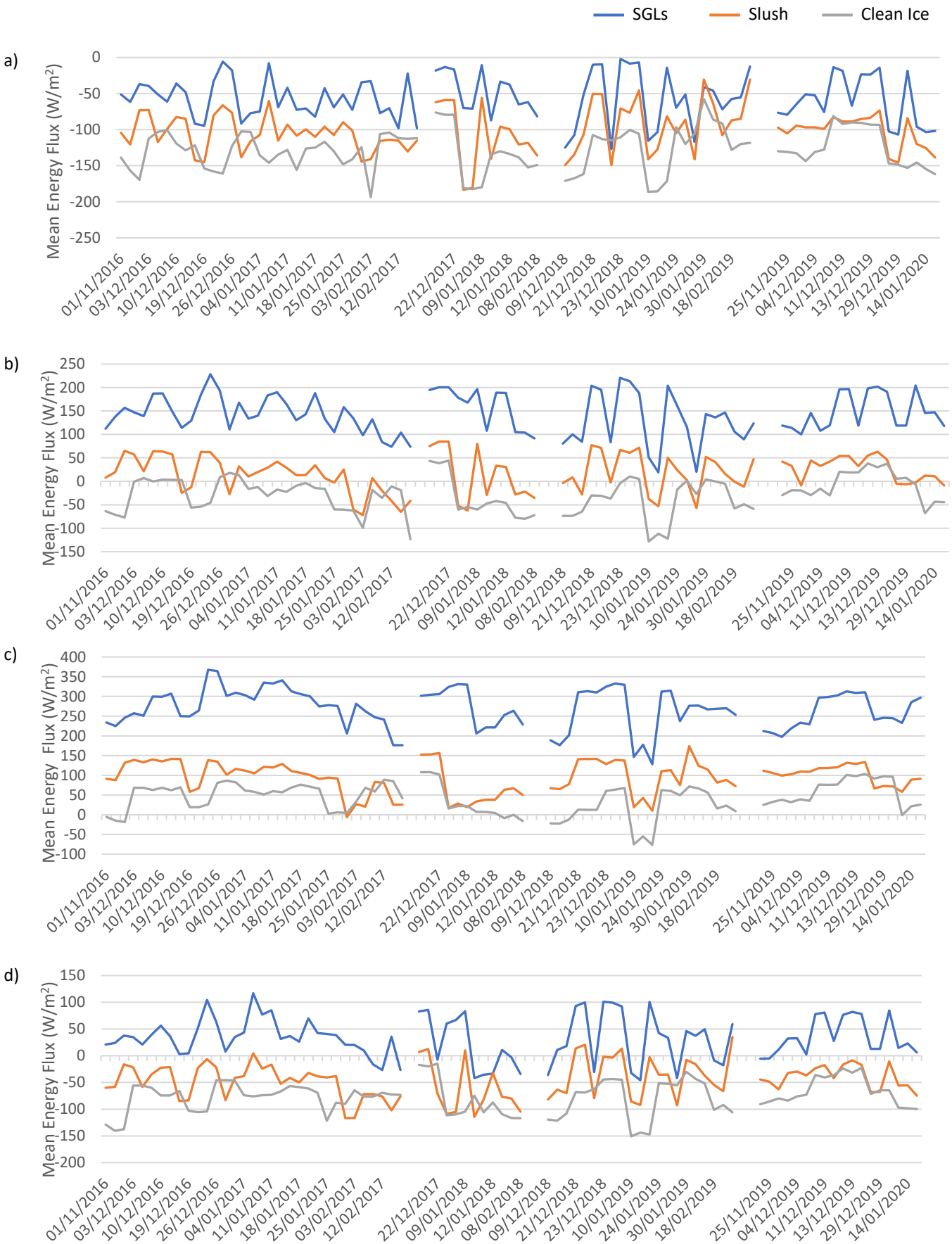

Figure 20. Mean energy balance at lake, slush and clean ice pixels at (a) 00:00 (b) 06:00 (c) 12:00 and (d) 18:00 for austral summers of 2017-2020. Mean energy balance at each time calculated for all available Landsat 8 and Sentinel-2 images as well as one day either side.

The SEB model calculates total energy flux to be the most sensitive to variation in shortwave radiation. Average daily shortwave energy flux varies synchronously with variability in GFS incoming shortwave raditation data (Figures 18-19). Lake and slush pixels have net positive shortwave radiation absorption with mean values of 13.4 MJ/m^2/day and 7.2 MJ/m^2/day respectively in the austral summer of 2019 (Figure 18-19). Lake and slush pixels have mean longwave energy transfer of -1.5 MJ/m^2/day and -3.1 MJ/m^2/day over the same austral summer (Figure 18-19). Slush is determined to be an important supraglacial feature for emitting longwave radiation at peak incident radiation times but also throughout the night (Figure 20). Overall, SGL and slush regions have a net positive contribution to SEB given that daily longwave emitted radiation is an order of magnitude smaller than absorbed shortwave radiation.

Where net sensible heat flux is positive, energy is directed away from the surface to the surrounding atmosphere. Over lake and slush regions, net sensible heat flux is positive but near negligble as a proportion of total energy balance (Figure 18-19). Across the whole slush region, an average of 0.49 KJ/m^2/day of sensible heat energy is transferred to the atmosphere. SGLs beneath a stable air column (Ri > 0) emit 0.60 KJ/m^2/day of sensible heat whilst SGLs beneath an unstable air column (Ri < 0) emit a much higher average of 420 KJ/m^2/day. The intuitive explanation for this is that stronger winds drive continual replacement of air above the lakes, maintaining the temperature gradient and facilitating sensible heat emission later into the evening.

Net positive latent heat represents a gain of thermal energy at the surface due to melting. Negative values indicate heat loss through freezing. For 2019, the -400 KJ/m^2 average daily loss at SGLs under a stable air column in the late austral summer might indicate that these lakes are in the process of refreezing. Meanwhile, lakes in areas where the near-surface air column is turbulent (Ri < 0) and unstable absorb an extra 660 KJ/m^2/day due to high melting rates. The -1.12 KJ/m^2 daily latent heat loss at slush areas is likely to be the energy required to maintain the ice crystals in interstitial water.

The daily sum of SEB across the whole lake, slush, and ice regions is plotted through time in Figures 21-22. The sum of SEB is calculated using GFS meteorological data for the 72-hour period around each image acquistion time i.e. 24 hours either side of each satellite image. Total SEB across the clean ice area is calculated to show the net significance of lake and slush regions for overall energy balance (Figure 21). The daily total energy balance for clean ice, which constitutes ~80.0 % of the study-site by area, dominates the energy balance of NIS. Although SGLs only constitute ~4.8 % of the study-site area, Figure 21 demonstrates the significant energy absorption that occurs across the

whole lake mask. To more clearly identify trends in SGL and slush contribution, net SEB for clean ice is not plotted in Figure 22.

Total energy absorbed by the entire lake-covered area decreases over austral summers of 2017 – 2020. Total energy absorbed across the whole slush region remains constant inter-annually. Figure 22 clearly identifies the austral summer of 2017 as a year where a particularly high 1.6 GJ/day was absorbed across the whole 78 km^2 lake-covered region on NIS. Meanwhile, the net energy absorption across the 103 km^2 slush region was particularly high (up to 0.8 GJ/day) in the austral summer of 2019 (Figure 22). However, the *mean* energy absorbed at lake pixels was not especially high in 2017, nor was *mean* absorption at slush pixels especially high in 2019 (Figure 23). Inter-annual variability in net energy absorbed across SGL compared to slush regions is not the result of changes in mean absorptive capacity of lake or slush pixels (Figure 23). Instead, total energy transfer is largely controlled by inter-annually variable lake versus slush *extent* which is likely the result of climate conditions, ice shelf topography, and firn hydrology.

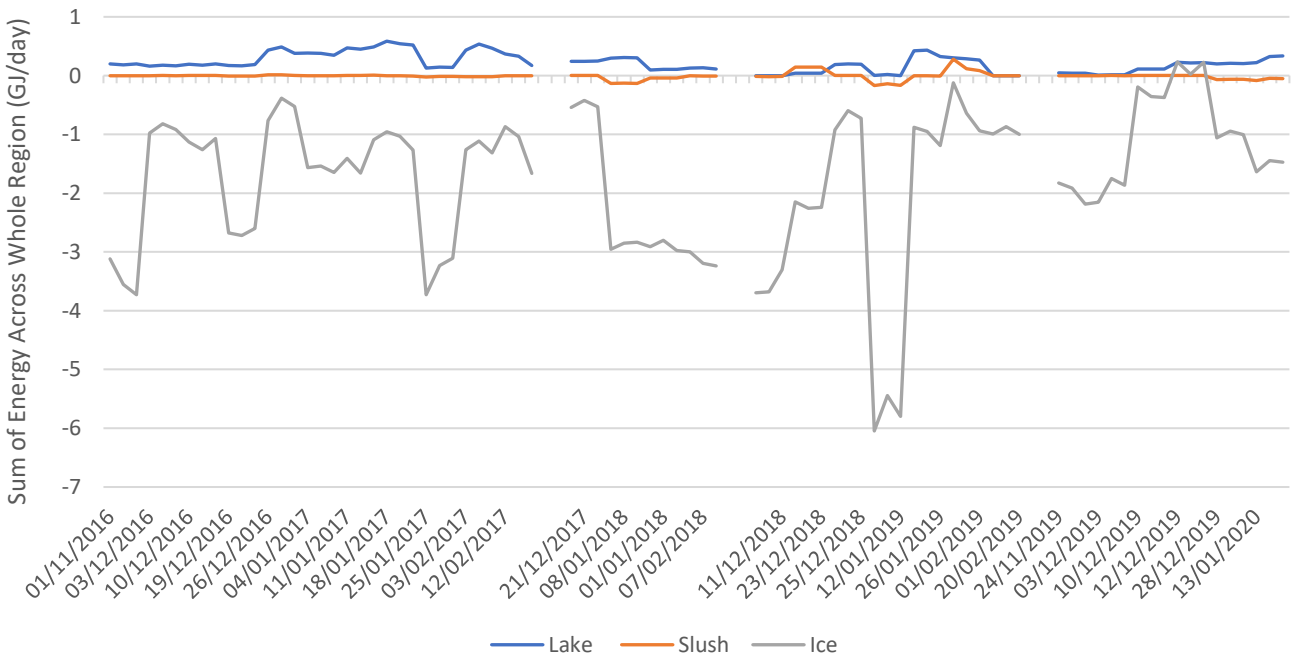

Figure 21. Daily sum of surface energy balance across whole lake, slush and clean ice regions for austral summers of 2017-2020. Total energy balance across whole NIS calculated for the day of Landsat 8 or Sentinel-2 image acquisition and one day either side.

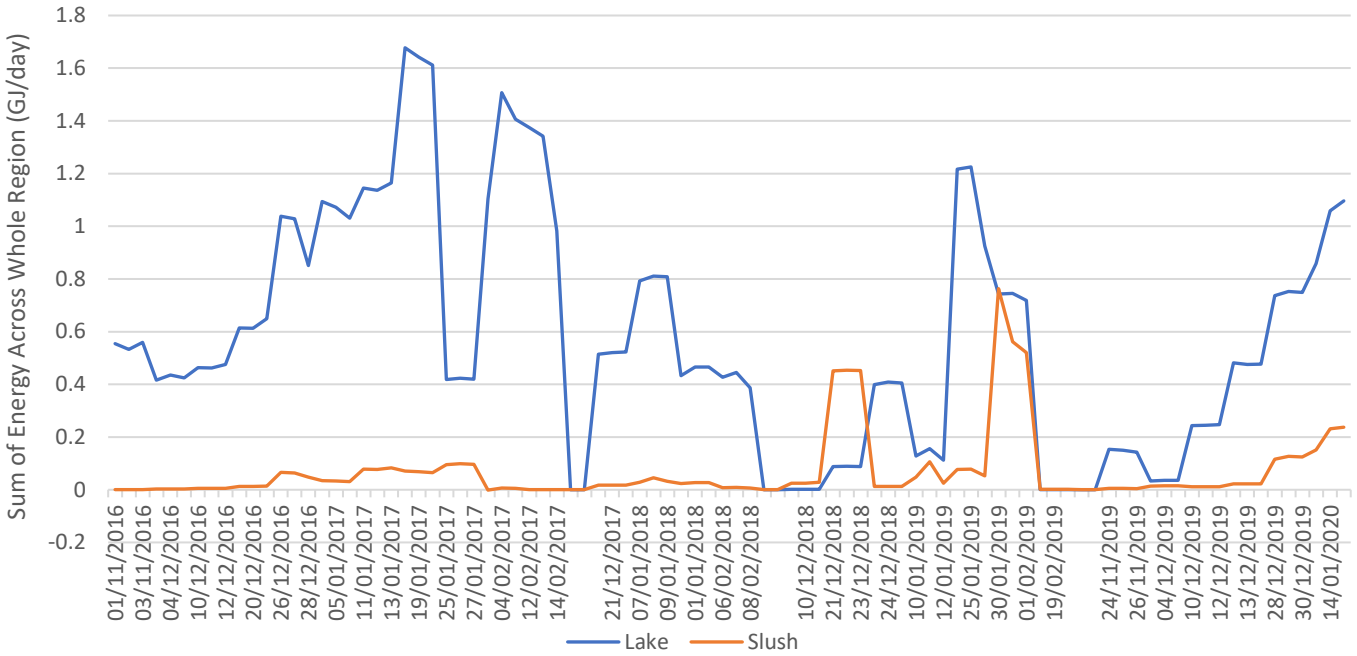

Figure 22. Daily sum of surface energy balance across whole slush and lake regions for austral summers of 2017-2020. Total energy balance across NIS calculated for the day of Landsat 8 or Sentinel-2 image acquisition and one day either side.

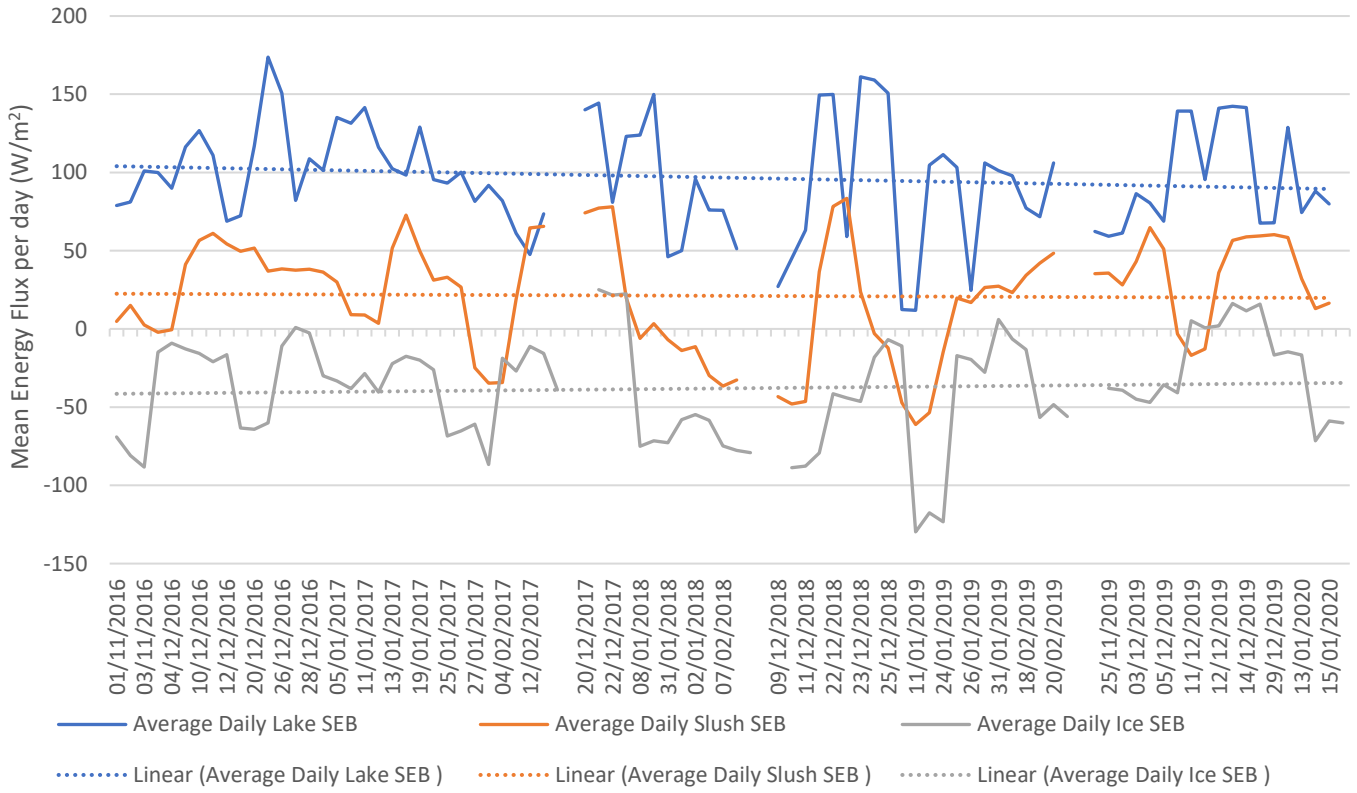

Figure 23. Daily mean energy flux at lake, slush and clean ice pixels for austral summers of 2017-2020. Mean energy balance calculated for the day of Landsat 8 or Sentinel-2 image acquisition and one day either side. Dashed line gives linear trendline across all seasons.

4.4 Surface Energy Balance Model Verification and Validation

4.4i Verification of Energy Balance Model

To verify that the SEB model is sensitive to meteorological variability, modelled output energy fluxes are calculated using different forecast data for the same satellite image. Figures 24-28 plot meteorological variability of Global Forecast System data in relation to modelled average shortwave and longwave radiation fluxes for lake and slush pixels. Four measurements of GFS data (6-hourly) from one day either side of Sentinel-2 and Landsat 8 images in mid-melt season of 2017-2020, are used to run the SEB model. This assumes that, whilst meteorological conditions are sufficiently variable to affect SEB, the distribution of lake and slush pixels remains unchanged over each 3-day period. The lack of direct observations of rapid SGL hydrofracture-driven drainage on NIS suggest that a single satellite image is representative of the surface over 3 days.

The net modelled shortwave flux varies linearly across lake and slush areas with incoming shortwave radiation. Figure 27 suggests that, for Landsat 8-based SEB calculations, the sensitivity of modelled shortwave flux to incoming solar radiation is strongest over lake pixels. Meanwhile, modelled longwave flux over lake pixels is sensitive to air temperature variation. Anomalously high air temperatures reached on 01/02/2019 and 10/01/2018 correspond to greater longwave radiation absorption on average at lake pixels (less negative longwave flux values – Figures 24 and 27). Under warmer conditions SGLs are more efficient net absorbers of longwave radiation and therefore transfer more energy to NIS (Figure 26). Longwave radiation flux over lake and slush gradually becomes less negative from 2017-2020 (greater longwave absorption) in line with slightly increased air temperatures. Even with large anomalous air temperature or humidity readings (e.g. 16/01/2017), longwave flux responds proportionately to the magnitude of meteorological forcing. Therefore, modelled longwave flux through time can be interpreted in the context of on-going local increases in air temperature.

Modelled SEB flux is verified as being sensitive to input meteorological data with greater sensitivity at lake pixels compared to slush pixels. More importantly, images acquired from Sentinel-2 and Landsat 8 datasets are confirmed to reasonably predict surface features over the course of a 3-day period. Justifying the extrapolation of lake and slush masks over multiple days is essential for providing a longer temporal dataset for running the SEB model.

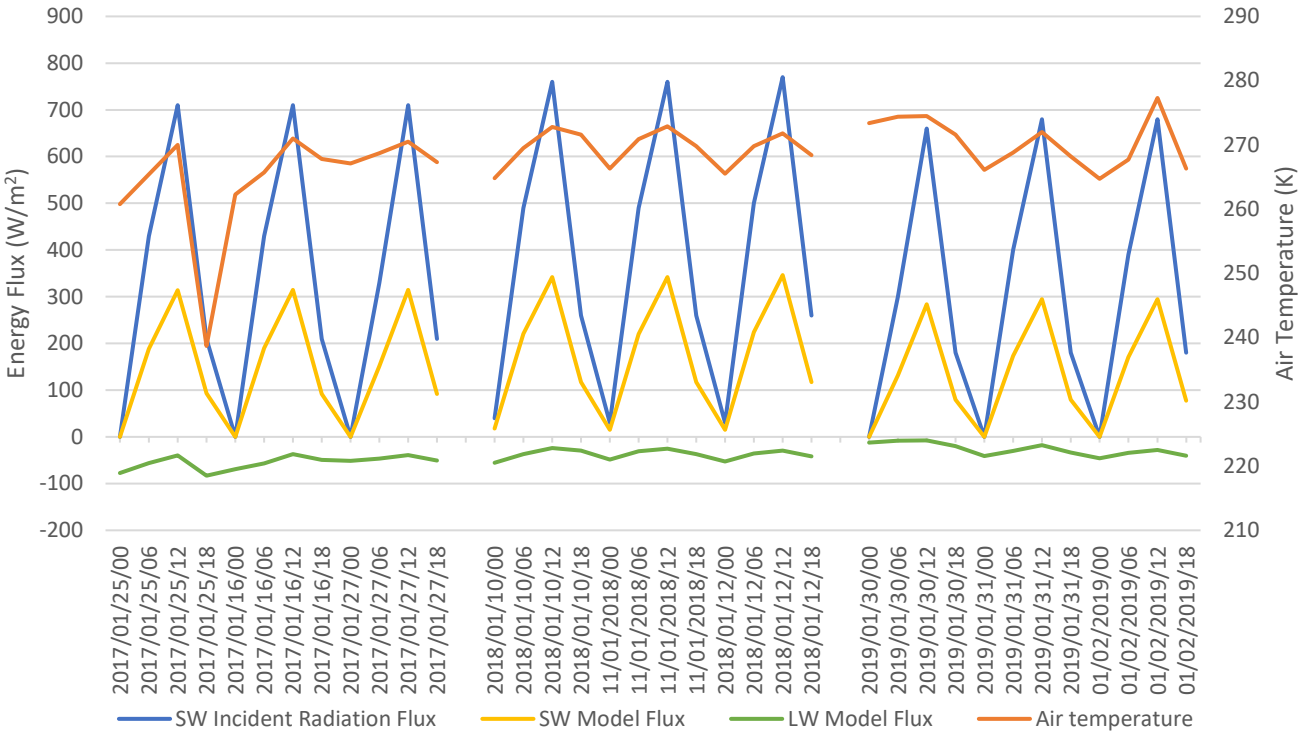

Figure 24. Modelled average shortwave and longwave radiation flux at lakes compared to Global Forecast System Data at 6-hourly intervals. Data plotted for date of Sentinel-2 image acquisition and one day either side. Wind speed is not displayed because variability was negligible. Timestamp in format YYYY/MM/DD/HH. See Table S5 for data.

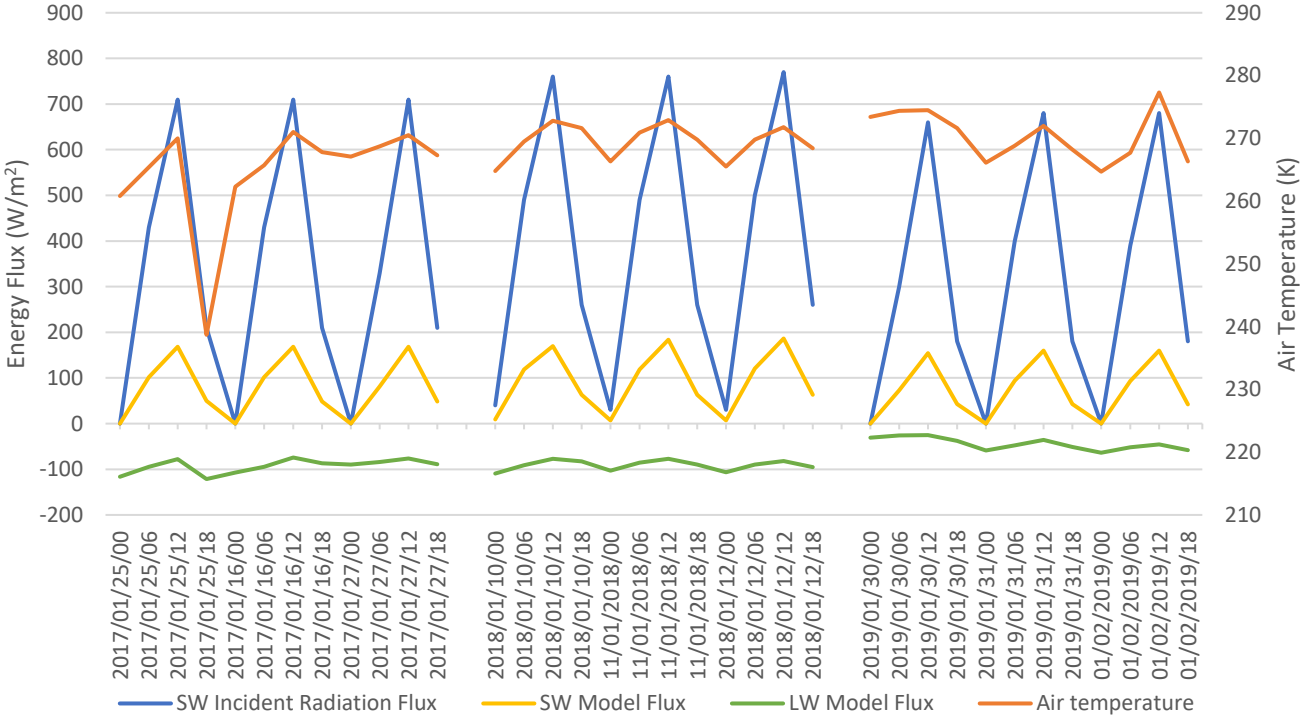

Figure 25. Modelled average shortwave and longwave radiation flux at slush compared to Global Forecast System Data at 6-hourly intervals. Data plotted for date of Sentinel-2 image acquisition and one day either side. Wind speed is not displayed because variability was negligible. Timestamp in format YYYY/MM/DD/HH. See Table S5 for data.

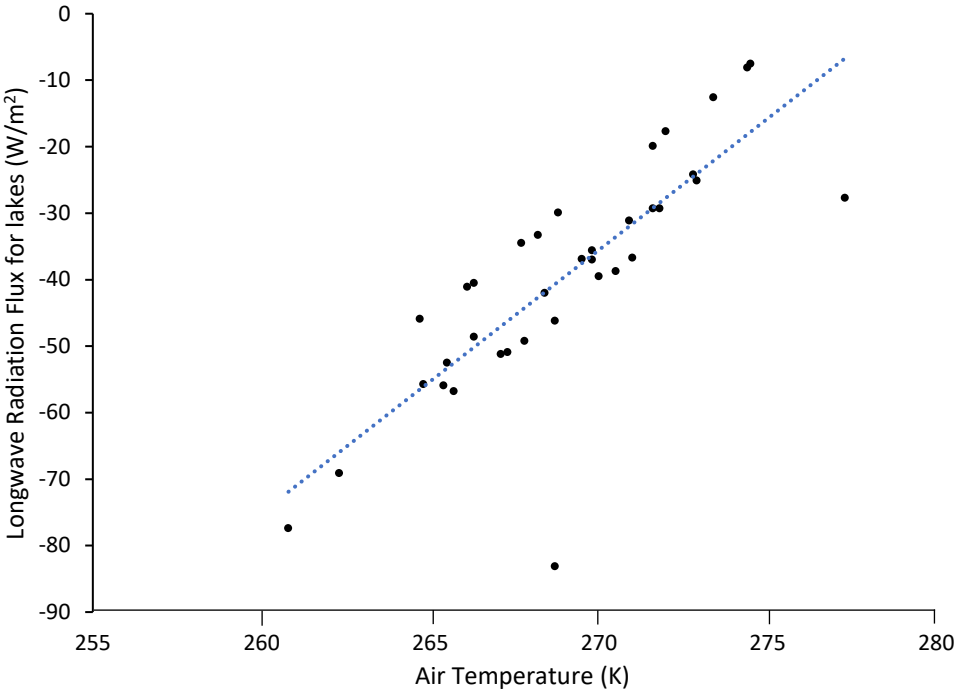

Figure 26. Modelled longwave radiation over lakes against air temperature using GFS and Sentinel-2 data. As air temperature increases, net longwave radiation emission increases. Increased longwave radiation emission is likely the result of the temperature increase of the surface pixel.

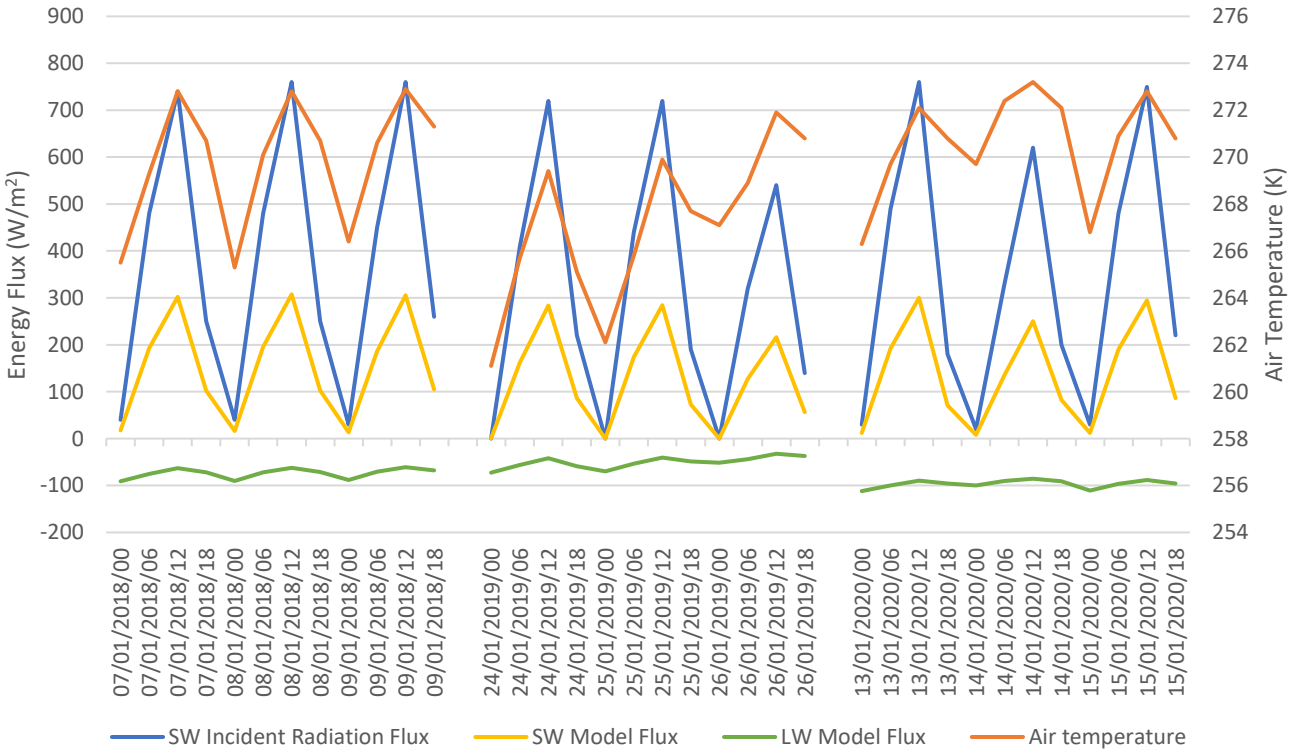

Figure 27. Modelled average shortwave and longwave radiation flux at lakes compared to Global Forecast System Data at 6-hourly intervals. Data plotted for date of Landsat 8 image acquisition and one day either side. Wind speed is not displayed because variability was negligible. Timestamp in format YYYY/MM/DD/HH. See Table S6 for data.

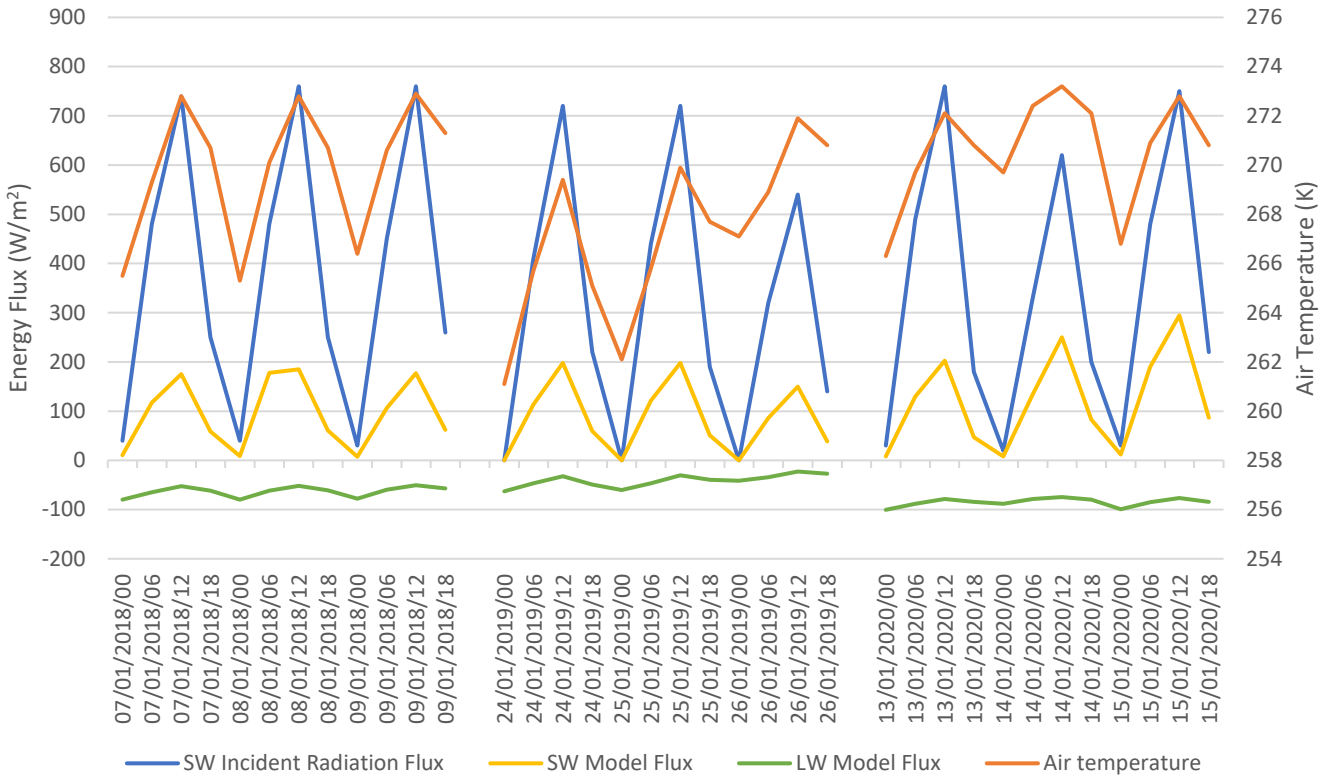

Figure 28. Modelled average shortwave and longwave radiation flux at slush compared to Global Forecast System Data at 6 hourly intervals. Data plotted for date of Landsat 8 image acquisition and one day either side. Wind speed and specific humidity are not displayed because variability was negligible. Timestamp in format YYYY/MM/DD/HH. See Table S6 for data.

4.4ii Validation of Energy Balance Results

The performance of the SEB model is validated by statistically comparing the modelled extra energy absorbed by lakes and inferred energy transfer derived from SGL volume (Table 18). Lake volume, calculated following Pope et al. (2016), is scaled by specific heat capacity (4200 J/kg °C) and density of water (997 kg/m^3) to estimate inferred energy transferred to create SGLs on Nivlisen. Calculated water depth per pixel is scaled by the satellite band spatial resolution to give depth per square metre.

Cumulative energy absorbed over an austral summer across the whole lake region is modelled to vary between 0.12 GJ and 3.0 GJ for 2017-2020 (Figure 29). Total energy transfer required to form the observed peak lake volume varies between 0.45 GJ and 9.1 GJ for 2017-2020. The Nash-Sutcliffe Efficiency value of 0.922 supports the conclusion that the modelled total energy absorption at SGLs matches the inferred dataset well. Furthermore, the normalised RMSE, which performs well for small sample sizes ($n < 20$), has a residual variance of less than 0.5 which indicates the SEB model results are sufficiently accurate to predict inferred energy absorption (Chai and Draxler, 2014).

Measure of Model Performance	Formula	Value	Significance	Interpretation
R^2	$1-\frac{\sum_{i=0}^{n}(OBS-MOD)^2}{\sum_{i=0}^{n}(OBS-\overline{MOD})^2}$	0.2588 p = 0.11	p < 0.05	Linear regression model not statistically significant.
Nash-Sutcliffe Efficiency (NSE)	$1-\frac{\sum_{i=0}^{n}(OBS-MOD)^2}{\sum_{i=0}^{n}(OBS-\overline{OBS})^2}$	0.9221	NSE ≈ 1	Good match of model to observed data (McCuen et al., 2006).
NRMSE	$\sqrt{\frac{\sum_{i=0}^{n}(MOD-OBS)^2}{n}}/\overline{OBS}$	0.4729	Variance < 0.5	Lower values indicate less residual variance. Normalised RMSE works for small sample size (Chai and Draxler, 2014).

Table 18. Statistical measures of SEB model performance in predicting observed values of total energy absorption across the entire lake region on NIS for austral summers of 2017-2020. Observed values of total energy absorption at SGLs derived from peak lake volume (m^3) using Equation 14. 'OBS' – observed values and 'MOD' – modelled values.

Regression of inferred energy stored in lake volume at the end of the melt season with cumulative SGL energy absorbed across the whole melt season gives the linear correlation coefficient (R^2) of 0.2588 (Figure 29). The weak correlation between modelled and inferred energy is not significant at the 1% level. Furthermore, Figure 29 demonstrates that inferred energy transfer is consistently an underestimate of the modelled energy transfer by approximately ~1.5 times which is likely a result of lake volume leakage (Section 5.2i). The high NSE and significant NRMSE values indicate the sensitivity of the SEB model to variable supraglacial conditions but uncertainty remains over the systematic errors causing discrepancies between modelled and inferred energy transfer.

Figures 30a-d show cumulative trendlines derived from extrapolating modelled energy absorption for days without input spectral data. Over different austral summers, the best-fit trendline for cumulative energy absorption varies between linear, exponential and polynomial growth (Figure 30). Across a whole typical melt season, the cumulative energy would be expected to follow an "s-shaped" cumulative frequency curve, as seen in Figure 30c. Figures 30a, 30b, and 30d do not follow the typical "s-shaped" curve indicating that the data collected in 2017, 2018 and 2020 only represent a section of the whole cycle of lake evolution. The evolution of lake area between satellite image acquisitions represents a significant source of uncertainty in this approximation method (Section 5.2i).

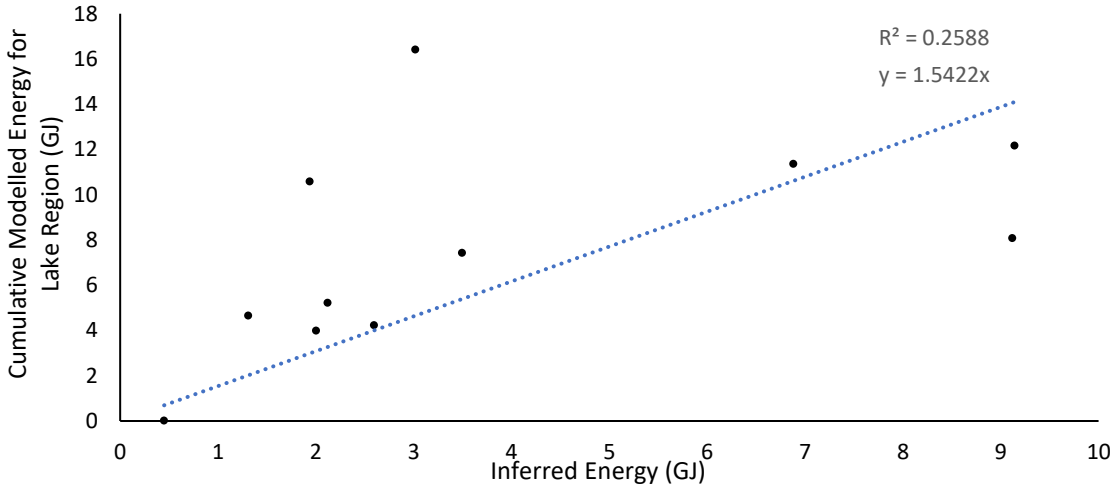

Figure 29. Cumulative modelled surface energy balance (GJ) across whole lake region compared to inferred energy (GJ) transfer from peak lake volume (m^3) (Equation 14). Lake volume calculated for the latest images in the melt season – i.e. to get maximum lake volume. Cumulative modelled energy calculated up until time of image capture used for lake volume calculation.

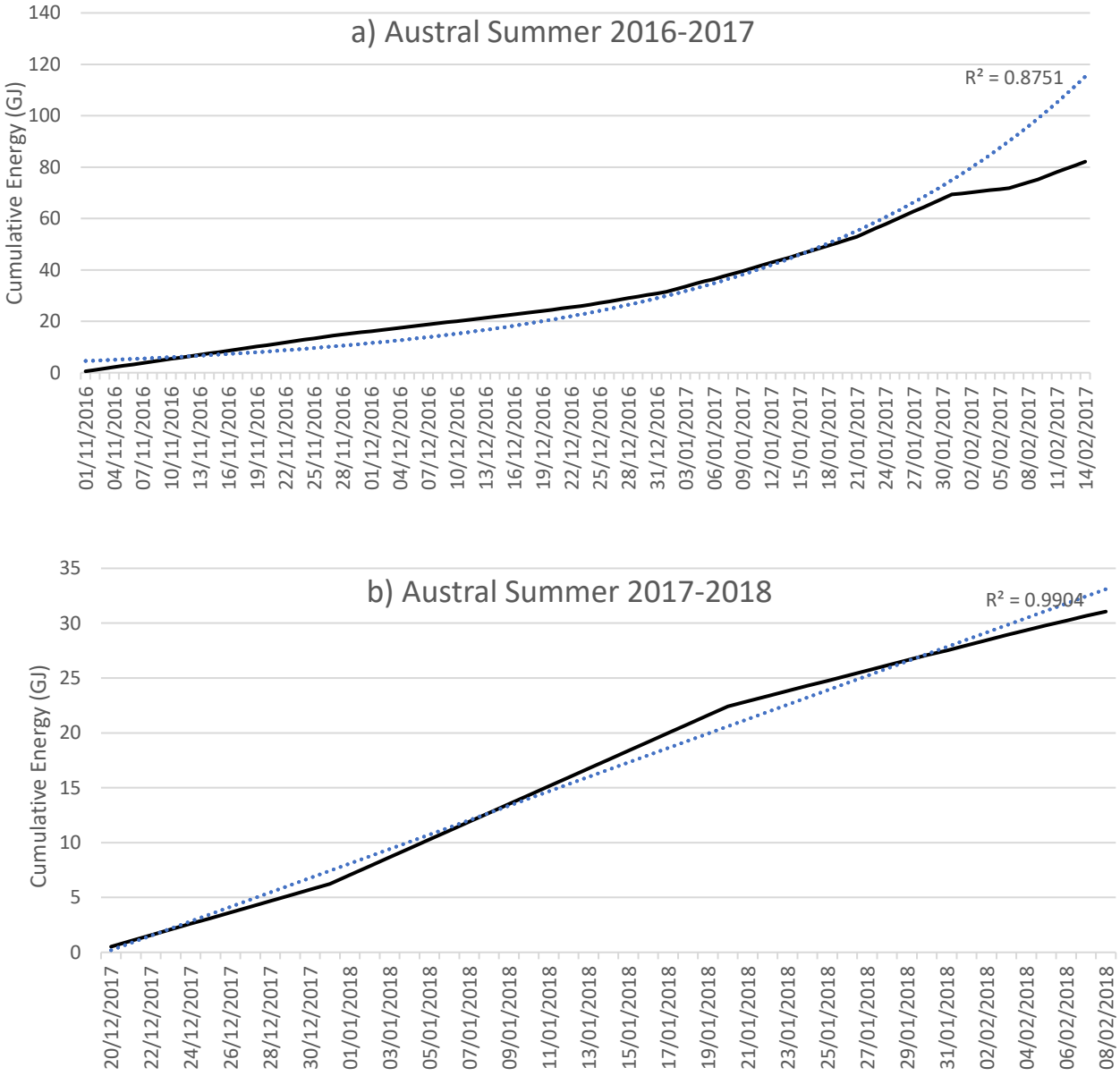

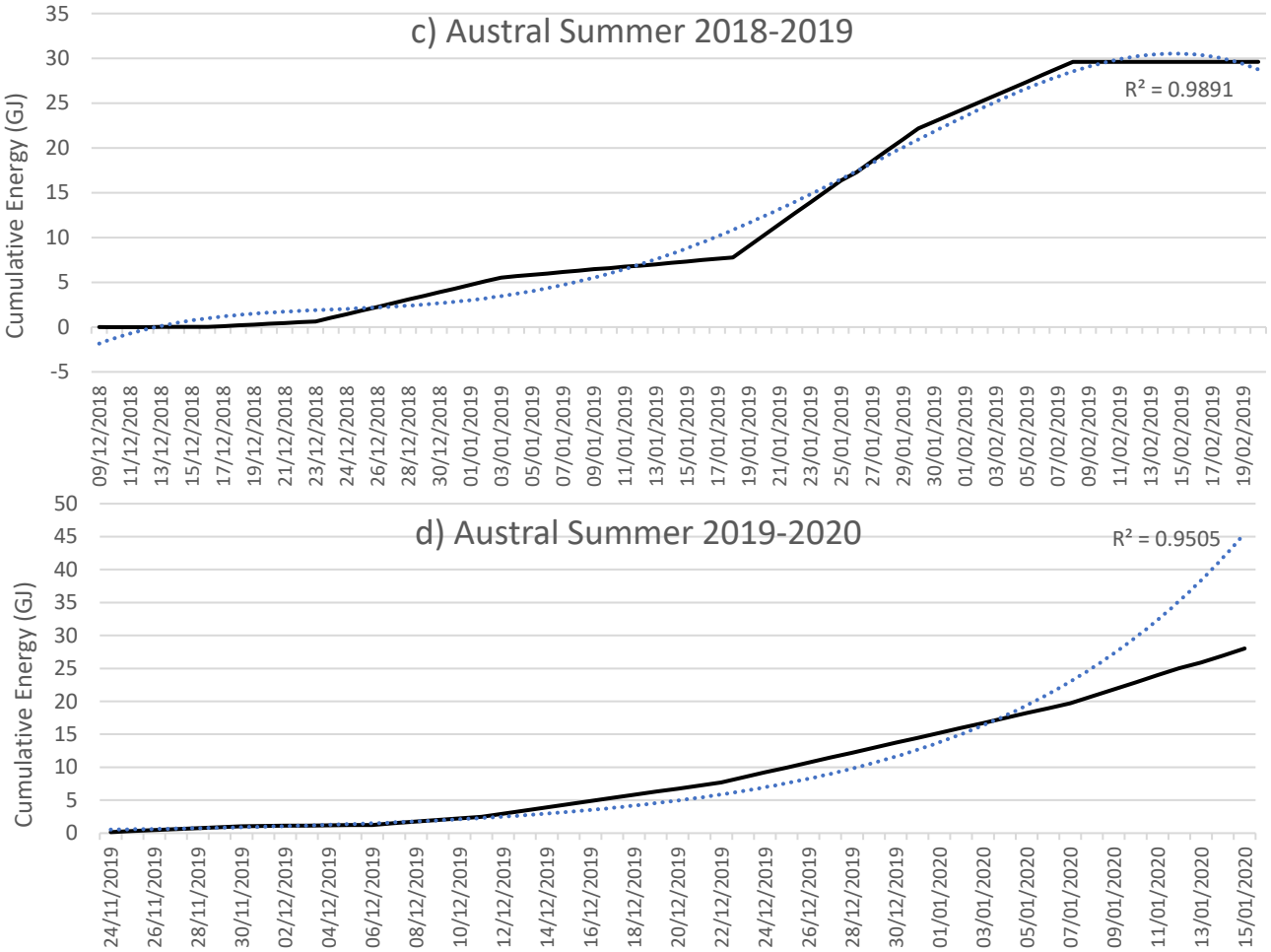

Figure 30a-d. Cumulative modelled energy absorption across whole lake region in a) 2016-2017, b) 2017-2018, c) 2018-2019 and d) 2019-2020. Dashed lines are best-fit trendlines with R^2 to indicate model trendline fit to data – a) and d) exponential trend, b) linear trend, c) polynomial order 3 trend.

4.5 Summary of Results

The PCA extracts two PCs which indicate the spectral bands that are useful in distinguishing SGL and slush pixels in Landsat 8 and Sentinel-2 imagery. Application of spectral reflectance thresholds give an average lake area of 53.6 km^2 and average slush area of 65.6 km^2 over 2017-2020. These estimates are more accurate than NDWI methods which underestimate SGL extent by an average of 122% across all images. Furthermore, the PCA successfully extracts spectral band thresholds which not only improve accuracy, but also reduce over-sensitivity of supraglacial feature extraction to a single spectral band. On an average day across the austral summers of 2017-2020, the mean energy absorbed by lake and slush areas relative to clean ice is ~ 8.7 MJ/m^2/day and ~0.54 MJ/m^2/day (Figure 23). Mean energy absorption has remained relatively constant inter-annually indicating that variation in net energy transfer across the whole of NIS is driven by lake and slush extent. The suggestion that the variable contribution of lake and slush areas to net energy transfer to NIS is related to extreme meteorological conditions is discussed in Section 5.

5. Discussion

5.1 Principal Components Analysis

The PCA, determined from Sentinel-2 and Landsat 8 imagery, identifies orthogonal components which define the total spectral variability of supraglacial features at the NIS study-site region (Tables 8-9). Two PCs were extracted from Sentinel-2 and Landsat 8 images as important factors for describing supraglacial variability. PC1, accounting for the majority of spectral variability across the ice shelf surface, represents the slush cluster with high reflectance in visible bands and relatively low reflectance in SWIR bands (Tables 10-11). PC2 is negatively correlated to visible spectral bands and positively correlated to SWIR (Tables 10-11). As PC2 increases, the absorption of visible bands increases (reflectance decreases) and temperature of the observed surface increases (high emission in the infrared). Such spectral properties described by PC2 are likely to represent water-saturated pixels which absorb most visible light and release latent heat during melting. These results are consistent for both Sentinel-2 and Landsat 8 satellite imagery which indicates that PCA is a useful method for spectral classification, regardless of the original multispectral satellite used.

Image Date	RGB Image	SGL (blue) and slush (red) mask
31/01/2019	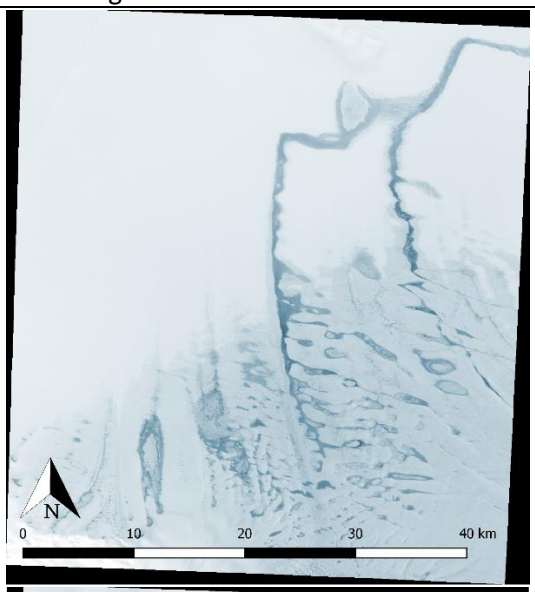	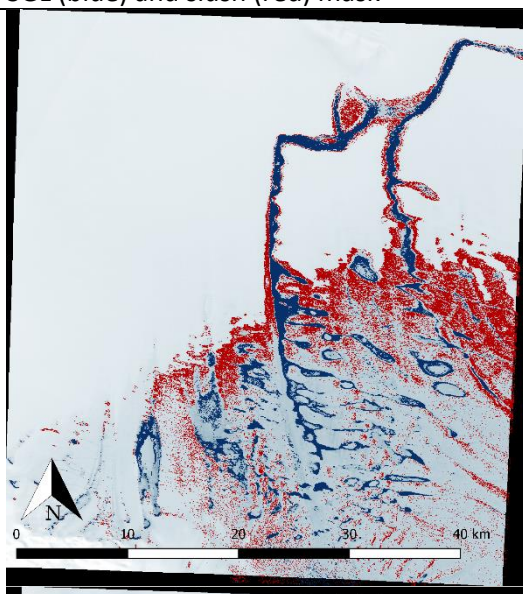
11/01/2019	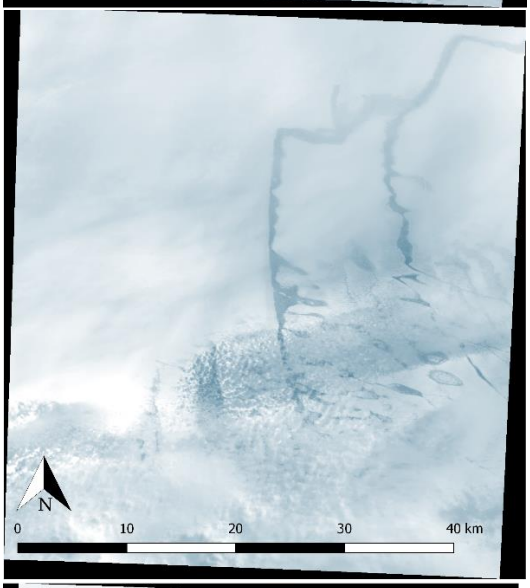	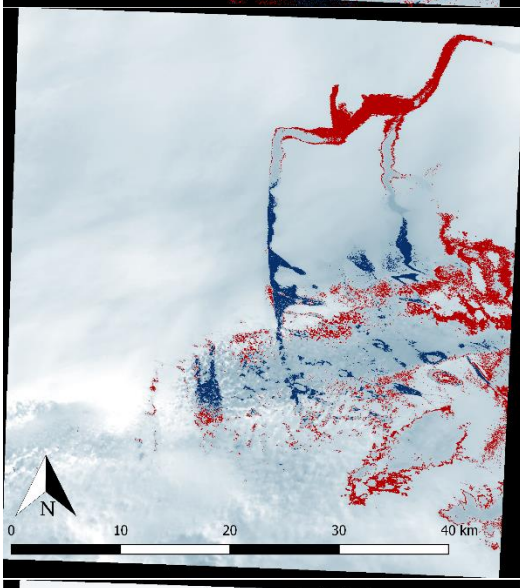
28/01/2018	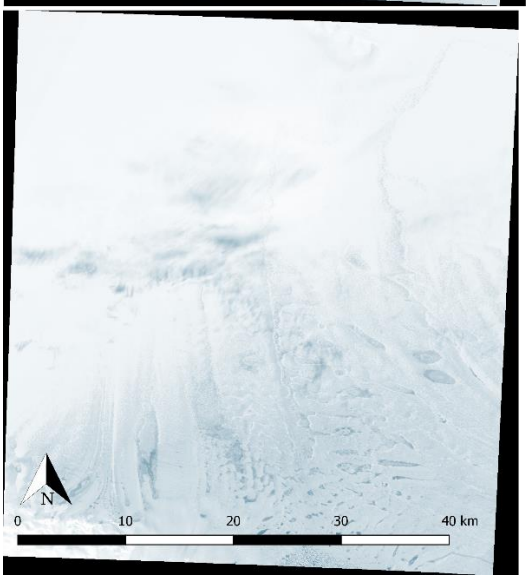	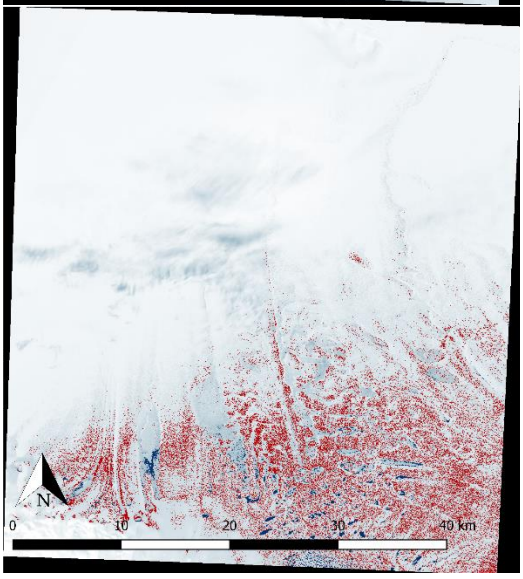

11/01/2018

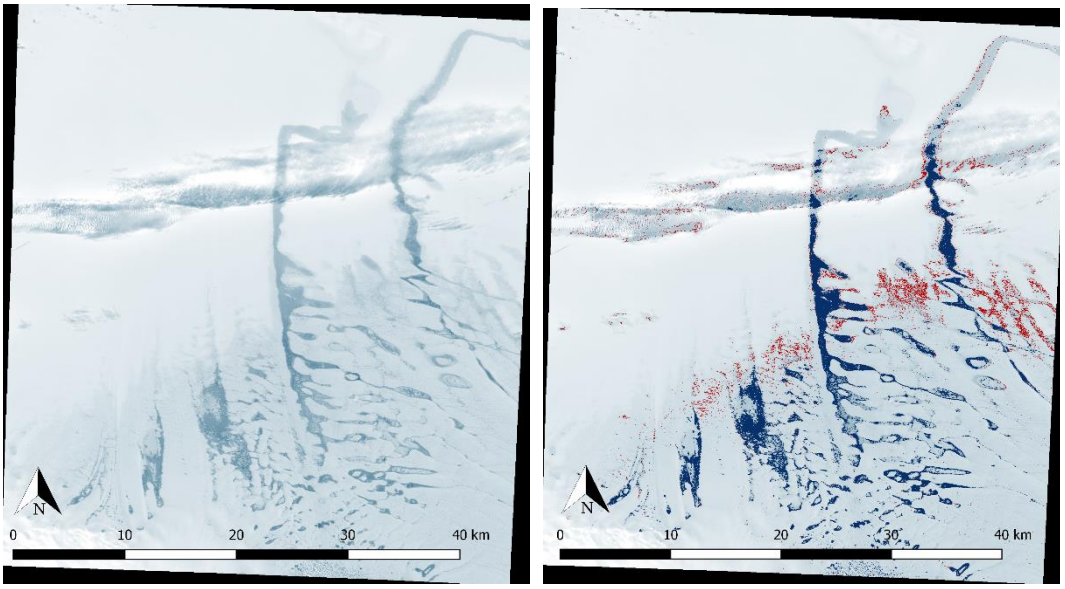

26/01/2017

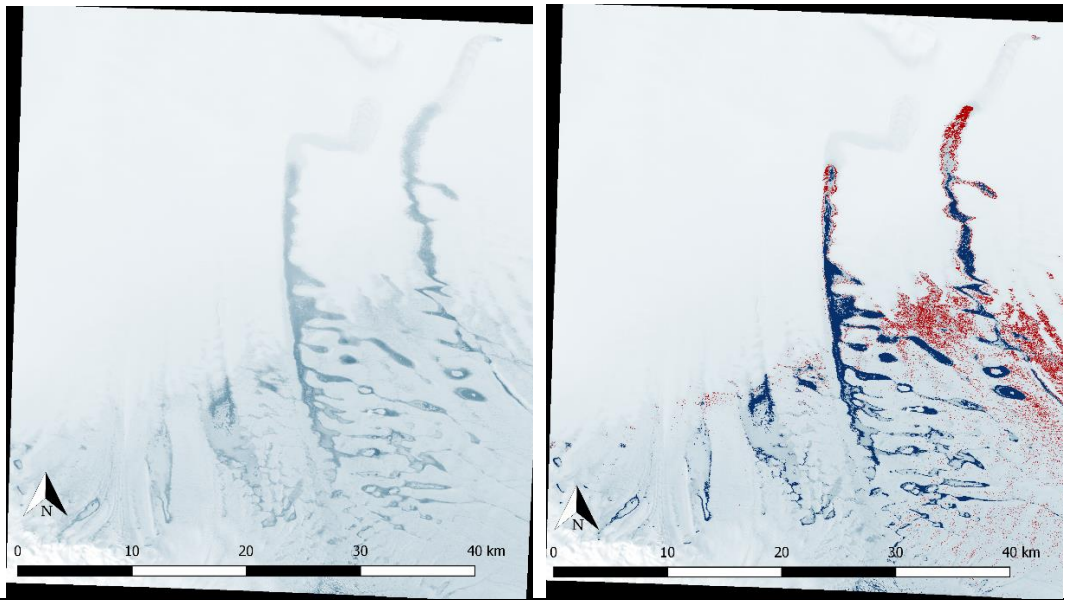

Figure 31. False colour RGB Sentinel-2 images compared to lake (dark blue) and slush (red) masks determined using PCA-histogram method. Despite evidence of cloud in some images, the PCA remains successful at identifying supraglacial features.

Image Date	RGB Image	SGL (blue) and slush (red) mask
14/01/2020	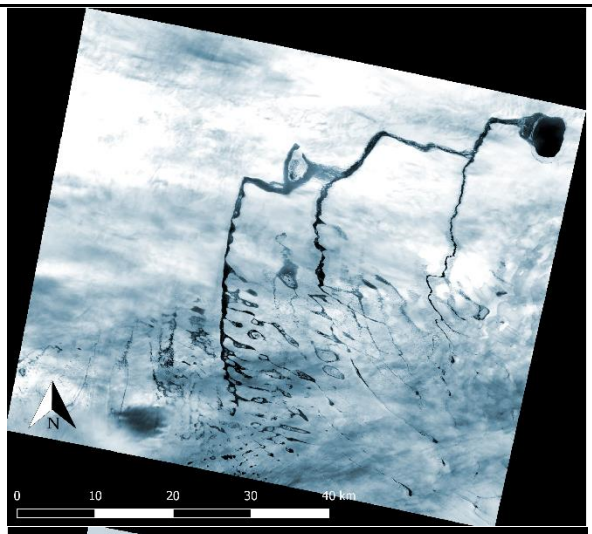	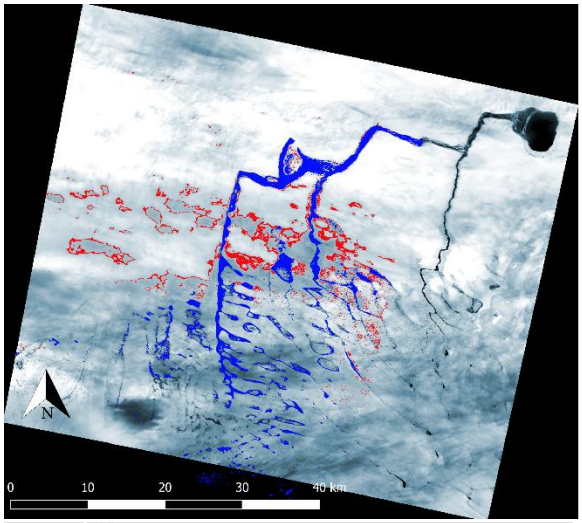
19/02/2019	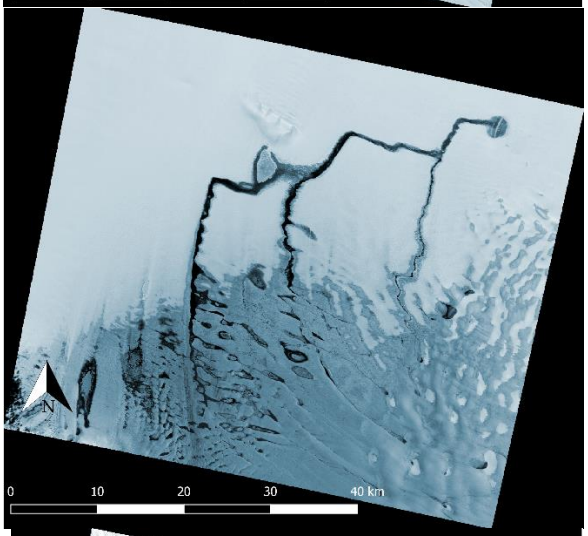	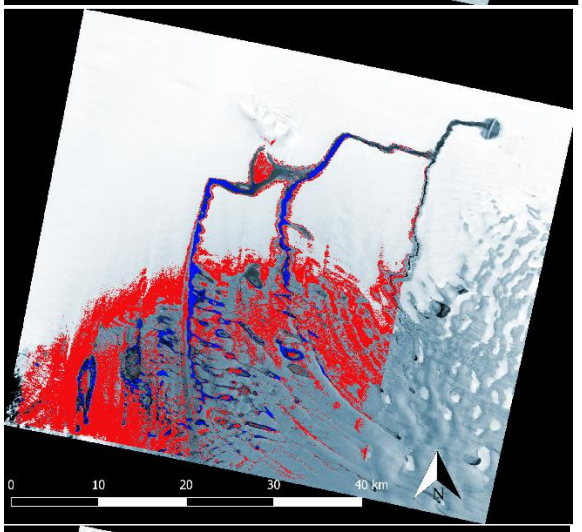
08/01/2018	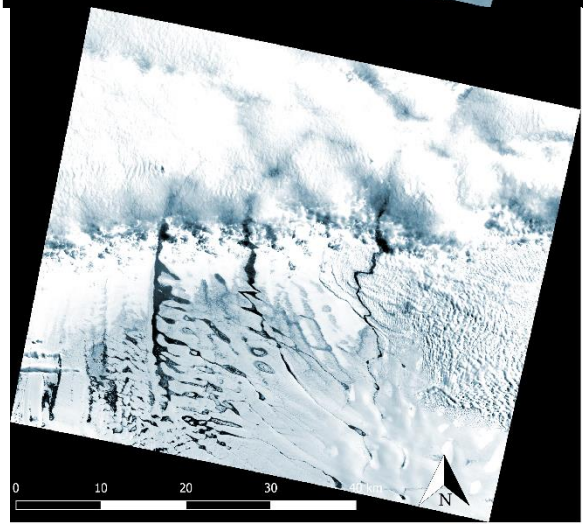	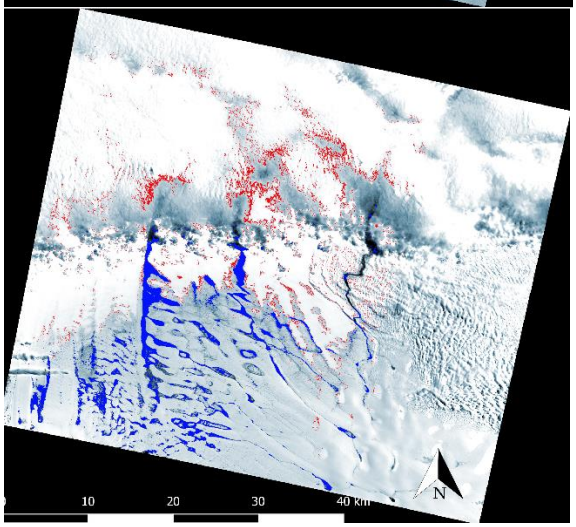

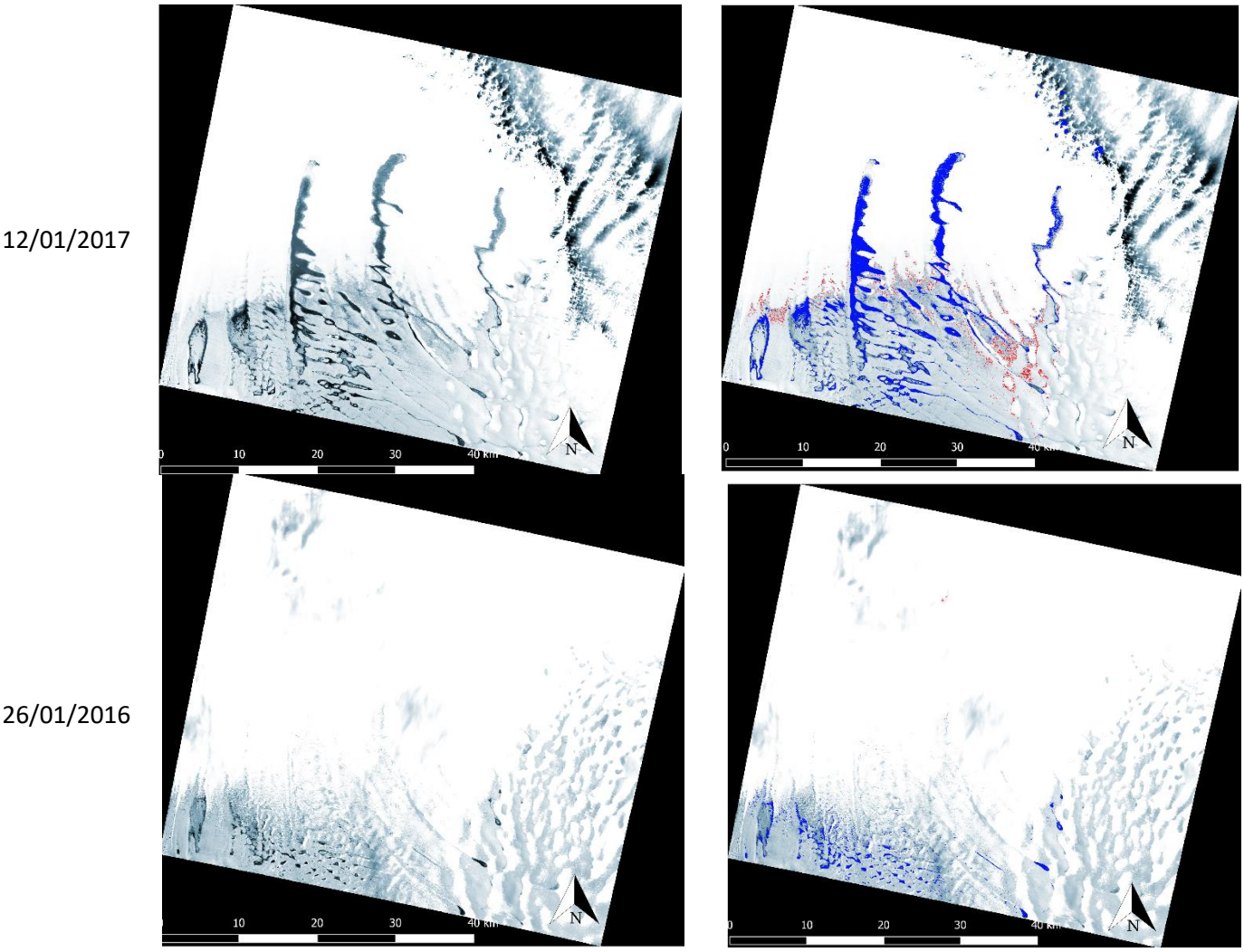

Figure 32. False colour RGB Landsat 8 images compared to lake (dark blue) and slush (red) masks determined using PCA-histogram method. Despite evidence of cloud in some images, the PCA remains successful at identifying supraglacial features.

5.1i Lake and Slush Extents

Lake and slush extent on NIS are sensitive to inter-annual variation in weather conditions (Figures 31-32). This corroborates the finding of Dell et al. (2020) that austral summers with highest air temperatures are those with the greatest lake and slush extents. Lake masks derived from Sentinel-2 and Landsat 8 images in the late austral summer identify two large elongate lake systems which hold up to 62.6 % of surface meltwater volume (Figure 31; Dell et al., 2020). The eastern and western systems are formed of a series of smaller lakes connected by supraglacial streams or slush patches and extend for ~16 and ~ 20 km respectively. Both lake systems terminate ~ 35 – 55km from the ice shelf front, most likely draining into the surrounding firn area. Under increased temperatures, the extent and volume of meltwater is likely to increase which may exceed the firn storage capacity, facilitating development of a drainage system which extends to the ice shelf front (Lenaerts et al., 2017).

Evidence of this is observed in the austral summer of 2020 where lake systems delivered sufficient water downstream to cause firn saturation nearer the terminus. The result is a 12 km^2 circular lake captured on 14/01/2020 (as seen in Figure 15 and Figure 32). The implications of an end-member state characterised by meltwater pooling, rather than efficient meltwater export, are significant for the future stability of NIS (Kingslake et al., 2017). As demonstrated on Nansen Ice Shelf, the potential to develop efficient water evacuation systems may mitigate ice shelf instability (Banwell, 2017; Frezzotti et al., 2017; Bell et al., 2018). The PCA-histogram method for lake delineation could therefore be incorporated into predictive models to estimate scenarios of ice shelf stability under different hydrological regimes.

At present, however, extensive firn cover on NIS facilitates the storage of meltwater in firn-pack pore space. The PCA method extracts slush coverage of up to 155 km^2, corroborating expectations of extensive water-saturated firn (Buzzard et al., 2018). Landsat 8 and Sentinel-2 images both indicate increased slush extent since the austral summer of 2017 (Table 12-13). Extensive slush coverage presumably suggests that current firn capacity is sufficient to delay the development of a supraglacial distribution similar to that observed on Larsen B prior to its collapse in March 2002 (Glasser and Scambos, 2008; Banwell and MacAyeal, 2015). Although current firn capacity for water storage reduces likelihood of hydrofracture through the ice shelf, efficient storage of interstitial water in firn adds extra load. Whilst this load may not be sufficient to generate flexure forces capable of initiating fracture propagation (Banwell et al., 2019), the overall stress field is altered with unresearched implications for cross-grounding line ice flow.

Whilst high firn capacity limits development of new lakes, existing lake systems form in the same locations year-on-year. Lake masks indicate that SGLs cluster around the grounding line in the early melt season and then gradually grow into larger water bodies which expand nearer the ice shelf front (Figures 31-32). As Dell et al. (2020) suggest, this is the result of lateral transfer of water across NIS through the austral summer. Firn facilitates lateral transport of water if it becomes isothermal or if it is saturated to the extent that it becomes an impermeable surface for excess meltwater to flow over (Kingslake et al., 2015). The distinction between unsaturated firn, with water storage capacity, and saturated firn, which facilitates lateral melt water transfer, is one not investigated in this study. However, the PCA-histogram method may be extended, using different thresholds, to categorise supraglacial features further into more discrete categories (e.g. different types of slush). Different forms of slush which transition from meltwater storage to meltwater transfer zones have varying implications for ice shelf hydrology.

For the most recent images, PCA-histogram thresholds applied to Landsat 8 out-perform Sentinel-2 masks in identifying both stagnant and flowing water bodies (Figure 32). This may be due to the greater weighting of the infrared bands in the Landsat 8 PCA which would lead to greater sensitivity of lake masks to NIR bands. In contrast to Sentinel-2 masks, the Landsat 8 masks delineate far smaller areas of slush which reduces the overall recorded agreement (62%) of the PCA delineation method applied with different satellite data (Section 4.2ii). Slush patches are calculated from Landsat 8 imagery to be within 0 – 300 m of SGLs and further away from the grounding line compared to Sentinel-2 slush masks (Figure 31-32). Whilst these differences are likely the result of the thresholds used, it indicates that slush delineation remains subject to more uncertainty that SGL regions, as confirmed by the confusion matrix results (Section 4.2ii). Therefore, applying the PCA-histogram method to satellite imagery from different sensors tests the reliability of results for different supraglacial features.

The PCA-histogram method developed here presents a number of improvments in accurate SGL delineation compared to ratio-band techniques. Previous NDWI-based classification methods under-estimate lake extent in the majority of cases, whilst large errors of commission are introduced in cloudy images (Williamson et al., 2017). Thin, low-altitude cloud has similar visible spectral characteristics to that of slush which has prevented delineation of slush extent in previous research using single and ratio band techniques (Pope et al., 2016; Watson et al., 2018). The PCA-histogram method is able to delineate lake and slush extent through cloud cover of up to 20% and without mis-identifying cloud (Figure 33). This demonstrates the utility of considering spectral returns across a broader range of wavelengths.

Furthermore, NDWI threshold is user-defined whereas the histogram thresholds across PC bands are automatically identified from the frequency distributions. NDWI-generated lake masks may be useful for individual images, but the lack of threshold consistency between images makes it difficult to automate a longer temporal record of lake extent. Overall, the PCA-histogram lake and slush masks are successful at delineating supraglacial characteristics when visually compared to underlying false-colour composite images (Figures 31-32).

The finding that the PCA-histogram method significantly outperforms the classic band ratio methods has implications for a broad spectrum of research. The automated PCA-histogram method could be incorporated into lake tracking algorithms, such as FASTISh (Dell et al., 2020), and applied within energy balance models for constraint of different supraglacial characteristics. There is also potential for application to other Antarctic ice shelves where cloud coverage commonly disrupts surface

spectral data accquisition. However, there remain various sources of error which should be considered and rectified before this method is applied more broadly.

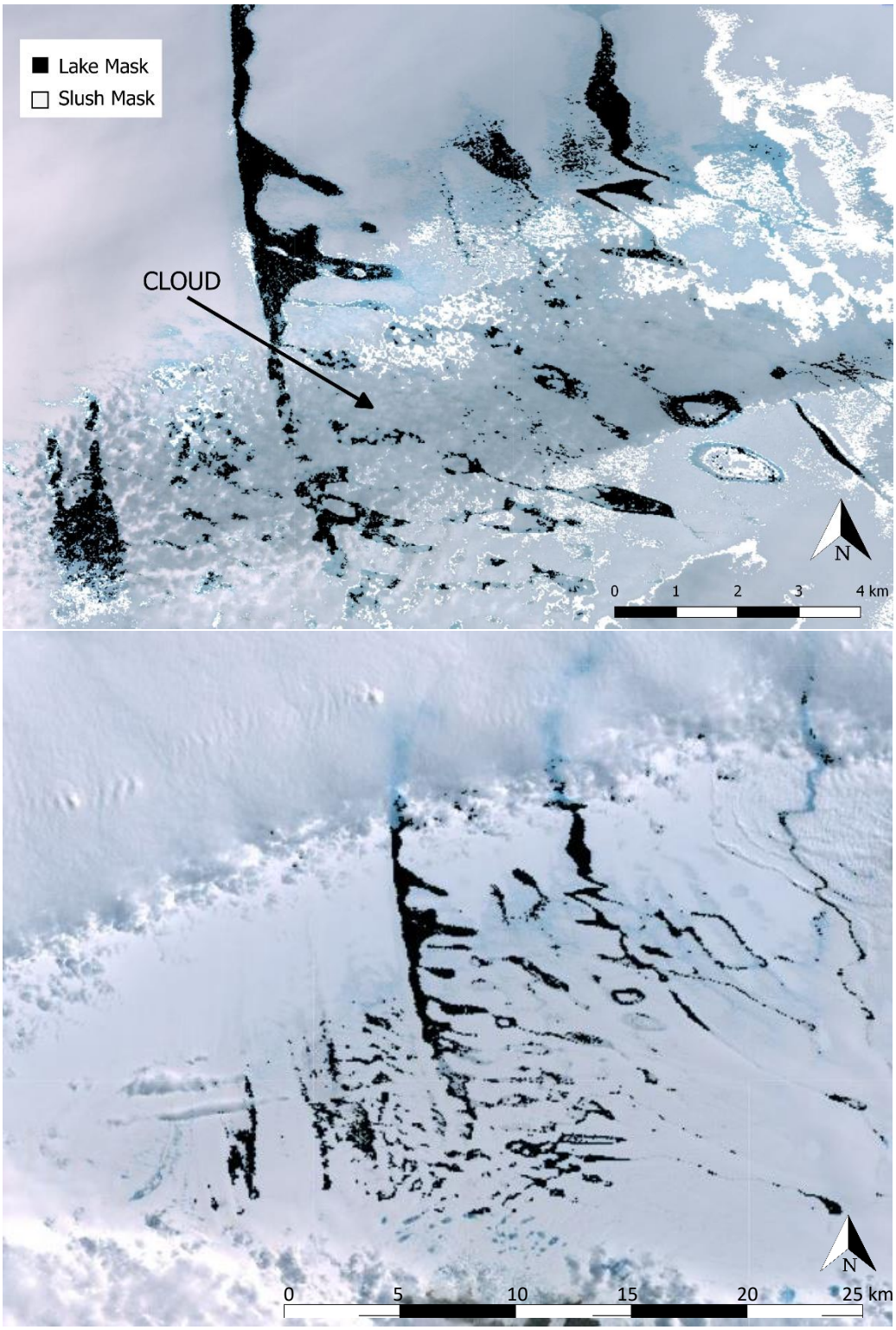

Figure 33. Lake (black) and slush (white) mask determined from PCA-histogram method on RGB background image for (a) 11/01/2018 Sentinel-2 image and (b) 08/01/2018 Landsat 8 image. Despite ~20% cloud cover, masks do not misidentify clouds and some lakes are detected through clouds.

5.1ii Limitations of PCA-Histogram Method

Sentinel-2 and Landsat 8 imagery are demonstrated to work successfully with the PCA-histogram method. The high spatial resolution of Sentinel-2 allows more accurate boundary delineation between SGL and slush areas. Errors related to application of Landsat 8 imagery are likely to arise as a result of lower spatial resolution (30 m) for each band layer. The SGL-slush boundary may occur within a 30 m pixel whilst spectral reflectance will be averaged over the 30 m^2 pixel generating error in the final classification of the pixel. The selection of relevant bands using the PCA aims to minimise inclusion of unnecessary thresholds which would otherwise exacerbate this source of error.

Uncertainty associated with the PCA-histogram method is smaller compared to previous single-band methods although some discrepancies between mapped and observed lakes remain. Visual inspection of the Sentinel-2 PCA-histogram lake mask against the false-colour images suggests that the thresholding underestimates water-covered pixels furthest from the grounding line (Figure 31). In these Sentinel-2 images, water-covered areas furthest from the grounding line are generally braided supraglacial streams rather than SGLs (Figure 31). Therefore, the inaccuracy of the PCA-histogram method in these regions could be related to the variable contribution of the infrared bands due to differing temperatures of stagnant versus flowing water. Uncertainty introduced across infrared bands could be minimised by subsequently filtering extracted water-covered areas by geometry (e.g. Yang and Smith, 2012).

The PCA-histogram method is accurate for supraglacial feature delineation using Landsat 8 imagery when the user can eliminate bands which are causing significant errors of omission. The disproportionate sensitivity of Landsat 8-derived slush extent to the blue band (B2) required user intervention to remove the blue band threshold. The limitation of this is that the method is no longer automated and subject to researcher bias. User intervention is also occasionally required to mask cloud shadow in Landsat 8 images. Whilst the SIMPLE_CLOUD_SCORE algorithm, provided in GEE, is applied to mask the cloud itself, the cloud shadow on images is not masked and may be misidentified as slush (Figure 32). Such errors are minimised using the PCA-histogram method, but uncertainty cannot be fully eliminated without high resolution ground truthing data. The greatest source of uncertainty is derived from the lack of ground truthing data to quantify the relative accuracy of different approaches. Application of the PCA-histogram method for areas with available *in situ* data would be a useful pursuit for future research.

5.2 Surface Energy Balance Model Discussion

Over the austral summers of 2017 to 2020, slush and lakes begin to form around mid-November, corresponding to the beginning of the austral summer, and reach peak extent by Feburary in all years. The modelled timing of lake formation corroborates austral summer timings determined by the annual SEB model of Jakobs et al. (2019). Interestingly, daily mean energy flux per lake and slush pixel peaks earlier in January (Figure 23). An initial peak in the mean energy absorbed at each pixel is followed by a peak in the extent of lake and slush areas. Whilst average energy absorption is directly sensitive to maximum intensity of incoming SW radiation in early January, there is an indirect lagged effect for slush and lake extent.

The peak in average lake energy absorption at each lake pixel may indicate a period of lake deepening. Further energy transfer to the ice shelf and melting facilitates the over-topping of the already saturated and deepened lake basin, generating subsequent increase in extent. This confirms the observation of Dell et al. (2020) that early austral SGL formation is controlled by air temperature and solar radiation, whilst late austral summer lake development is controlled by ice shelf topography. There is therefore a 'trade-off' between peak energy availability in early January and peak lake extent in late January, when total energy absorption capacity reaches a maximum. As the season progresses towards late January, input energy availability decreases limiting the energy absorption potential of deepened lakes. The lag between maximum input energy availability, maximum energy absorption and supraglacial feature extent provides insight into lake-firn interaction on NIS.

Processes, whether lake over-topping or firn saturation, involved in forming NIS supraglacial hydrology are inter-annually variable. Mean energy absorbed by lake and slush pixels remained proportionately similar in 2017 and yet total energy absorbed across the lake region was up to 9 times greater than that of slush (Figures 22-23). Such a large total absorption at lake pixels is related to extensive lake coverage. Meanwhile, in the austral summer of 2019, total energy absorbed across the entire slush region (~1 GJ/day) was as large as energy absorbed across the entire lake region (~1.6 GJ/day) (Figure 22). The ability of slush regions to absorb similar total energy to that of SGL areas during high slush years is of notable importance. Therefore, despite assumptions that SGLs are a predominant means by which extra energy is transferred to Antarctic ice shelves (Kingslake et al., 2017; Jakobs et al., 2019), highly-saturated slush zones are of underestimated significance in austral summers where slush is spatially extensive. However, in most austral summers studied, slush areas contribute a far smaller proportion of energy to NIS relative to SGLs. In general, slush areas efficiently re-emit energy absorbed at times of peak solar insolation giving daily near-zero net energy

contribution (Figure 22). Net positive total energy absorption of slush regions in the austral summer of 2019 indicates underestimated implications of slush in particular years. This supports development of research into the evolution of slush and controls on its inter-annually variable formation.

Water-saturated slush has implications for energy balance not only because of lower albedo but also because, on East Antarctic ice shelves, slush is typically a precursor for SGL formation (Buzzard et al., 2018). Widespread slush indicates increasingly favourable conditions for lake formation with implications for increasing inter-annual net energy absorption. However, given that only one high slush extent year (2019) is recorded between austral summers of 2017 - 2020, the temporal record is insufficient to determine any inter-annual trend of increasing frequency in high slush years.

The controls determining relative significance of SGL or slush areas for NIS energy balance are currently unknown. Meteorological variability across the austral summers of 2017 – 2020 is extracted from the GFS dataset and plotted to suggest controls on proportionally high lake and slush years (Figures 34-37). Given confirmed sensitivity of the model to shortwave radiation, specific humidity, wind speed and air temperature are considered here. Specific humidity varies minimally between 0.001 - 0.004 g/kg and is therefore unlikely to alter overall energy flux significantly enough to explain inter-annual variability. Figures 38-41 show little evidence of co-variability between total SEB with either air temperature or wind speed. Regression of the GFS meteorological data with net SEB gives the strongest correlation between net lake SEB and air temperature ($R^2 = 0.1848$), although this correlation is insignificant at the 5% level (Figures 38-41). Overall, the lack of significant trends in inter-annual meteorological variability suggests that other controls are likely to be more important in explaining the high lake year of 2017 and high slush year of 2019.

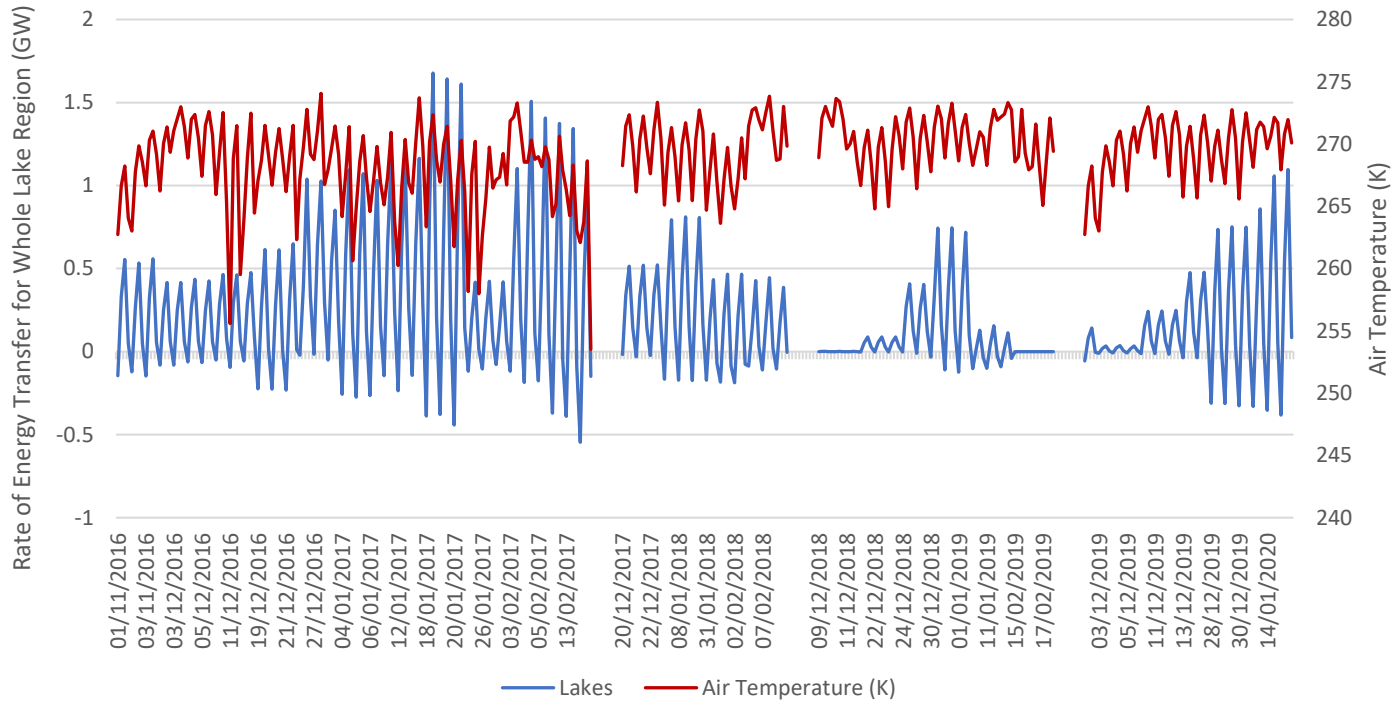

Figure 34. Rate of energy transfer over whole NIS lake region (2016-2020) and air temperature (K). Air temperature from GFS Data. Rate of energy transfer and GFS data collected at 6-hourly time stamps at 00:00, 06:00, 12:00 and 18:00.

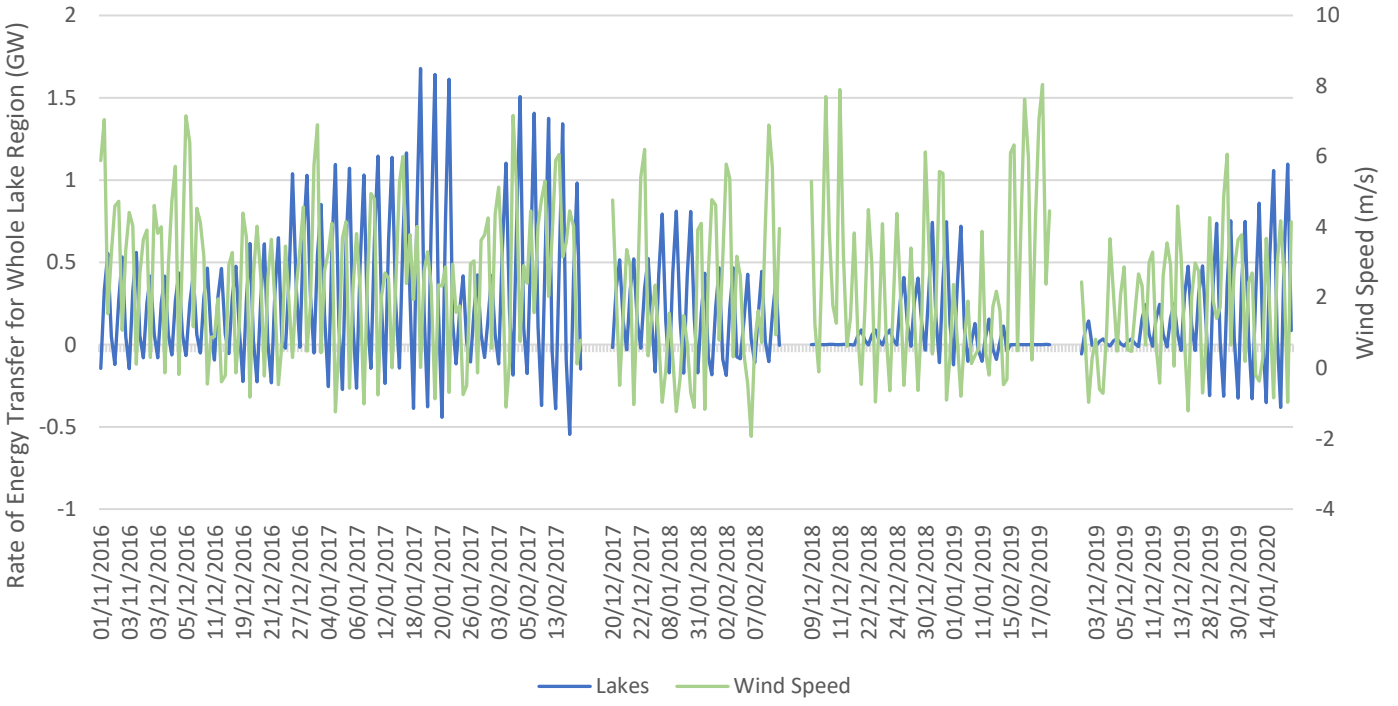

Figure 35. Rate of energy transfer (GW) over whole NIS lake region (2016-2020) and wind velocity (m/s) in the north-south direction. Wind velocity from GFS data taken in north-south orientation given assumption that katabatic winds flowing off the ice sheet dominate relative to east-west winds. Rate of energy transfer and GFS data collected at 6-hourly time stamps at 00:00, 06:00, 12:00 and 18:00.

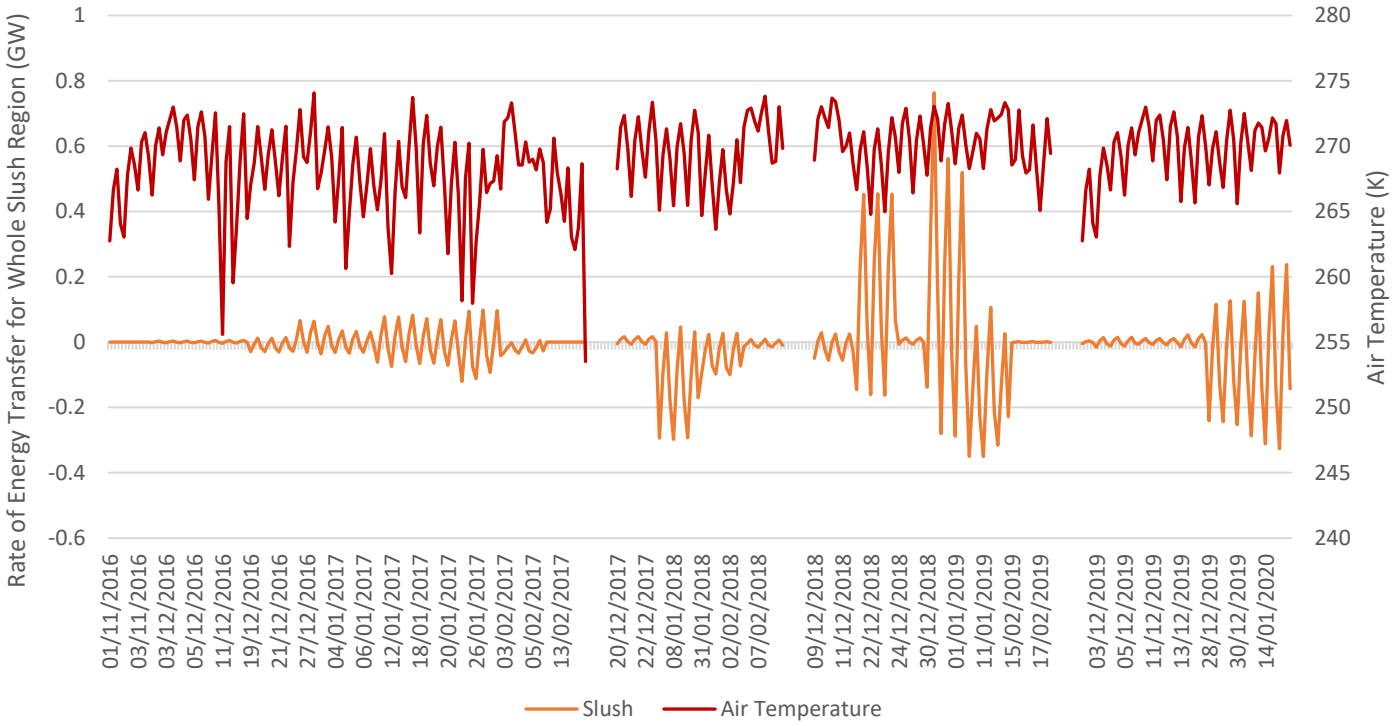

Figure 36. Rate of energy transfer (GW) over whole NIS slush region (2016-2020) and air temperature (K). Air temperature from GFS data. Rate of energy transfer and GFS data collected at 6-hourly time stamps at 00:00, 06:00, 12:00 and 18:00.

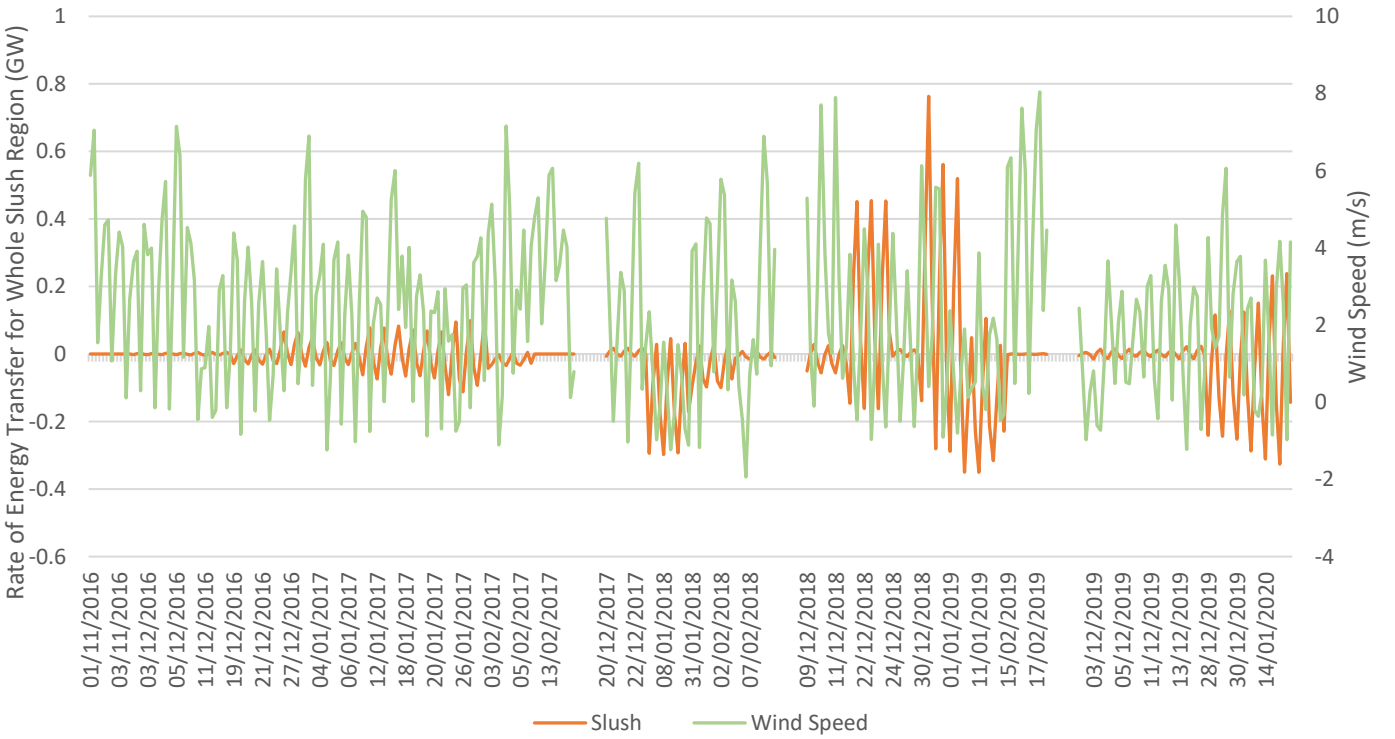

Figure 37. Rate of energy transfer (GW) over whole NIS slush region (2016-2020) and wind velocity (m/s) in the north-south direction. Wind velocity from GFS data taken in north-south orientation given assumption that katabatic winds flowing off the ice sheet dominate relative to east-west winds. Rate of energy transfer and GFS data collected at 6-hourly time stamps at 00:00, 06:00, 12:00 and 18:00.

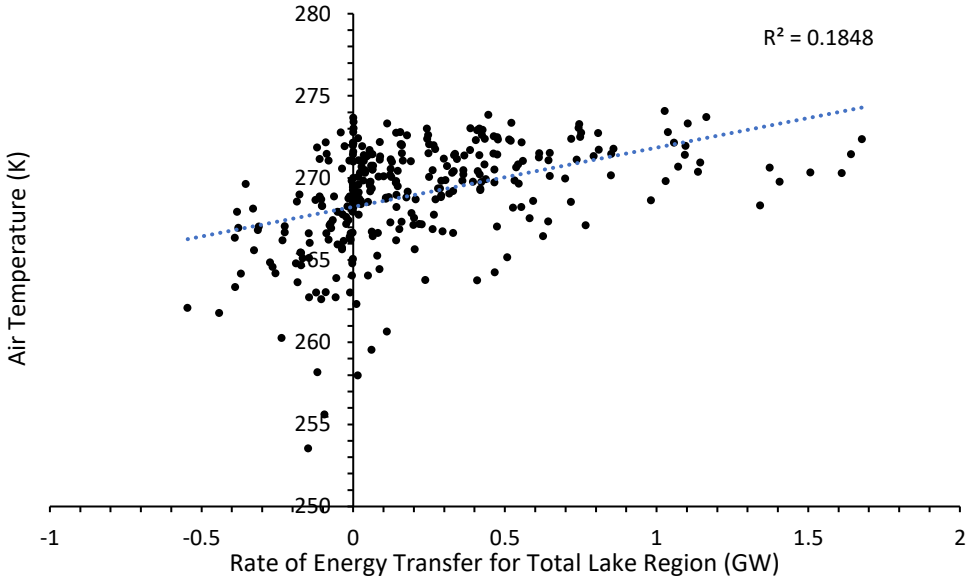

Figure 38. Relationship between rate of energy transfer (GW) over whole lake region (2016-2020) and air temperature (K). Weak positive correlation but significant at the 5% level. Linear regression test run in SPSS.

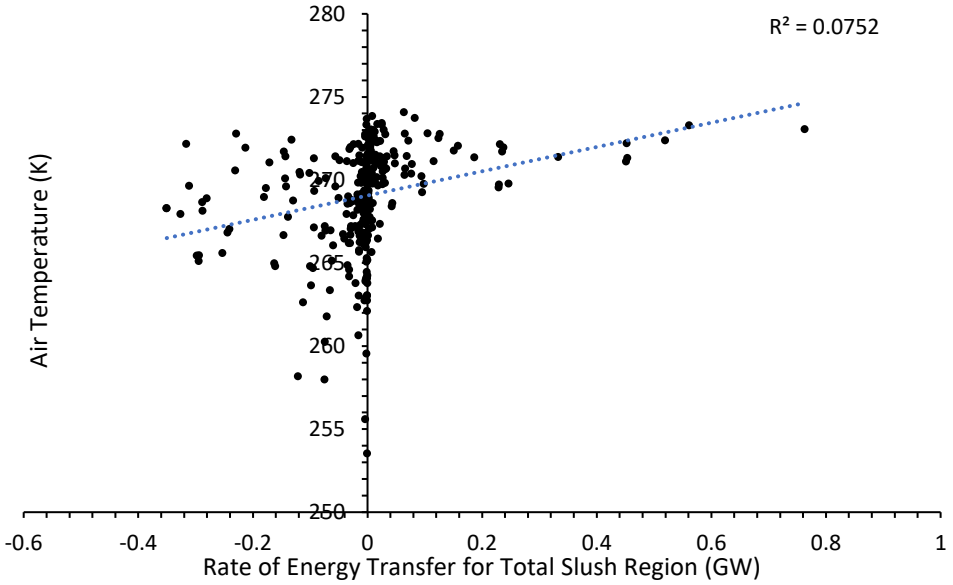

Figure 39. Relationship between rate of energy transfer (GW) over whole slush region (2016-2020) and air temperature (K). Weak positive correlation and insignificant at the 5% level. Linear regression test run in SPSS.

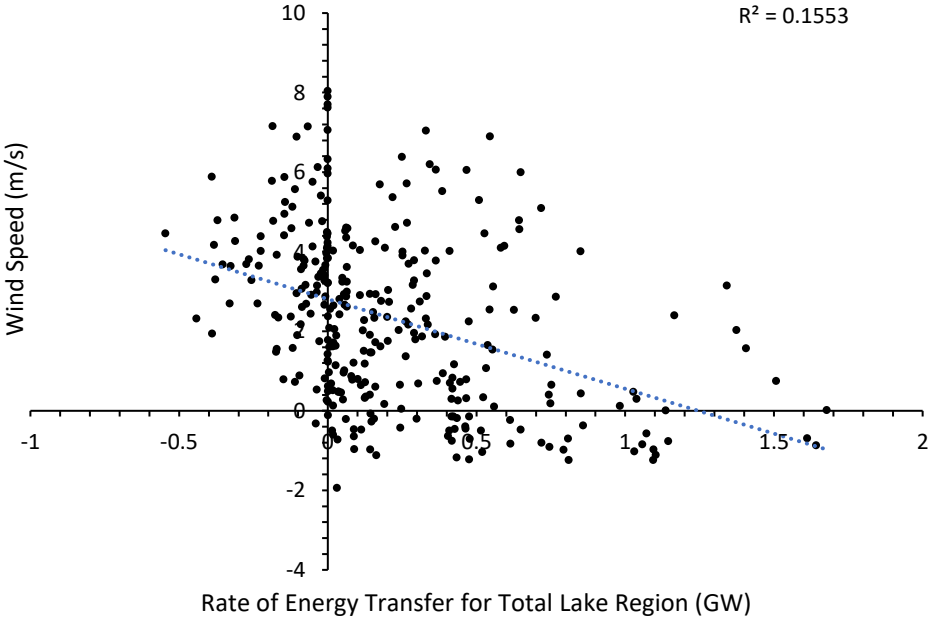

Figure 40. Relationship between rate of energy transfer (GW) over whole lake region (2016-2020) and wind speed (m/s). Weak positive correlation but significant at the 5% level. Linear regression test run in SPSS.

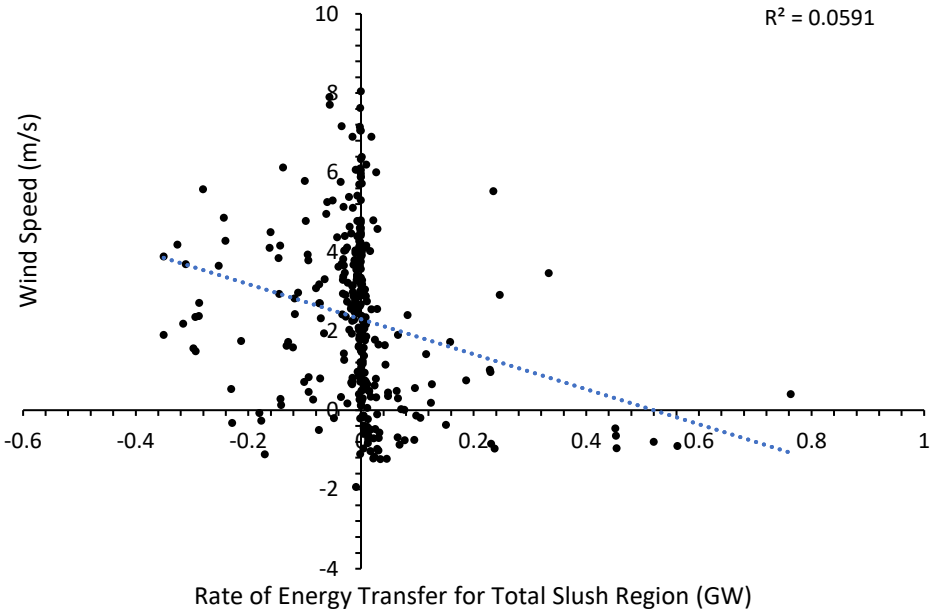

Figure 41. Relationship between rate of energy transfer (GW) over whole slush region (2016-2020) and wind speed (m/s). Weak positive correlation and insignificant at the 5% level. Linear regression test run in SPSS.

Modelled mean energy absorption for lake pixels is constant over the years 2017 – 2020 at each time of day (Figure 20). Deeper lakes are expected to be more efficient at attenuating incoming shortwave radiation and therefore will absorb greater proportions of incident radiation (Sneed and Hamilton, 2007; Banwell et al., 2012). The lack of change in mean energy absorption at lake pixels suggests that there has been no significant inter-annual lake deepening. Slight increases in average absorption at slush pixels at each time of day may suggest increasing water saturation between 2017 – 2020 (Figure 20). However, given the relatively short time period over which the model results are evaluated and the lack of *in situ* data, this hypothesis cannot be reliably confirmed. Inter-annual mean energy absorption is relatively unchanged but daily SEB flux variation results indicate localised trends in energy transfer. Therefore, the following section outlines the significance of temporal and spatial variability of each of the different energy fluxes.

The daily variability of SEB flux is controlled primarily by incident shortwave radiation confirming the conclusions of Jakobs et al. (2019) and Buzzard et al. (2018) that SEB models are most sensitive to absorbed shortwave radiation. Whilst incoming shortwave radiation reaches a peak between 1200 and 1800, it is notable that net SEB for SGLs and slush is lower on average at 1800 than at 0600 (Figure 20). Lower net energy transfer to NIS in the afternoon, despite incident shortwave radiation remaining high, is likely the result of increasing longwave radiation emission towards the end of the day. This is expected as the ice shelf surface re-radiates energy that has been absorbed throughout the day (Benn and Evans, 2014). Greater emission of longwave radiation in the afternoon counter-acts a proportion of incoming shortwave radiation, causing net energy transfer to decrease in the

afternoon. At a typical lake and slush area on the Nivlisen Ice Shelf, peak energy absorption occurs between 0600 and 1200.

Consistently net negative longwave radiation flux for SGL and slush regions implies greater longwave radiation emission than absorption. Due to lack of direct or forecasted measurements, the Stefan-Boltzmann law uses temperature as a proxy for incident and emitted longwave radiation. Air temperature at 2 m (proxy for incoming longwave) is ~4 K colder than lake and slush surfaces (proxy for outgoing longwave) which explains negative longwave radiation budget. SGLs and slush regions absorb incoming shortwave radiation and efficiently re-emit longwave radiation (Benn and Evans, 2014). However, daily longwave emitted radiation is on average two orders of magnitude smaller than absorbed shortwave radiation across austral summers (Figures 24, 25, 27, 28). As suggested by Law et al. (2020), the sensitivity of the model to incoming shortwave radiation relative to other fluxes should place greater emphasis on accurate measurement of solar radiation.

Although shortwave energy fluxes dominate overall energy balance, the relative spatial variability of other fluxes give insight into the interaction of NIS with its atmospheric and topographic setting. Variable contribution of net latent and sensible heat at lake and slush areas to the overall SEB of NIS implies the significance of local ice shelf processes. Controlling variables may include distance from the grounding line, elevation, wind strength and turbulence, proximity to nunataks and variable strain fields (Stokes et al., 2019).

The sensible and latent heat contribution of slush over NIS is relatively unchanged in each SEB calculation whilst lake pixels respond sensitively to spatial and temporal meteorological variation. The stability of overlying air column, parameterised in the SEB model by the Richardson number, is a control on SGL sensible and latent heat fluxes. An unstable and turbulent air column allows for substantially more sensible and latent heat to be transported away from the surface (Cohen and Rind, 1990). Lakes at higher elevations near the grounding line emit low amounts of sensible heat and are net absorbers of latent heat due to freezing (Section 4.3). There is a distinct spatial transition from a stable to turbulent air column moving from the grounding line towards the terminus of the ice shelf (Figure 42). This localised transition in near-surface atmospheric stability can be explained in the context of the topographic setting of NIS.

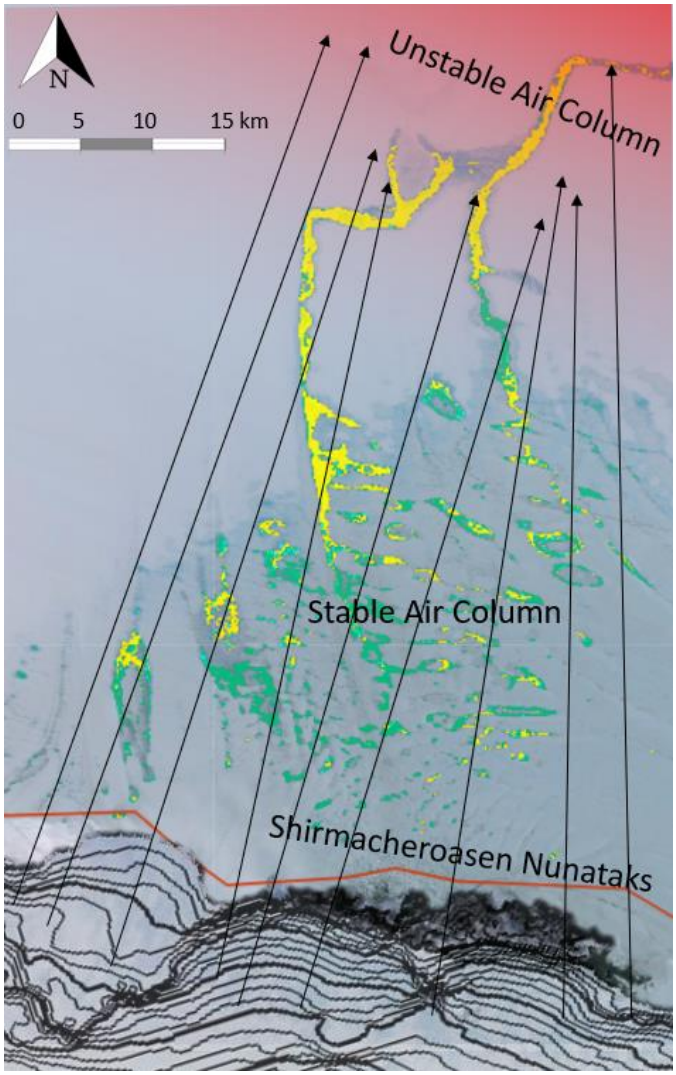

Figure 42. Spatial differentiation of lake pixels with negative Richardson numbers (yellow) and positive Richardson numbers (green) which indicate unstable (red hue) and stable (blue hue) air columns respectively. Wind (black arrows) is forced over nunataks generating stable air in the lee of the topography, nearest the grounding line (red line). RGB Sentinel-2 image from 31/01/2019. 10 m contours from REMA data cropped for grounded ice area.

Tributary glaciers feed the NIS over an arc of steep topography - the Shirmacheroasen nunataks - before the NIS becomes ungrounded (Lindbäck et al., 2019). Elevation profiles from grounded ice 20 km inland to the floating NIS demonstrate elevation changes of over 700 m (Figure 42). SGLs closer to the grounding line are in the lee of the Shirmacheroasen nunataks, sheltered from the strong northerly katabatic winds flowing off the EAIS. Meanwhile, SGLs closer to the ice shelf front are exposed to these strong winds facilitating high evaporation rates and maintaining the surface-atmosphere temperature gradient (Figure 42). Although localised wind variability is the most likely interpretation for the contribution of SGLs to sensible and latent heat flux, the lack of *in situ* data available prevents construction of an accurate wind profile with height over Nivlisen.

The effect of katabatic winds on energy fluxes implied in this study is supported by previous research. Katabatic winds interact with the ice shelf surface and facilitate enhanced ablation by: i) removing surface snow and exposing lower albedo blue ice; and ii) enhancing near-surface temperatures by up to 3 K (Lenaerts et al., 2017; Moussavi et al., 2020). The turbulent air column above lakes ~5-10 km from the grounding line is indicative of the influence of strong katabatic winds creating conditions favourable to SGL formation. Meanwhile, the stability of the air column over lakes ~0-5 km from the grounding line, in the lee of the Shirmacheroasen nunataks, slows the development of SGLs. This indicates that the relationship between katabatic winds, topography, and meltwater production is more nuanced than a simple distance decay model based on proximity to low albedo features (Kingslake et al., 2017). Whilst research has previously focused on the significance of nunataks for longwave radiation budget, these results indicate significance of nunataks for localised wind disturbances and, hence, sensible and latent heat fluxes. Further research would be useful to better constrain the variability of nunatak-ice shelf interactions given the positive feedback mechanism between overall thinning of AIS and increased nunatak exposure (Kingslake et al., 2017).

Attributing the spatial variability of SGL sensible and latent heat fluxes to wind patterns also explains the proportionally invariable fluxes from slush regions. Previous research suggests that winds only effect the temperature profile of slush, and therefore sensible heat flux, up to depths of a few centimetres (Cohen and Rind, 1991; Brandt and Warren, 1997). Brandt and Warren (1997) measured temperature changes through 3 m of snowpack at the South Pole Station and found that temperature variability was reduced by an order of magnitude at just 20 cm of depth relative to the surface. Meanwhile, at SGLs, a wind-generated surface disturbance is effective at driving water circulation. This mixing may bring cooler water at depth to the surface, steepening the atmosphere-SGL temperature gradient and enhancing energy transfer. Therefore, the effect of katabatic winds on sensible and latent heat fluxes is more substantial over lakes than for slush by this heat-exchange mechanism.

5.2i Surface Energy Balance Model Validation

Lake volume, used as a proxy for energy absorbed by Nivlisen Ice Shelf's surface, is determined using a depth-calculation method proven to reliably reproduce field measurements (Sneed and Hamilton, 2007; Banwell et al., 2014; Pope et al., 2016). The correlation coefficient (R^2 = 0.2588) between modelled cumulative energy and inferred energy absorption, derived from peak lake volume, indicates a positive linear relationship. However, the agreement between modelled and inferred

datasets is not statistically significant ($p > 0.01$), suggesting sources of error in this validation method. This is likely related to the assumption that modelled energy remains constant between days with available spectral data i.e. there is no variability in lake area between satellite images captured. Recent work challenges this assumption by suggesting that short lived (<1 week) intense (> 4 mm w.e./day) melt events are the main control on seasonal evolution of lake area (Arthur et al., 2020). Implications of intense melt events and lateral meltwater transport on East Antarctic ice shelves must be better constrained for validation of SEB models.

Modelled energy balance predicts that, on average, ~1.5 times more energy is absorbed at lake pixels than is inferred by calculated lake volume. The marginal overestimation of modelled to inferred energy absorption from lake volume indicates SEB model accuracy, as water volume calculated in the images is an instantaneous snapshot of water stored, and so cannot account for volume loss via leakage. SGL volume is variable on sub-hourly timescales by lateral transport, vertical infiltration or even evaporation (Arthur et al., 2020). Therefore, a degree of systematic error is introduced using this method of model validation.

Given extensive firn cover on Antarctic ice shelves (Lightenberg et al., 2011), the assumed SGL base is unlikely to be a distinct boundary between liquid water and impermeable ice. Meltwater retention in firn is important as firn must be impermeable or fully saturated for SGLs to form (Buzzard et al., 2018). The phase boundary between the saturated firn layer and lake bottom is difficult to determine remotely without ground truthing data. Given that saturated slush areas beneath SGLs on NIS also contain liquid water, the total lake volume quantified is subject to uncertainty from assumed depth of phase boundary and underlying slush water-retention capacity (Buzzard et al., 2018). The recent release of ICESat-2 data shows potential for more accurately delineating subsurface boundaries on Antarctic ice shelves. Even if the SGL base could be better constrained using ICESat-2 data, water storage capacity in underlying firn would still generate a degree of error in lake volume estimation.

Using SGL volume to validate the SEB model assumes that energy input from external sources, other than incident radiation, is negligible. This is a reasonable assumption to make given that energy transfers from precipitation, ocean heat transfer and geothermal sources are small for floating ice shelves, such as NIS (Wei et al., 2014; Lindbäck et al., 2019). Precipitation rates measured at the Novolazarevskaya Weather Station are low (19 mm w.e./month), altering sensible heat transfers negligibly. Heat flux from the base of the ice shelf derived from underlying ocean is not considered a significant source of energy for the melting of surface ice (Buzzard et al., 2018; Akhoudas et al., 2020). However, warming of the Weddell Sea over recent decades (Schmidtko et al., 2014) has

generated up to 7 m/yr of basal melt (Lindbäck et al., 2019). Therefore, as the ice shelf thins and ocean temperatures increase, ice shelf temperature profile may steepen to alter surface energy fluxes significantly. At present, no temperature profile through a floating ice shelf in East Antarctica is available, limiting understanding of ocean-ice shelf thermal energy exchanges (Holland et al., 2008; Dinniman et al., 2016). This defines a key area for future *in situ* research and numerical modelling.

Whilst external sources of extra energy are currently considered negligible, assumptions made about internal transfers of energy introduce uncertainty in the conversion from lake volume to inferred energy absorption. Energy transferred from solar radiation is not used solely to generate melt which forms lake volume. Radiative energy is likely to be transferred to kinetic energy within the water column which in turn generates energy losses to surrounding slush through friction. Some of the energy transferred to generate the volume of melt observed on NIS is also lost to other internal processes which are unaccounted for in this empirical conversion. This also clarifies why the inferred energy transfer is under-estimated relative to modelled energy transfer. Sources of uncertainty remain in this validation method and the following section outlines limitations in the SEB model developed.

5.2ii Surface Energy Balance Model Limitations

The SEB model performs well in quantifying extra energy absorbed by lake and slush areas on NIS for Landsat 8 and Sentinel-2 images. Whilst input meteorological data is abundantly available through complex forecast modelling and reanalysis, satellite image acquisition is limited by revisit interval and cloud conditions. The lack of consistency in image availability between years (2016 – 2017 has 13 images, 2019 – 2020 has 6 images) has implications for the interpretation of inter-annual trends. For example, total energy absorbed at SGLs is significantly higher in 2016-2017 which is assumed to be a result of greater SGL extent but may be a product of the images that were available. The consistency of supraglacial feature positioning in images across each austral summer suggests that it is unlikely that the results are skewed by available images. However, the uncertainty derived from lack of input data should be noted.

As stated, meteorological input data is readily available at high temporal intervals in the GFS data used here. However, GFS data does not include a forecast for longwave radiation. Longwave energy flux is calculated using the Stefan-Boltzmann law and the difference between surface and air temperature at 2 m (Wang and Dickinson, 2013). Downward longwave radiation at the surface is affected by vertical concentration distributions of water vapour, carbon dioxide and other trace

gases which cannot be accounted for using an empirical conversion (Morcrette and Fouquart, 1985; Palchetti et al., 2008). Surface temperature is derived using Planck's irradiance function for TOA reflectance data in the SWIR bands, corrected by calibration coefficients (Chander et al., 2009). The decoupling of TOA and surface radiation fields mean that infrared band-based estimates of downward longwave radiation contain large errors, particularly under cloudy conditions (Liang et al., 2001; Talley et al., 2011). Once net longwave radiation is ingested into reanalysis datasets, such as ERA-5, this source of error in the SEB model would be reduced.

The model developed here quantifies energy exchanges occurring in an infinitesimally thin surface layer. The results are therefore useful for quantifying the implications of the interactions between supraglacial features and the near-surface atmosphere. However, the energy which is eventually transferred to the underlying ice shelf propagates through a water column or interstitial slush pack. Recently developed models, such as GlacierLake (Law et al., 2020), numerically derive these surface processes of energy transfer at depth. The subsequent feedback effects of energy transfer processes at depth on surface energy fluxes is not quantified in this study, presenting a degree of uncertainty in SEB calculations.

5.3 Summary of Discussion

The discussion above highlights proportionately high lake extent in 2017 and extensive slush in 2019. Inter-annual variability of supraglacial feature extents and lagged timing of peak mean energy absorption and maximum lake extent are indicative of firn-meltwater interactions. In the austral summer of 2020, substantial meltwater accumulation nearer the ice shelf front suggests increasing firn saturation. If this meltwater persists and remains *in situ*, NIS will become increasingly vulnerable to hydrofracture-driven collapse. Conversely, if SGL systems over-top and facilitate lateral export of water, the ice shelf could be stabilised. The PCA-histogram method has further potential for delineating different slush types which would facilitate more accurate modelling of the evolution of ice shelf hydrology.

The SEB results for previous austral summers are dominated by shortwave radiation flux during peak daylight hours whilst the warmed slush and SGLs emit longwave radiation at times of low solar irradiance. Spatial variation in sensible and latent heat fluxes is determined by local topographic and atmospheric interactions. Whilst these fluxes vary by smaller magnitudes, this confirms that the SEB model can account for broader ice shelf processes.

6. Conclusions

Examination of supraglacial hydrology of ice shelves is important for understanding regional ice sheet mass balance, dynamics, and local energy transfer through the ice shelf (Jakobs et al., 2019; Leeson et al., 2020). Examples from the West Antarctic (Wilkins – Scambos et al., 2009) and the Antarctic Peninsula (Larsen B – Berthier et al., 2012) demonstrate potential for the evolution of surface meltwater distribution to enhance vulnerability to collapse and ongoing mass loss (Joughin et al., 2011; Rignot et al., 2013; Alley et al., 2019). It is important for ice mass loss and sea level rise projections to accurately constrain interactions between the atmosphere and ice shelf supraglacial hydrology for integration into more complex two-dimensional models of energy propagation at depth. This study makes a first attempt to quantify the extra energy transferred from the atmosphere to an Antarctic ice shelf (Nivlisen Ice Shelf) as a result of the presence of supraglacial lakes and water-saturated slush features.

The generation of an accurate surface energy balance model for NIS requires differentiation between distinct supraglacial features. Here, the PCA identifies clusters within the spectral reflectance variability of the surface of NIS which are interpreted as SGLs, slush, or clean ice regions. Thresholds from histograms of PCA-selected spectral bands differentiate these supraglacial features and constrain the spatial input domain for the SEB model. Given that the PCA-histogram method is successful for delineation of lake and slush features on East Antarctica, future research could test the accuracy of this method for other case study sites.

Following the equations set out by Buzzard et al. (2018) and Law et al. (2020), the SEB model developed here calculates mean daily energy absorbed at lake and slush areas as ~ 8.7 MJ/m^2/day and ~ 0.54 MJ/m^2/day across the austral summers of 2017-2020. Extra energy transferred at lake and slush regions is most sensitive to variability in incident shortwave radiation. As a proportion of net energy balance, sensible and latent heat fluxes are responsible for energy flux variability two orders of magnitude smaller than shortwave and longwave fluxes which corroborates estimations from other literature (Jakobs et al., 2019; Law et al., 2020). Although calculated lake volume, used for model validation, infers a net energy transfer which varies linearly with modelled energy absorption, the inferred energy transfer consistently underestimates extra energy absorbed by lakes. The volume of water stored in saturated firn beneath lake basins could represent a significant proportion of energy transferred to NIS which is unaccounted for in this method of empirical model validation.

A key finding from the SEB model is the significance of saturated slush for energy transfer in austral summers where slush is an extensive supraglacial feature. Total extra energy absorbed across the slush region in the year 2019 is equivalent to extra energy absorbed by SGLs, suggesting that slush can be a significant control on energy absorption. In the austral summer of 2019, total extra energy transferred to NIS is similar to extra energy transferred in the summer of 2017 – a year with widespread lake coverage. Therefore, a significant finding of this study is that exclusion of slush regions in previous energy balance calculations is likely to have underestimated the net energy transfer to Antarctic ice shelves in particular years. However, extensive slush cover is only recorded in 2019 limiting inter-annual comparison of controls on high lake versus slush extent.

The generation and firn-pack infiltration of meltwater to form slush, and subsequently SGLs, on Nivlisen Ice Shelf is found to have significant implications for transfer of energy. As Jakobs et al. (2019) suggest, the feedback between extensive surface meltwater coverage and enhanced absorption of incident radiation has implications for the sensitivity of East Antarctic ice shelves to future increases in radiative forcing and average temperatures. Furthermore, increased prevalence of surface meltwater will add extra loading to NIS with unknown implications for ice shelf stability. With the findings from this study, quantifying the relative contribution of lake and slush pixels, projections of future meltwater prevalence and East Antarctic ice shelf vulnerability to collapse can be more finely tuned. Accurate quantification of the SGL and slush energy balance given here is the starting point for predicting meltwater evolution under different radiative forcing pathways and reducing uncertainty in sea level projections.

7. Bibliography

Satellite Imagery:

Landsat 8, Operational Land Imager. Collection 1 Tier 2 TOA Reflectance. United States Geographical Society. Accessed using collection code: COPERNICUS/S2

Sentinel 2, Multi-Spectral Instrument. Level-1C data products. European Union, European Space Agency, Copernicus. Accessed using collection code: : LANDSAT/LC08/C01/T2_TOA

References:

AARI (2017) Information on monthly meteorology from NAWS were obtained from the Russian Federation NADC, Arctic and Antarctic Research Institute (AARI), http://www.aari.aq. Accessed January – February 2020.

Akhoudas, C., Sallée, J.B., Reverdin, G., Aloisi, G., Benetti, M., Vignes, L. and Gelado, M., 2020. Ice shelf basal melt and influence on dense water outflow in the Southern Weddell Sea. *Journal of Geophysical Research: Oceans*.

Alley, K.E., Scambos, T.A., Miller, J.Z., Long, D.G. and MacFerrin, M., 2018. Quantifying vulnerability of Antarctic ice shelves to hydrofracture using microwave scattering properties. *Remote Sensing of Environment*, *210*, pp.297-306.

Arst, H., Erm, A., Reinart, A., Sipelgas, L. and Herlevi, A., 2002. Calculating irradiance penetration into water bodies from the measured beam attenuation coefficient, II: application of the improved model to different types of lakes. *Hydrology Research*, *33*(2-3), pp.227-240.

Arthur, J., Stokes, C.R., Jamieson, S.S., Carr, J.R. and Leeson, A., 2020. Progress in understanding Antarctic supraglacial lakes using remote sensing. *Progress in Physical Geography.*

Banwell, A.F. and Macayeal, D.R., 2015. Ice-shelf fracture due to viscoelastic flexure stress induced by fill/drain cycles of supraglacial lakes. *Antarctic Science*, *27*(6), pp.587-597.

Banwell, A.F., Caballero, M., Arnold, N.S., Glasser, N.F., Mac Cathles, L. and MacAYEAL, D.R., 2014. Supraglacial lakes on the Larsen B ice shelf, Antarctica, and at Paakitsoq, West Greenland: a comparative study. *Annals of Glaciology*, *55*(66), pp.1-8.

Banwell, A.F., Willis, I.C., Macdonald, G.J., Goodsell, B. and MacAyeal, D.R., 2019. Direct measurements of ice-shelf flexure caused by surface meltwater ponding and drainage. *Nature communications*, *10*(1), pp.1-10.

Baťka, J., 2016. Factors of formation and development of supraglacial lakes and their quantification: A review. *AUC Geographica*, *51*(2), pp.205-216.

Bell, R.E., Banwell, A.F., Trusel, L.D. and Kingslake, J., 2018. Antarctic surface hydrology and impacts on ice-sheet mass balance. *Nature Climate Change*, *8*(12), pp.1044-1052.

Benn, D.I., Bolch, T., Hands, K., Gulley, J., Luckman, A., Nicholson, L.I., Quincey, D., Thompson, S., Toumi, R. and Wiseman, S., 2012. Response of debris-covered glaciers in the Mount Everest region to recent warming, and implications for outburst flood hazards. *Earth-Science Reviews*, *114*(1-2), pp.156-174.

Benn, D. and Evans, D.J., 2014. *Glaciers and glaciation.* Routledge.

Berthier, E., Scambos, T.A. and Shuman, C.A., 2012. Mass loss of Larsen B tributary glaciers (Antarctic Peninsula) unabated since 2002. *Geophysical Research Letters*, *39*(13).

Borstad, C. P., Rignot, E., Mouginot, J., and Schodlok, M. P.: Creep deformation and buttressing capacity of damaged ice shelves: theory and application to Larsen C ice shelf, The Cryosphere, 7, 1931–1947, https://doi.org/10.5194/tc-7-1931-2013, 2013.

Box, J.E. and Ski, K., 2007. Remote sounding of Greenland supraglacial melt lakes: implications for subglacial hydraulics. *Journal of glaciology*, *53*(181), pp.257-265.

Brandt, R.E. and Warren, S.G., 1997. Temperature measurements and heat transfer in near-surface snow at the South Pole. *Journal of Glaciology*, *43*(144), pp.339-351.

Burton-Johnson, A., Black, M., Fretwell, P. and Kaluza-Gilbert, J., 2016. An automated methodology for differentiating rock from snow, clouds and sea in Antarctica from Landsat 8 imagery: a new rock outcrop map and area estimation for the entire Antarctic continent. *The Cryosphere*, *10*, pp.1665-1677.

Busetto, M., Lanconelli, C., Mazzola, M., Lupi, A., Petkov, B., Vitale, V., Tomasi, C., Grigioni, P. and Pellegrini, A., 2013. Parameterization of clear sky effective emissivity under surface-based temperature inversion at Dome C and South Pole, Antarctica. *Antarctic Science*, *25*(5), pp.697-710.

Buzzard, S.C., Feltham, D.L. and Flocco, D., 2018. A mathematical model of melt lake development on an ice shelf. *Journal of Advances in Modeling Earth Systems*, 10(2), pp.262-283.

Chai, T. and Draxler, R.R., 2014. Root mean square error (RMSE) or mean absolute error (MAE)?–Arguments against avoiding RMSE in the literature. *Geoscientific model development*, 7(3), pp.1247-1250.

Chand, M.B. and Watanabe, T., 2019. Development of Supraglacial Ponds in the Everest Region, Nepal, between 1989 and 2018. *Remote Sensing*, *11*(9), p.1058.

Chander, G., Markham, B.L. and Helder, D.L., 2009. Summary of current radiometric calibration coefficients for Landsat MSS, TM, ETM+, and EO-1 ALI sensors. *Remote sensing of environment*, *113*(5), pp.893-903.

Colbeck, S.C., 1979. Water flow through heterogeneous snow. *Cold Regions Science and Technology*, *1*(1), pp.37-45.

Coléou, C. and Lesaffre, B., 1998. Irreducible water saturation in snow: experimental results in a cold laboratory. Annals of glaciology, 26, pp.64-68.

D'Urso, G. and Calera Belmonte, A., 2006, August. Operative approaches to determine crop water requirements from Earth Observation data: methodologies and applications. In *AIP conference proceedings* (Vol. 852, No. 1, pp. 14-25). American Institute of Physics.

Dabiri, S., Mehrpooya, M. and Nezhad, E.G., 2018. Latent and sensible heat analysis of PCM incorporated in a brick for cold and hot climatic conditions, utilizing computational fluid dynamics. *Energy*, *159*, pp.160-171.

Das, S.B., Joughin, I., Behn, M.D., Howat, I.M., King, M.A., Lizarralde, D. and Bhatia, M.P., 2008. Fracture propagation to the base of the Greenland Ice Sheet during supraglacial lake drainage. *Science*, *320*(5877), pp.778-781.

David, T. W. E. & Priestley, R. E. Geological Observations in Antarctica by the British Antarctic Expedition 1907–1909 (JP Lippincott, 1909).

Dell, R., Arnold, N., Willis, I., Banwell A., Williamson A., and Pritchard H. (2020). Lateral meltwater transfer across an Antarctic Ice Shelf. *The Cryosphere. 316.*

Dinniman, M.S., Asay-Davis, X.S., Galton-Fenzi, B.K., Holland, P.R., Jenkins, A. and Timmermann, R., 2016. Modeling ice shelf/ocean interaction in Antarctica: A review. *Oceanography*, *29*(4), pp.144-153.

Doyle, S.H., Hubbard, A.L., Dow, C.F., Jones, G.A., Fitzpatrick, A.A.W., Gusmeroli, A., Kulessa, B., Lindback, K., Pettersson, R. and Box, J.E., 2013. Ice tectonic deformation during the rapid in situ drainage of a supraglacial lake on the Greenland Ice Sheet. *Cryosphere*, *7*(1), pp.129-140.

Ebert, E.E. and Curry, J.A., 1993. An intermediate one-dimensional thermodynamic sea ice model for investigating ice-atmosphere interactions. *Journal of Geophysical Research: Oceans*, *98*(C6), pp.10085-10109.

Encyclopædia Britannica, 2016. Richardson number: The Editors of Encyclopaedia Britannica. Published: October 24, 2016. Accessed at: https://www.britannica.com/science/Richardson-number on 01/01/20.

Ettema J, van den Broeke MR, van Meijgaard E, et al. (2009) Higher surface mass balance of the Greenland ice sheet revealed by high-resolution climate modeling. *Geophysical Research Letters* 36(12): 1–5.

Fitzpatrick, A.A.W., Hubbard, A.L., Box, J.E., Quincey, D.J., Van As, D., Mikkelsen, A., Doyle, S.H., Dow, C.F., Hasholt, B. and Jones, G.A., 2014. A decade (2002–2012) of supraglacial lake volume estimates across Russell Glacier, West Greenland. *Cryosphere*, *8*(1), pp.107-121.

Fretwell, P., Pritchard, H.D., Vaughan, D.G., Bamber, J.L., Barrand, N.E., Bell, R., Bianchi, C., Bingham, R.G., Blankenship, D.D., Casassa, G. and Catania, G., 2013. Bedmap2: improved ice bed, surface and thickness datasets for Antarctica. *The Cryosphere*, *7*(1), pp.375-393.

Frezzotti, M., Boghosian, A. and Lee, W. S.: Antarctic ice shelf potentially stabilized by 634 export of meltwater in surface river, Nature, 544(7650), 344–348, 635 doi:10.1038/nature22048, 2017.

Gallegos, C.L. and Moore, K.A., 2000. Factors contributing to water-column light attenuation. *Chesapeake bay submerged aquatic vegetation water quality and habitat-based requirements and restoration targets: A second technical synthesis*.

Gardner, A.S., Sharp, M.J., Koerner, R.M., Labine, C., Boon, S., Marshall, S.J., Burgess, D.O. and Lewis, D., 2009. Near-surface temperature lapse rates over Arctic glaciers and their implications for temperature downscaling. *Journal of Climate*, *22*(16), pp.4281-4298.

Ghulam, A., 2010. Calculating surface temperature using Landsat thermal imagery. *Department of Earth & Atmospheric Sciences, and Center for Environmental Sciences*, pp.9829-9852.

Glasser, N.F. and Scambos, T.A., 2008. A structural glaciological analysis of the 2002 Larsen B ice-shelf collapse. *Journal of Glaciology*, *54*(184), pp.3-16.

Gorelick, N.; Hancher, M.; Dixon, M.; Ilyushchenko, S.; Thau, D.; Moore, R. Google Earth Engine: Planetary-scale geospatial analysis for everyone. Remote Sens. Environ. 2017, 202, 18–27

Grant Petty (2006). A First Course in Atmospheric Radiation (2nd Ed.). Sundog Publishing (Madison, Wisconsin). ISBN 978-0-9729033-1-8.

Grenfell, T.C. and Perovich, D.K., 2004. Seasonal and spatial evolution of albedo in a snow-ice-land-ocean environment. *Journal of Geophysical Research: Oceans*, *109*(C1).

Gupta, R.P., Haritashya, U. K., and Singh, P.: Mapping dry/wet snow cover in the Indian Himalayas using IRS multispectral imagery, Remote Sens. Environ., 97(4), 458–469, 2005.

Hall, D.K., Riggs, G.A., Salomonson, V.V., Barton, J.S., Casey, K., Chien, J.Y.L., DiGirolamo, N.E., Klein, A.G., Powell, H.W. and Tait, A.B., 2001. Algorithm theoretical basis document (ATBD) for the MODIS snow and sea ice-mapping algorithms. *Nasa Gsfc*, *45*.

Holland, P. R., Brisbourne, A., Corr, H. F. J., McGrath, D., Purdon, K., Paden, J., Fricker, H. A., Paolo, F. S., and Fleming, A. H.: Oceanic and atmospheric forcing of Larsen C Ice-Shelf thinning, The Cryosphere, 9, 1005–1024, https://doi.org/10.5194/tc-9-1005-2015, 2015.

Holland, P.R., Jenkins, A. and Holland, D.M., 2008. The response of ice shelf basal melting to variations in ocean temperature. *Journal of Climate*, *21*(11), pp.2558-2572.

Horwath, M., Dietrich, R., Baessler, M., Nixdorf, U., Steinhage, D., Fritzsche, D., Damm, V., and Reitmayr, G.: Nivlisen, an Antarctic ice shelf in Dronning Maud Land: geodetic – glaciological results from a combined analysis of ice thickness, ice surface height and ice-flow observations, J. Glaciol., 52, 17–30, https://doi.org/10.3189/172756506781828953, 2006.

Howat, I. M., Porter, C., Smith, B. E., Noh, M.-J., and Morin, P.: The Reference Elevation Model of Antarctica, The Cryosphere, 13, 665-674, 2019.

Hwang, B.J., Ehn, J.K. and Barber, D.G., 2008. Impact of ice temperature on microwave emissivity of thin newly formed sea ice. *Journal of Geophysical Research: Oceans*, *113*(C2).

Jakobs, C.L., Reijmer, C.H., Kuipers Munneke, P., König-Langlo, G. and Van Den Broeke, M.R., 2019. Quantifying the snowmelt-albedo feedback at Neumayer Station, East Antarctica. *Cryosphere*, *13*(5), pp.1473-1485.

Jawak, S.D., Kulkarni, K. and Luis, A.J., 2015. A review on extraction of lakes from remotely sensed optical satellite data with a special focus on cryospheric lakes. *Advances in Remote Sensing*, *4*(03), p.196.

Jolliffe, I.T. and Cadima, J., 2016. Principal component analysis: a review and recent developments. *Philosophical Transactions of the Royal Society A: Mathematical, Physical and Engineering Sciences*, *374*(2065), p.20150202.

Kinar, N. J., and J. W. Pomeroy (2015), Measurement of the physical properties of the snowpack, Rev. Geophys., 53, doi:10.1002/2015RG000481.

Kingslake, J., Ely, J.C., Das, I. and Bell, R.E., 2017. Widespread movement of meltwater onto and across Antarctic ice shelves. *Nature*, *544*(7650), pp.349-352.

Kingslake, J., Ng, F., and Sole, A.: Modelling channelized surface drainage of supraglacial lakes, J. Glaciol., 61, 185–199, https://doi.org/10.3189/2015JoG14J158, 2015.

Konzelmann, T. and Braithwaite, R.J., 1995. Variations of ablation, albedo and energy balance at the margin of the Greenland ice sheet, Kronprins Christian Land, eastern north Greenland. *Journal of Glaciology*, *41*(137), pp.174-182.

Kuipers Munneke, P., McGrath, D., Medley, B., Luckman, A., Bevan, S., Kulessa, B., Jansen, D., Booth, A., Smeets, P., Hubbard, B. and Ashmore, D., 2017. Observationally constrained surface mass balance of Larsen C ice shelf, Antarctica. *The Cryosphere*, *11*, pp.2411-2426.

Kuipers Munneke, P., Van den Broeke, M.R., King, J.C., Gray, T. and Reijmer, C.H., 2012. Near-surface climate and surface energy budget of Larsen C ice shelf, Antarctic Peninsula. The Cryosphere, 6(2), pp.353-363.

Lakhankar, T. Azar, A.E., Shahroudi, N., Powell, A.M., Khanbilvardi., R. (2012). Analysis of the Effects of Snowpack Properties on Satellite Microwave Brightness Temperature and Emissivity Data. Volume 1 - Issue 1 – 1000101. J Geophys Remote Sensing. ISSN:2169-0049 JGRS [25].

Langley, E.S., Leeson, A.A., Stokes, C.R. and Jamieson, S.S., 2016. Seasonal evolution of supraglacial lakes on an East Antarctic outlet glacier. *Geophysical Research Letters*, *43*(16), pp.8563-8571.

Law, R., Arnold, N., Benedek, C., Tedesco, M., Banwell, A. and Willis, I., 2020. Over-winter persistence of supraglacial lakes on the Greenland Ice Sheet: results and insights from a new model. *Journal of Glaciology*, v. 66, p.362-372. doi:10.1017/jog.2020.7

Law, R., 2020. *The development and application of IceLake, an accurate and computationally efficient model of supraglacial lake evolution in the ablation zone of the Greenland Ice Sheet* (Doctoral dissertation, University of Cambridge).

Leeson, A.A., Shepherd, A., Briggs, K., Howat, I., Fettweis, X., Morlighem, M. and Rignot, E., 2015. Supraglacial lakes on the Greenland ice sheet advance inland under warming climate. *Nature Climate Change*, *5*(1), pp.51-55.

Lenaerts, J.T.M., Lhermitte, S., Drews, R., Ligtenberg, S.R.M., Berger, S., Helm, V., Smeets, C.J.P.P., Van den Broeke, M.R., Van De Berg, W.J., Van Meijgaard, E. and Eijkelboom, M., 2017. Meltwater produced by wind–albedo interaction stored in an East Antarctic ice shelf. Nature climate change, 7(1), p.58.

Liang, S., 2001. Narrowband to broadband conversions of land surface albedo I: Algorithms*. Remote sensing of environment,* 76(2), pp.213-238.

Lindbäck, K., Moholdt, G., Nicholls, K.W., Hattermann, T., Pratap, B., Thamban, M. and Matsuoka, K., 2019. Spatial and temporal variations in basal melting at Nivlisen ice shelf, East Antarctica, derived from phase-sensitive radars. *The Cryosphere*, *13*(10), pp.2579-2595.

Luckman, A., Elvidge, A., Jansen, D., Kulessa, B., Munneke, P.K., King, J. and Barrand, N.E., 2014. Surface melt and ponding on Larsen C Ice Shelf and the impact of föhn winds. *Antarctic Science*, *26*(6), pp.625-635.

Lüthje, M., Pedersen, L.T., Reeh, N. and Greuell, W., 2006. Modelling the evolution of supraglacial lakes on the West Greenland ice-sheet margin. *Journal of Glaciology*, *52*(179), pp.608-618.

MacAyeal, D. R., and O. V. Sergienko (2013), Flexural dynamics of melting ice shelves, Ann. Glaciol., 54(63), 1–10, doi:10.3189/2013AoG63A256.

Macdonald, G.J., Banwell, A.F. and MacAyeal, D.R., 2018. Seasonal evolution of supraglacial lakes on a floating ice tongue, Petermann Glacier, Greenland. *Annals of Glaciology*, *59*(76pt1), pp.56-65.

Makshtas, A.P. and Podgorny, I.A., 1996. Calculation of melt pond albedos on arctic sea ice. *Polar Research*, *15*(1), pp.43-52.

Malakar, N.K., Hulley, G.C., Hook, S.J., Laraby, K., Cook, M. and Schott, J.R., 2018. An operational land surface temperature product for Landsat thermal data: Methodology and validation. IEEE *Transactions on Geoscience and Remote Sensing*, 56(10), pp.5717-5735.

Marshall, H.P., Koh, G. and Forster, R.R., 2005. Estimating alpine snowpack properties using FMCW radar. Annals of Glaciology, 40, pp.157-162.

Matsuoka, K., Hindmarsh, R. C. A., Moholdt, G., Bentley, M. J., Pritchard, H. D., Brown, J., Conway, H., Drews, R., Durand, G., Goldberg, D., Hattermann, T., Kingslake, J., Lenaerts, J. T. M., Martín, C., Mulvaney, R., Nicholls, K. W., Pattyn, F., Ross, N., Scambos, T., and Whitehouse, P. L.: Antarctic ice rises and rumples: Their properties and significance for ice-sheet dynamics and evolution, Earth Sci. Rev., 150, 724–745, https://doi.org/10.1016/j.earscirev.2015.09.004, 2015.

Mertes, J.R., Thompson, S.S., Booth, A.D., Gulley, J.D. and Benn, D.I., 2017. A conceptual model of supra-glacial lake formation on debris-covered glaciers based on GPR facies analysis. *Earth Surface Processes and Landforms*, *42*(6), pp.903-914.

Miles, E.S., Pellicciotti, F., Willis, I.C., Steiner, J.F., Buri, P. and Arnold, N.S., 2016. Refined energy-balance modelling of a supraglacial pond, Langtang Khola, Nepal. *Annals of Glaciology*, *57*(71).

Miles, E.S.; Steiner, J.; Willis, I.; Buri, P.; Immerzeel, W.W.; Chesnokova, A.; Pellicciotti, F. Pond Dynamics and Supraglacial-Englacial Connectivity on Debris-Covered Lirung Glacier, Nepal. Available online: https://www.frontiersin.org/articles/10.3389/feart.2017.00069/full (accessed on 1 May 2019).

Miles, K.E., Willis, I.C., Benedek, C.L., Williamson, A.G. and Tedesco, M., 2017. Toward monitoring surface and subsurface lakes on the Greenland ice sheet using Sentinel-1 SAR and Landsat-8 OLI imagery. Frontiers in Earth Science, 5, p.58.

Miles, E.S.; Willis, I.C.; Arnold, N.S.; Steiner, J.; Pellicciotti, F. Spatial, seasonal and interannual variability of supraglacial ponds in the Langtang Valley of Nepal, 1999–2013. J. Glaciol. 2017, 63, 88–105. [CrossRef]

Moelg, T., Cullen, N.J. and Kaser, G., 2009. Solar radiation, cloudiness and longwave radiation over low-latitude glaciers: implications for mass-balance modelling. *Journal of Glaciology*, *55*(190), pp.292-302.

Morcrette, J.J. and Fouquart, Y., 1985. On systematic errors in parametrized calculations of longwave radiation transfer. *Quarterly Journal of the Royal Meteorological Society*, 111(469), pp.691-708.

Morriss, B.F., Hawley, R.L., Chipman, J.W., Andrews, L.C., Catania, G.A., Hoffman, M.J., Lüthi, M.P. and Neumann, T.A., 2013. A ten-year record of supraglacial lake evolution and rapid drainage in West Greenland using an automated processing algorithm for multispectral imagery. *The Cryosphere*, *7*, pp.1869-1877.

Moussavi, M.S., Abdalati, W., Pope, A., Scambos, T., Tedesco, M., MacFerrin, M. and Grigsby, S., 2016. Derivation and validation of supraglacial lake volumes on the Greenland Ice Sheet from high-resolution satellite imagery. *Remote Sensing of Environment*, *183*, pp.294-303.

Mullen, P.C. and Warren, S.G., 1988. Theory of the optical properties of lake ice. *Journal of Geophysical Research: Atmospheres*, *93*(D7), pp.8403-8414.

Munneke, P.K., Ligtenberg, S.R., Van Den Broeke, M.R. and Vaughan, D.G., 2014. Firn air depletion as a precursor of Antarctic ice-shelf collapse. *Journal of Glaciology*, *60*(220), pp.205-214.

Palchetti, L., Bianchini, G., Carli, B., Cortesi, U. and Del Bianco, S., 2008. Measurement of the water vapour vertical profile and of the Earth's outgoing far infrared flux.

Pallant, J., 2005. *Statistical package for the social sciences (SPSS).* Survival Manual.

Panday, P.K., Bulley, H., Haritashya, U. and Ghimire, B., 2011. Supraglacial Lake classification in the Everest region of Nepal Himalaya. In *Geospatial Techniques for Managing Environmental Resources* (pp. 86-99). Springer, Dordrecht.

Picard, G., Fily, M. and Gallée, H., 2007. Surface melting derived from microwave radiometers: a climatic indicator in Antarctica. *Annals of Glaciology*, *46*, pp.29-34.

Pirazzini, R., 2009. Challenges in snow and ice albedo parameterizations. *Geophysica*, *45*(1-2), pp.41-62.

Pope, R. M. and Fry, E. S.: Absorption spectrum (380–700 nm) of pure water. II. Integrating cavity measurements, Appl. Opt., 36, 8710–8723, 1997.

Raupach, M.R. and Finnigan, J.J., 1997. The influence of topography on meteorogical variables and surface-atmosphere interactions. *Journal of Hydrology*, *190*(3-4), pp.182-213.

Reid, T.D. and Brock, B.W., 2014. Assessing ice-cliff backwasting and its contribution to total ablation of debris-covered Miage glacier, Mont Blanc massif, Italy. *Journal of Glaciology*, *60*(219), pp.3-13.

Rignot, E., Casassa, G., Gogineni, P., Krabill, W., Rivera, A.U. and Thomas, R., 2004. Accelerated ice discharge from the Antarctic Peninsula following the collapse of Larsen B ice shelf. *Geophysical research letters*, *31*(18).

Rignot, E., 2006. Changes in ice dynamics and mass balance of the Antarctic ice sheet. Philosophical Transactions of the Royal Society A: *Mathematical, Physical and Engineering Sciences*, 364(1844), pp.1637-1655.

Rignot, E., Jacobs, S., Mouginot, J., and Scheuchl, B.: Ice-Shelf Melting Around Antarctica, Science, 341, 266–270, https://doi.org/10.1126/science.1235798, 2013.

Rott, H., Abdel Jaber, W., Wuite, J., Scheiblauer, S., Floricioiu, D., Van Wessem, J.M., Nagler, T., Miranda, N. and Van Den Broeke, M.R., 2018. Changing pattern of ice flow and mass balance for glaciers discharging into the Larsen A and B embayments, Antarctic Peninsula, 2011 to 2016. *Cryosphere*, 12(4), pp.1273-1291.

Rösel, A. and Kaleschke, L., 2011. Comparison of different retrieval techniques for melt ponds on Arctic sea ice from Landsat and MODIS satellite data. *Annals of Glaciology*, *52*(57), pp.185-191.

Roy, D.P., Wulder, M.A., Loveland, T.R., Woodcock, C.E., Allen, R.G., Anderson, M.C., Helder, D., Irons, J.R., Johnson, D.M., Kennedy, R. and Scambos, T.A., 2014. Landsat-8: Science and product vision for terrestrial global change research. *Remote sensing of Environment*, *145*, pp.154-172.

Saitoh, T.M., Tamagawa, I., Muraoka, H. and Koizumi, H., 2011. Energy balance closure over a cool temperate forest in steeply sloping topography during snowfall and snow-free periods. *Journal of Agricultural Meteorology*, pp.1103090078-1103090078.

Sakai, A.; Takeuchi, N.; Fujita, K.; Nakawo, M. Role of Supraglacial Ponds in the Ablation Process of a Debris-Covered Glacier in the Nepal Himalayas. Available online: http://hydrologie.org/redbooks/a264/ iahs_264_0119.pdf (accessed on 1 May 2020).

Scambos, T., Fricker, H.A., Liu, C.C., Bohlander, J., Fastook, J., Sargent, A., Massom, R. and Wu, A.M., 2009. Ice shelf disintegration by plate bending and hydro-fracture: Satellite observations and model results of the 2008 Wilkins ice shelf break-ups. *Earth and Planetary Science Letters*, *280*(1-4), pp.51-60.

Schneebeli, M., 1995. Development and stability of preferential flow paths in a layered snowpack. *IAHS Publications-Series of Proceedings and Reports-Intern Assoc Hydrological Sciences*, *228*, pp.89-96.

Selmes, N., Murray, T. and James, T.D., 2011. Fast draining lakes on the Greenland Ice Sheet. *Geophysical Research Letters*, *38*(15).

Shepherd, A., Ivins, E.R., Geruo, A., Barletta, V.R., Bentley, M.J., Bettadpur, S., Briggs, K.H., Bromwich, D.H., Forsberg, R., Galin, N. and Horwath, M., 2012. A reconciled estimate of ice-sheet mass balance. *Science*, 338(6111), pp.1183-1189.

Shepherd, A., Ivins, E., Rignot, E. *et al.* Mass balance of the Antarctic Ice Sheet from 1992 to 2017. *Nature* 558, 219–222 (2018) doi:10.1038/s41586-018-0179-y

Shukla, A., Garg, P.K. and Srivastava, S., 2018. Evolution of glacial and high-altitude lakes in the Sikkim, Eastern Himalaya over the past four decades (1975–2017). *Frontiers in Environmental Science*, *6*, p.81.

Silva, B.B.D., Braga, A.C., Braga, C.C., de Oliveira, L.M., Montenegro, S.M. and Barbosa Junior, B., 2016. Procedures for calculation of the albedo with OLI-Landsat 8 images: Application to the Brazilian semi-arid. *Revista Brasileira de Engenharia Agrícola e Ambiental*, *20*(1), pp.3-8.
Sneed, W.A. and Hamilton, G.S., 2007. Evolution of melt pond volume on the surface of the Greenland Ice Sheet. *Geophysical Research Letters*, *34*(3).

Steiner, J.F., Pellicciotti, F., Buri, P., Miles, E.S., Immerzeel, W.W. and Reid, T.D., 2015. Modelling ice-cliff backwasting on a debris-covered glacier in the Nepalese Himalaya. *Journal of Glaciology*, *61*(229), pp.889-907.

Stevens, L.A., Behn, M.D., McGuire, J.J., Das, S.B., Joughin, I., Herring, T., Shean, D.E. and King, M.A., 2015. Greenland supraglacial lake drainages triggered by hydrologically induced basal slip. *Nature*, *522*(7554), pp.73-76.

Sun, F., Sun, W., Chen, J. and Gong, P., 2012. Comparison and improvement of methods for identifying waterbodies in remotely sensed imagery. *International journal of remote sensing*, *33*(21), pp.6854-6875.

Techel, F., Pielmeier, C. and Schneebeli, M., 2011. Microstructural resistance of snow following first wetting. *Cold Regions Science and Technology*, *65*(3), pp.382-391.

Tedesco, M. and Steiner, N., 2011. In-situ multispectral and bathymetric measurements over a supraglacial lake in western Greenland using a remotely controlled watercraft.

Tedesco, M., 2009. Assessment and development of snowmelt retrieval algorithms over Antarctica from K-band spaceborne brightness temperature (1979–2008). *Remote Sensing of Environment*, *113*(5), pp.979-997.

Tedesco, M., Lüthje, M., Steffen, K., Steiner, N., Fettweis, X., Willis, I., Bayou, N. and Banwell, A., 2012. Measurement and modeling of ablation of the bottom of supraglacial lakes in western Greenland. *Geophysical Research Letters*, *39*(2).

Tedesco, M., Willis, I.C., Hoffman, M.J., Banwell, A.F., Alexander, P. and Arnold, N.S., 2013. Ice dynamic response to two modes of surface lake drainage on the Greenland ice sheet. *Environmental Research Letters*, *8*(3), p.034007.

Thompson, A. F., Heywood, K. J., Schmidtko, S., and Stewart, A. L.: Eddy transport as a key component of the Antarctic overturning circulation, Nat. Geosci., 7, 879–884, https://doi.org/10.1038/ngeo2289, 2014.

Thuillier, G., Hersé, M., Foujols, T., Peetermans, W., Gillotay, D., Simon, P.C. and Mandel, H., 2003. The solar spectral irradiance from 200 to 2400 nm as measured by the SOLSPEC spectrometer from the ATLAS and EURECA missions. *Solar Physics*, 214(1), pp.1-22.

Town, M.S., Walden, V.P. and Warren, S.G., 2007. Cloud cover over the South Pole from visual observations, satellite retrievals, and surface-based infrared radiation measurements. *Journal of Climate*, *20*(3), pp.544-559.

Trusel, L.D., Frey, K.E. and Das, S.B., 2012. Antarctic surface melting dynamics: Enhanced perspectives from radar scatterometer data. *Journal of Geophysical Research: Earth Surface*, *117*(F2).

Turner, J., Orr, A., Gudmundsson, G.H., Jenkins, A., Bingham, R.G., Hillenbrand, C.D. and Bracegirdle, T.J., 2017. Atmosphere-ocean-ice interactions in the Amundsen Sea embayment, West Antarctica. *Reviews of Geophysics*, *55*(1), pp.235-276.

van den Broeke MR, Smeets P, Ettema J, et al. (2008) Partitioning of melt energy and meltwater fluxes in the ablation zone of the west Greenland ice sheet. *The Cryosphere* 2: 178–189.

van der Veen, C.J., 2007. Fracture propagation as means of rapidly transferring surface meltwater to the base of glaciers. *Geophysical Research Letters*, *34*(1).

Vanino, S., Nino, P., De Michele, C., Bolognesi, S.F., D'Urso, G., Di Bene, C., Pennelli, B., Vuolo, F., Farina, R., Pulighe, G. and Napoli, R., 2018. Capability of Sentinel-2 data for estimating maximum evapotranspiration and irrigation requirements for tomato crop in Central Italy. *Remote Sensing of Environment*, *215*, pp.452-470.

Wang, K. and Dickinson, R.E., 2013. Global atmospheric downward longwave radiation at the surface from ground-based observations, satellite retrievals, and reanalyses. *Reviews of Geophysics*, *51*(2), pp.150-185.

Watson, C.S.; Quincey, D.J.; Carrivick, J.L.; Smith, M.W.; Rowan, A.V.; Richardson, R. Heterogeneous water storage and thermal regime of supraglacial ponds on debris-covered glaciers. Earth Surf. Process. Landf. 2018, 43, 229–241.

Wessels, R.L., Kargel, J.S. and Kieffer, H.H., 2002. ASTER measurement of supraglacial lakes in the Mount Everest region of the Himalaya. *Annals of Glaciology*, *34*, pp.399-408.

Williamson, A.G., Arnold, N.S., Banwell, A.F. and Willis, I.C., 2017. A Fully Automated Supraglacial lake area and volume Tracking ("FAST") algorithm: Development and application using MODIS imagery of West Greenland. *Remote Sensing of Environment*, *196*, pp.113-133.

Wiscombe, W.J. and Warren, S.G., 1980. A model for the spectral albedo of snow. I: Pure snow. *Journal of the Atmospheric Sciences*, *37*(12), pp.2712-2733.

Wouters, B., Martin-Español, A., Helm, V., Flament, T., van Wessem, J.M., Ligtenberg, S.R., Van den Broeke, M.R. and Bamber, J.L., 2015. Dynamic thinning of glaciers on the Southern Antarctic Peninsula. *Science*, *348*(6237), pp.899-903.

Wuttichaikitcharoen, P. and Babel, M.S., 2014. Principal component and multiple regression analyses for the estimation of suspended sediment yield in ungauged basins of Northern Thailand. *Water*, *6*(8), pp.2412-2435.

Yang, K. and Smith, L.C., 2012. Supraglacial streams on the Greenland Ice Sheet delineated from combined spectral–shape information in high-resolution satellite imagery. *IEEE Geoscience and Remote Sensing Letters*, *10*(4), pp.801-805.

Yang, K. and Smith, L.C., 2016. Internally drained catchments dominate supraglacial hydrology of the southwest Greenland Ice Sheet. *Journal of Geophysical Research: Earth Surface*, *121*(10), pp.1891-1910.

8. Appendix

8.1 Satellite Imagery

Sentinel-2 Image ID	Date	Cloud Cover (%)
COPERNICUS/S2/20161111T074922_20161111T074922_T32DNG	11/11/2016	58
COPERNICUS/S2/20161111T074922_20161111T122828_T32DNG	11/11/2016	58
COPERNICUS/S2/20161114T075922_20161114T075925_T32DNG	14/11/2016	62
COPERNICUS/S2/20161114T075922_20161114T110349_T32DNG	14/11/2016	63
COPERNICUS/S2/20161127T080922_20161127T080925_T32DNG	27/11/2016	61
COPERNICUS/S2/20161127T080922_20161127T111013_T32DNG	27/11/2016	41
COPERNICUS/S2/20161217T080922_20161217T080922_T32DNG	17/12/2016	36
COPERNICUS/S2/20170126T080921_20170126T080920_T32DNG	26/01/2017	9
COPERNICUS/S2/20170225T080921_20170225T080922_T32DNG	25/02/2017	21
COPERNICUS/S2/20170327T080921_20170327T080923_T32DNG	27/03/2017	29
COPERNICUS/S2/20180111T080921_20180111T080919_T32DNG	11/01/2018	19
COPERNICUS/S2/20180128T075921_20180128T075920_T32DNG	28/01/2018	35
COPERNICUS/S2/20180128T075921_20180128T080000_T32DNG	28/01/2018	66
COPERNICUS/S2/20180307T080919_20180307T080917_T32DNG	07/03/2018	26
COPERNICUS/S2/20180327T080929_20180327T080924_T32DNG	27/03/2018	65
COPERNICUS/S2/20181202T080929_20181202T080923_T32DNG	02/12/2018	46
COPERNICUS/S2/20181222T080929_20181222T080923_T32DNG	22/12/2018	0
COPERNICUS/S2/20190101T080929_20190101T080925_T32DNG	01/01/2019	49
COPERNICUS/S2/20190111T080929_20190111T080926_T32DNG	11/01/2019	20
COPERNICUS/S2/20190131T080929_20190131T080941_T32DNG	31/01/2019	16
COPERNICUS/S2/20190302T080929_20190302T080926_T32DNG	02/03/2019	56
COPERNICUS/S2/20190908T080929_20190908T080931_T32DNG	08/09/2019	61
COPERNICUS/S2/20191207T080919_20191207T080946_T32DNG	07/12/2019	36

Table S1. Sentinel-2 images of Nivlisen Ice Shelf TOA reflectance extracted for austral summers of 2017-2020 over the study-site region (Figure 5). Images with <20 % cloud cover (highlighted green) are deemed useful for analysis.

Years	Image ID	Date	WRS Path	WRS Row
2019-2020	LANDSAT/LC08/C01/T2_TOA/LC08_165110_20191111	11/11/2019	165	110
	LANDSAT/LC08/C01/T2_TOA/LC08_165110_20191213	13/12/2019	165	110
	LANDSAT/LC08/C01/T2_TOA/LC08_165110_20191229	29/12/2019	165	110
	LANDSAT/LC08/C01/T2_TOA/LC08_165110_20200114	14/01/2020	165	110
	LANDSAT/LC08/C01/T2_TOA/LC08_166110_20191102	02/11/2019	166	110
	LANDSAT/LC08/C01/T2_TOA/LC08_166110_20191118	18/11/2019	166	110
	LANDSAT/LC08/C01/T2_TOA/LC08_166110_20191204	04/12/2019	166	110
	LANDSAT/LC08/C01/T2_TOA/LC08_167110_20191109	09/11/2019	167	110
	LANDSAT/LC08/C01/T2_TOA/LC08_167110_20191125	25/11/2019	167	110
	LANDSAT/LC08/C01/T2_TOA/LC08_167110_20191211	11/12/2019	167	110

2018-2019	LANDSAT/LC08/C01/T2_TOA/LC08_165110_20181108	08/11/2018	165	110
	LANDSAT/LC08/C01/T2_TOA/LC08_165110_20181210	10/12/2018	165	110
	LANDSAT/LC08/C01/T2_TOA/LC08_166110_20181115	15/11/2018	166	110
	LANDSAT/LC08/C01/T2_TOA/LC08_166110_20181201	01/12/2018	166	110
	LANDSAT/LC08/C01/T2_TOA/LC08_166110_20190102	02/01/2019	166	110
	LANDSAT/LC08/C01/T2_TOA/LC08_166110_20190118	18/01/2019	166	110
	LANDSAT/LC08/C01/T2_TOA/LC08_166110_20190219	19/02/2019	166	110
	LANDSAT/LC08/C01/T2_TOA/LC08_167110_20181106	06/11/2018	167	110
	LANDSAT/LC08/C01/T2_TOA/LC08_167110_20181208	08/12/2018	167	110
	LANDSAT/LC08/C01/T2_TOA/LC08_167110_20181224	24/12/2018	167	110
	LANDSAT/LC08/C01/T2_TOA/LC08_167110_20190125	25/01/2019	167	110
2017-2018	LANDSAT/LC08/C01/T2_TOA/LC08_165110_20180108	08/01/2018	165	110
	LANDSAT/LC08/C01/T2_TOA/LC08_166110_20171214	14/12/2017	166	110
	LANDSAT/LC08/C01/T2_TOA/LC08_167110_20171205	05/12/2017	167	110
	LANDSAT/LC08/C01/T2_TOA/LC08_167110_20171221	21/12/2017	167	110
	LANDSAT/LC08/C01/T2_TOA/LC08_167110_20180207	07/02/2018	167	110
2016-2017	LANDSAT/LC08/C01/T2_TOA/LC08_165110_20161102	02/11/2016	165	110
	LANDSAT/LC08/C01/T2_TOA/LC08_165110_20161204	04/12/2016	165	110
	LANDSAT/LC08/C01/T2_TOA/LC08_165110_20161220	02/12/2016	165	110
	LANDSAT/LC08/C01/T2_TOA/LC08_165110_20170105	05/01/2017	165	110
	LANDSAT/LC08/C01/T2_TOA/LC08_165110_20170121	21/02/2017	165	110
	LANDSAT/LC08/C01/T2_TOA/LC08_166110_20161211	11/12/2016	166	110
	LANDSAT/LC08/C01/T2_TOA/LC08_166110_20161227	27/12/2016	166	110
	LANDSAT/LC08/C01/T2_TOA/LC08_166110_20170112	12/01/2017	166	110
	LANDSAT/LC08/C01/T2_TOA/LC08_166110_20170213	13/02/2017	166	110
	LANDSAT/LC08/C01/T2_TOA/LC08_167110_20161116	16/11/2016	167	110
	LANDSAT/LC08/C01/T2_TOA/LC08_167110_20170119	19/01/2017	167	110
	LANDSAT/LC08/C01/T2_TOA/LC08_167110_20170204	04/02/2017	167	110
2015-2016	LANDSAT/LC08/C01/T2_TOA/LC08_165110_20151202	02/12/2015	165	110
	LANDSAT/LC08/C01/T2_TOA/LC08_165110_20151218	18/12/2015	165	110
	LANDSAT/LC08/C01/T2_TOA/LC08_165110_20160103	03/01/2016	165	110
	LANDSAT/LC08/C01/T2_TOA/LC08_166110_20151123	23/11/2015	166	110
	LANDSAT/LC08/C01/T2_TOA/LC08_166110_20151209	09/12/2015	166	110
	LANDSAT/LC08/C01/T2_TOA/LC08_166110_20160126	26/01/2016	166	110
	LANDSAT/LC08/C01/T2_TOA/LC08_166110_20160211	11/02/2016	166	110

Table S2. Landsat 8 images of Nivlisen Ice Shelf TOA reflectance extracted for austral summers of 2017-2020 with < 20% cloud cover. Images which did not cover the study-site region of NIS are discarded.

8.2 Surface Energy Balance Model Code

Code (1) – surface energy balance model for lake and slush regions on Nivlisen Ice Shelf, EAIS, using Sentinel-2.

Landsat 8 SEB model: https://code.earthengine.google.com/c0cffa9bca56dec2c0d7bab404b2b568
Sentinel-2 SEB model: https://code.earthengine.google.com/79e9e6144b68f6c30d62526fb29b6db3

// Surface Energy Balance Model for Sentinel-2 developed in 2020 for Masters of Philosophy in Polar Studies. Contact Scott Polar Research Institute for further information.

// Permission is hereby granted to any person obtaining a copy of this documentation to make use of it for non-commercial purposes provided that, a) its original authorship is acknowledged and b) no modified versions of the source code are published.

// PARAMETERS

// ice_albedo = 0.65;
// slush_albedo = 0.6; // After Buzzard et al. 2017 following Singh 2011
// snow_albedo = 0.72; // Chen et al. 2014 study of snow albedo with snow depth

// CONSTANTS

// T_melt = 273.15 // (K) Melt temperature of water
// e_ice = 0.99; // Buzzard et al. 2017
// e_lake = 0.97; // Buzzard et al. 2017
// e_slush = 0.985; // estimated from other emissivities and histogram data
// steffan_boltz = 5.67*(10^-8); // W/(m^2).(K^4) Steffan Boltzmann constant
// ro_air = 1.27; // (kg/m^3) Density of dry air
// ro_water = 997; // (kg/m^3) Density of water
// c_air = 1000; // (J/kgK) Specific heat capacity of dry air
// c_water = 4217; // (J/kgK) Specific heat capacity of water
// c_ice = 2108; // (J/kgK) Specific heat capacity of ice
// Lf_water = 3.348*(10^5); // (J/kg) Latent heat of fusion of water
// sgc_air = 287; // (J/kgK) Specific gas constant for dry air
// sgc_vapour = 461; // (J/kgK) Specific gas constant for water vapour
// rough = 10; // (m) Surface roughness

////////// FILTER IMAGE COLLECTION TO GET RELEVANT SENTINEL 2 IMAGE //////////

```
var imagewhole = ee.Image('COPERNICUS/S2/20190131T080929_20190131T080941_T32DNG');

// Define the visualization parameters.
var vizParams = {
  bands: ['B4','B3','B2'],
  min: 0,
  max: 11000,
  gamma: [0.95,1.1,1]
};
Map.addLayer(imagewhole,vizParams,'false colour');
```

```
var image = imagewhole.clip(geometry);

////////////// USE PRINCIPAL COMPONENTS ANALYSIS THRESHOLDS TO CREATE SUPRAGLACIAL
FEATURE MASKS //////////////
// Delineate lake region
var islake = image.expression(
  'NIR < 3485 && B3 < 5985 && B4 < 5395 && B2 < 8000', {
    'SWIR': image.select('B11'),
    'NIR': image.select('B8'),
    'B2': image.select('B2'),
    'B4': image.select('B4'),
    'B3': image.select('B3')
  });

Map.centerObject(image,9);
Map.addLayer(islake,{min: 0, max: 1, palette: ['000000', 'FFFFFF']},'filtered image');
var masklake = islake.eq(1);
var maskedcomposite = image.updateMask(masklake);
Map.addLayer(maskedcomposite,{min: 1, max: 1},'maskedcomposite');

var lakemask = maskedcomposite.divide(10000);
var lakemask_swbands_out = ee.Image(lakemask).select(['B2','B3','B4','B5','B6','B7','B8','B11','B12']);

// Delineate slush region
var slushlake = image.expression(
  '3485 < NIR && NIR < 5835 && 5985 < B3 && B3 < 7395 && 5395 < B4 && B4 < 7205 && 8000 < B2
&& B2 < 9000', {
    'SWIR': image.select('B11'),
    'NIR': image.select('B8'),
    'B2': image.select('B2'),
    'B4': image.select('B4'),
    'B3': image.select('B3')
  });

Map.centerObject(image,9);
Map.addLayer(slushlake,{min: 0, max: 1, palette: ['000000', 'FFFFFF']},'filtered image');
var maskslush = slushlake.eq(1);
var maskedcompositeslush = image.updateMask(maskslush);
Map.addLayer(maskedcompositeslush,{min: 0, max: 1},'slush maskedcomposite');
var slushmask = maskedcompositeslush.divide(10000);
var slushmask_swbands_out =
ee.Image(slushmask).select(['B2','B3','B4','B5','B6','B7','B8','B11','B12']);

// Delineate ice region

var iceregionmask = islake.add(slushlake);
var iceregion = iceregionmask.eq(0);
var icemaskcomposite = image.updateMask(iceregion);
var icemask = icemaskcomposite.divide(10000);
Map.addLayer(icemask,{min:0, max:1},'icemask');
```

```
// Extract lake spectral band values into 2D array
var imagebandslake = ee.Image(lakemask)
.select(['B1','B2','B3','B4','B5','B6','B7','B8','B9','B10','B11','B12']);
var valuesListlake = imagebandslake.reduceRegion({
  reducer: ee.Reducer.toList(12),
  geometry: geometry
}).values().get(0);

var valuesList = ee.List(valuesListlake); // Cast valuesList
var myFeatures = ee.FeatureCollection(valuesList.map(function(el){
  el = ee.List(el); // cast every element of the list
  var geom = ee.Geometry(geometry);
  return ee.Feature(geom,
{'B1':ee.Number(el.get(0)),'B2':ee.Number(el.get(1)),'B3':ee.Number(el.get(2)),'B4':ee.Number(el.ge
t(3)),
'B5':ee.Number(el.get(4)),'B6':ee.Number(el.get(5)),'B7':ee.Number(el.get(6)),'B8':ee.Number(el.get
(7)),'B9':ee.Number(el.get(8)),'B10':ee.Number(el.get(9)),'B11':ee.Number(el.get(10)),'B12':ee.Numb
er(el.get(11))});
}));

// Extract slush spectral band values into 2D array
var imagebandsslush = ee.Image(slushmask)
.select(['B1','B2','B3','B4','B5','B6','B7','B8','B9','B10','B11','B12']);
var valuesListslush = imagebandsslush.reduceRegion({
  reducer: ee.Reducer.toList(12),
  geometry: geometry
}).values().get(0);
var valuesList2 = ee.List(valuesListslush); // Cast valuesList
var myFeaturesslush = ee.FeatureCollection(valuesList2.map(function(el){
  el = ee.List(el); // cast every element of the list
  var geom = ee.Geometry(geometry);
  return ee.Feature(geom,
{'B1':ee.Number(el.get(0)),'B2':ee.Number(el.get(1)),'B3':ee.Number(el.get(2)),'B4':ee.Number(el.ge
t(3)),
'B5':ee.Number(el.get(4)),'B6':ee.Number(el.get(5)),'B7':ee.Number(el.get(6)),'B8':ee.Number(el.get
(7)),'B9':ee.Number(el.get(8)),'B10':ee.Number(el.get(9)),'B11':ee.Number(el.get(10)),'B12':ee.Numb
er(el.get(11))});
}));


// Extract ice spectral bands into 2D array

var imagebandice = ee.Image(icemask).select(['B1','B2','B3','B4','B5','B6','B7']);

var valuesListice = imagebandice.reduceRegion({
  reducer: ee.Reducer.toList(7),
  geometry: grid
}).values().get(0);

var valuesList3 = ee.List(valuesListice); // Cast valuesList
```

```
var myFeaturesice = ee.FeatureCollection(valuesList3.map(function(el){
  el = ee.List(el); // cast every element of the list
  var geom = ee.Geometry(grid);
  return ee.Feature(geom,
{'B1':ee.Number(el.get(0)),'B2':ee.Number(el.get(1)),'B3':ee.Number(el.get(2)),'B4':ee.Number(el.ge
t(3)), 'B5':ee.Number(el.get(4)),'B6':ee.Number(el.get(5)),'B7':ee.Number(el.get(6))});
}));



////////////////// SURFACE ENERGY BALANCE MODEL (2020) /////////////////
// SEB calculates shortwave, longwave, sensible and latent energy fluxes separately
// All elements are summed for each 30 m Landsat pixel within lake and slush regions
// Global Forecast System Meteorological Data collected 6 hourly intervals with sufficient coverage
over EAIS

///// INCOMING SHORTWAVE RADIATION DATA //////////////
var dataset = ee.ImageCollection('NOAA/GFS0P25')
              .filter(ee.Filter.date('2017-01-27', '2017-01-28'))
              .filter(ee.Filter.eq('forecast_hours', 1))
              .filterBounds(ee.Geometry(grid));
 print(dataset);

var shortwaverad = dataset.select(['downward_shortwave_radiation_flux']);
var visParams = {
  min: 0.0,
  max: 1230.0,
  palette: ['blue', 'purple', 'cyan', 'green', 'yellow', 'red'],
};
var listOfImages = shortwaverad.toList(shortwaverad.size());
var SW_rad_list = listOfImages.get(0);
var Image1 = ee.Image(SW_rad_list);
print(Image1);
Map.addLayer(shortwaverad, visParams, 'sw radiation');


////////// INCOMING SW RADIATION FOR EACH BAND //////////////
// Scalar multipliers applied here are weighting coefficients (see Tables 6 & 7)

var B2_incoming = Image1.multiply(0.1324);
var B3_incoming = Image1.multiply(0.1269);
var B4_incoming = Image1.multiply(0.1051);
var B5_incoming = Image1.multiply(0.0971);
var B6_incoming = Image1.multiply(0.089);
var B7_incoming = Image1.multiply(0.0818);
var B8_incoming = Image1.multiply(0.0722);

// GENERATE AN IMAGE ARRAY OF 1 //
var create_1 = dataset.select(['precipitable_water_entire_atmosphere']);
var visParams = {
  min: 0.0,
```

```
  max: 1230.0,
  palette: ['blue', 'purple', 'cyan', 'green', 'yellow', 'red'],
};
var listOfImages = create_1.toList(create_1.size());
var image_array_list = listOfImages.get(0);
var image_array = ee.Image(image_array_list);
var image_array_1 = image_array.divide(image_array);

// 1 - REFLECTANCE OF SW RADIATION FOR EACH BAND LAKE PIXELS //

var B2_outgoing_lake = image_array_1.subtract(lakemask.select(['B2']));
var B3_outgoing_lake = image_array_1.subtract(lakemask.select(['B3']));
var B4_outgoing_lake = image_array_1.subtract(lakemask.select(['B4']));
var B5_outgoing_lake = image_array_1.subtract(lakemask.select(['B5']));
var B6_outgoing_lake = image_array_1.subtract(lakemask.select(['B6']));
var B7_outgoing_lake = image_array_1.subtract(lakemask.select(['B7']));
var B8_outgoing_lake = image_array_1.subtract(lakemask.select(['B8']));

// REFLECTANCE OF SW RADIATION FOR EACH BAND SLUSH PIXELS //

var B2_outgoing_slush = image_array_1.subtract(slushmask.select(['B2']));
var B3_outgoing_slush = image_array_1.subtract(slushmask.select(['B3']));
var B4_outgoing_slush = image_array_1.subtract(slushmask.select(['B4']));
var B5_outgoing_slush = image_array_1.subtract(slushmask.select(['B5']));
var B6_outgoing_slush = image_array_1.subtract(slushmask.select(['B6']));
var B7_outgoing_slush = image_array_1.subtract(slushmask.select(['B7']));
var B8_outgoing_slush = image_array_1.subtract(slushmask.select(['B8']));

// REFLECTANCE OF SW RADIATION FOR EACH BAND ICE PIXELS //

var B2_outgoing_ice = image_array_1.subtract(icemask.select(['B2']));
var B3_outgoing_ice = image_array_1.subtract(icemask.select(['B3']));
var B4_outgoing_ice = image_array_1.subtract(icemask.select(['B4']));
var B5_outgoing_ice = image_array_1.subtract(icemask.select(['B5']));
var B6_outgoing_ice = image_array_1.subtract(icemask.select(['B6']));
var B7_outgoing_ice = image_array_1.subtract(icemask.select(['B7']));
var B8_outgoing_ice = image_array_1.subtract(icemask.select(['B8']));

// Total shortwave radiation flux across each band for lake pixels //

var SW_flux_B2_lake = B2_incoming.multiply(B2_outgoing_lake);
var SW_flux_B3_lake = B3_incoming.multiply(B3_outgoing_lake);
var SW_flux_B4_lake = B4_incoming.multiply(B4_outgoing_lake);
var SW_flux_B5_lake = B5_incoming.multiply(B5_outgoing_lake);
var SW_flux_B6_lake = B6_incoming.multiply(B6_outgoing_lake);
var SW_flux_B7_lake = B7_incoming.multiply(B7_outgoing_lake);
var SW_flux_B8_lake = B8_incoming.multiply(B8_outgoing_lake);

// Total shortwave radiation flux across each band for slush pixels //

var SW_flux_B2_slush = B2_incoming.multiply(B2_outgoing_slush);
```

```
var SW_flux_B3_slush = B3_incoming.multiply(B3_outgoing_slush);
var SW_flux_B4_slush = B4_incoming.multiply(B4_outgoing_slush);
var SW_flux_B5_slush = B5_incoming.multiply(B5_outgoing_slush);
var SW_flux_B6_slush = B6_incoming.multiply(B6_outgoing_slush);
var SW_flux_B7_slush = B7_incoming.multiply(B7_outgoing_slush);
var SW_flux_B8_slush = B8_incoming.multiply(B8_outgoing_slush);

// Total shortwave radiation flux across each band for ice pixels//

var SW_flux_B2_ice = B2_incoming.multiply(B2_outgoing_ice);
var SW_flux_B3_ice = B3_incoming.multiply(B3_outgoing_ice);
var SW_flux_B4_ice = B4_incoming.multiply(B4_outgoing_ice);
var SW_flux_B5_ice = B5_incoming.multiply(B5_outgoing_ice);
var SW_flux_B6_ice = B6_incoming.multiply(B6_outgoing_ice);
var SW_flux_B7_ice = B7_incoming.multiply(B7_outgoing_ice);
var SW_flux_B8_ice = B8_incoming.multiply(B8_outgoing_ice);

/////// Sum of shortwave radiation budget across all spectral bands /////
var total_SW_lake =
SW_flux_B2_lake.add(SW_flux_B3_lake).add(SW_flux_B4_lake).add(SW_flux_B5_lake).add(SW_flux
_B6_lake).add(SW_flux_B7_lake).add(SW_flux_B8_lake);

var total_SW_slush =
SW_flux_B2_slush.add(SW_flux_B3_slush).add(SW_flux_B4_slush).add(SW_flux_B5_slush).add(SW_
flux_B6_slush).add(SW_flux_B7_slush).add(SW_flux_B8_slush);

var total_SW_ice =
SW_flux_B2_ice.add(SW_flux_B3_ice).add(SW_flux_B4_ice).add(SW_flux_B5_ice).add(SW_flux_B6_i
ce).add(SW_flux_B7_ice).add(SW_flux_B8_ice);

Map.addLayer(total_SW_lake, visParams,'shortwave lakes');
Map.addLayer(total_SW_slush, visParams,'shortwave slush');

// NET shortwave radiation budget for lake region //
var sum_SW_rad_lake = total_SW_lake.reduceRegion({
  reducer: ee.Reducer.sum(),
  geometry: lakemask.geometry(),
  scale: 10,
  maxPixels: 1e9
});
print(sum_SW_rad_lake, 'sum SW lake');

// AVERAGE shortwave radiation budget for lake region //
var sum_SW_rad_lake_mean = total_SW_lake.reduceRegion({
  reducer: ee.Reducer.mean(),
  geometry: lakemask.geometry(),
  scale: 10,
  maxPixels: 1e9
});
print(sum_SW_rad_lake_mean, 'mean SW lake');
```

```
// NET shortwave radiation budget for slush region //
var sum_SW_rad_slush = total_SW_slush.reduceRegion({
  reducer: ee.Reducer.sum(),
  geometry: slushmask.geometry(),
  scale: 10,
  maxPixels: 1e9
});
print(sum_SW_rad_slush, 'sum SW slush');

// AVERAGE shortwave radiation budget for slush region //

var sum_SW_rad_slush_mean = total_SW_slush.reduceRegion({
  reducer: ee.Reducer.mean(),
  geometry: slushmask.geometry(),
  scale: 10,
  maxPixels: 1e9
});
print(sum_SW_rad_slush_mean, 'mean SW slush');


// NET shortwave radiation budget for ice region //
var sum_SW_rad_ice = total_SW_ice.reduceRegion({
  reducer: ee.Reducer.sum(),
  geometry: icemask.geometry(),
  scale: 10,
  maxPixels: 1e9
});

print(sum_SW_rad_ice, 'sum SW ice');

// AVERAGE shortwave radiation budget for ice region //

var sum_SW_rad_ice_mean = total_SW_ice.reduceRegion({
  reducer: ee.Reducer.mean(),
  geometry: icemask.geometry(),
  scale: 10,
  maxPixels: 1e9
});

print(sum_SW_rad_ice_mean, 'mean SW ice');

////////////// START LONGWAVE CALCULATION////////////////

// Import air temperature data at 2m
var airtemp_2m = dataset.select(['temperature_2m_above_ground']);
var visParams = {
  min: 0.0,
  max: 1230.0,
  palette: ['blue', 'purple', 'cyan', 'green', 'yellow', 'red'],
};
var listOfImages_temp = airtemp_2m.toList(airtemp_2m.size());
```

```
var temp_list = listOfImages_temp.get(0);
var airtemp_image = ee.Image(temp_list);

// Convert temperature in celcius to kelvin //
var airtemp_kelvin = airtemp_image.add(273.15);
Map.addLayer(airtemp_kelvin, visParams, 'airtemp 2m');

// Calculate temperature of pixel at lake surface using bands 11 and 12 SWIR

var convert_irrad_lake = lakemask.expression(
   '14387/(1.6*log(1+119104200/(10.485*((B11 + B12)/ (0.25*1000000)))))', {
     'B11': lakemask.select('B11'),
     'B12': lakemask.select('B12')
});
var visParamslaketemp = {
  min: 253,
  max: 283,
   palette: ['blue', 'yellow', 'red'],
};
Map.addLayer(convert_irrad_lake, visParamslaketemp, 'lake temp kelvin');

// Calculate temperature of pixel at slush surface using bands 11 and 12 SWIR

var convert_irrad_slush = slushmask.expression(
   '14387/(1.6*log(1+119104200/(10.485*((B11 + B12)/ (0.25*1000000)))))', {
     'B11': slushmask.select('B11'),
     'B12': slushmask.select('B12')
});
var visParamsslushtemp = {
  min: 270,
  max: 290,
  palette: ['blue', 'yellow', 'red'],
};
Map.addLayer(convert_irrad_slush, visParamsslushtemp, 'slush temp kelvin');


// Calculate temperature of pixel at ice surface using bands 11 and 12 SWIR

var convert_irrad_ice = icemask.expression(
   '14387/(1.6*log(1+119104200/(10.485*((B11 + B12)/ (0.25*1000000)))))', {
     'B11': icemask.select('B11'),
     'B12': icemask.select('B12')
});

// Calculate incoming and outgoing longwave radiation
// e_lake = 0.97
// e_slush = 0.94
// e_ air = 0.9
// stefan_boltz = 0.0000000567

var LW_in = airtemp_kelvin.pow(4).multiply(0.9).multiply(0.0000000567);
```

```
var LW_out_lake = convert_irrad_lake.pow(4).multiply(0.97).multiply(0.0000000567);

// Calculate net longwave radiation per metre of lake area

var net_LW_lake_per_metre = LW_in.subtract(LW_out_lake);
Map.addLayer(net_LW_lake_per_metre,visParams, 'LW radiation lakes');
var LW_out_slush = convert_irrad_slush.pow(4).multiply(0.94).multiply(0.0000000567);
var net_LW_slush_per_metre = LW_in.subtract(LW_out_slush);

// Map net longwave radiation per metre of lake area
Map.addLayer(net_LW_slush_per_metre,visParams, 'LW radiation slush');

// Calculate NET of longwave radiation for total lake region

var sum_LW_rad_lake = net_LW_lake_per_metre.reduceRegion({
  reducer: ee.Reducer.sum(),
  geometry: lakemask.geometry(),
  scale: 20,
  maxPixels: 1e9
});

// Calculate AVERAGE longwave radiation for lake region
var sum_LW_rad_lake_mean = net_LW_lake_per_metre.reduceRegion({
  reducer: ee.Reducer.mean(),
  geometry: lakemask.geometry(),
  scale: 20,
  maxPixels: 1e9
});
print(sum_LW_rad_lake_mean, 'mean of LW lake');
print(sum_LW_rad_lake, 'sum of LW lake');

// Calulate NET longwave radiation at slush region
var sum_LW_rad_slush = net_LW_slush_per_metre.reduceRegion({
  reducer: ee.Reducer.sum(),
  geometry: slushmask.geometry(),
  scale: 10,
  maxPixels: 1e9
});
print(sum_LW_rad_slush, 'sum of LW slush');

// Calculate AVERAGE longwave radiation at slush
var sum_LW_rad_slush_mean = net_LW_slush_per_metre.reduceRegion({
  reducer: ee.Reducer.mean(),
  geometry: slushmask.geometry(),
  scale: 10,
  maxPixels: 1e9
});
print(sum_LW_rad_slush_mean, 'mean of LW slush');

// Calculate net longwave radiation per metre of ice area //
```

```
var LW_out_ice = convert_irrad_ice.pow(4).multiply(0.99).multiply(0.0000000567);
var net_LW_ice_per_metre = LW_in.subtract(LW_out_ice);
Map.addLayer(net_LW_ice_per_metre,visParams, 'LW radiation ice');


////////////// CALCULATE SENSIBLE HEAT FLUX  ///////////////

// Extract wind speed from GFS data

var wind_speed = dataset.select(['v_component_of_wind_10m_above_ground']);
var visParams_wind = {
  min: -64,
  max: 54,
  palette: ['blue', 'purple', 'cyan', 'green', 'yellow', 'red'],
};
var listOfImages_wind = wind_speed.toList(wind_speed.size());
var wind_list = listOfImages_wind.get(0);
var wind_image = ee.Image(wind_list);
Map.addLayer(wind_image,visParams_wind,'wind speed GFS');

// Wind speed multiplied by temp difference for lake regions

var sens_step1_lake = wind_image.multiply(airtemp_kelvin.subtract(convert_irrad_lake));
var sens_step2_lake = sens_step1_lake.multiply(1275);

// Wind speed multiplied by temp difference for slush regions

var sens_step1_slush = wind_image.multiply(airtemp_kelvin.subtract(convert_irrad_slush));
var sens_step2_slush = sens_step1_slush.multiply(1275);

// Wind speed multiplied by temp difference for ice regions

var sens_step1_ice = wind_image.multiply(airtemp_kelvin.subtract(convert_irrad_ice));
var sens_step2_ice = sens_step1_ice.multiply(1275);

// Calculate Richardson Number at Lake regions

var rich_lake = (airtemp_kelvin.subtract(convert_irrad_lake)).multiply(98);
var rich_lake_2 = rich_lake.divide((wind_image.pow(2)).multiply(airtemp_kelvin));
var mask_lake_ri_negative = rich_lake_2.gt(0);
var lake_ri_negative = rich_lake_2.updateMask(mask_lake_ri_negative);
Map.addLayer(lake_ri_negative, visParams, 'negative richardson for lakes');

var mask_lake_ri_positive = rich_lake_2.lt(0);
var lake_ri_positive = rich_lake_2.updateMask(mask_lake_ri_positive);
Map.addLayer(lake_ri_positive, visParams, 'positive richardson for lakes');

// Calculate Richardson Number at Slush regions

var rich_slush = (airtemp_kelvin.subtract(convert_irrad_slush)).multiply(98);
```

```
var rich_slush_2 = rich_slush.divide((wind_image.pow(2)).multiply(airtemp_kelvin));
var mask_slush_ri_negative = rich_slush_2.gt(0);
var slush_ri_negative = rich_slush_2.updateMask(mask_slush_ri_negative);
Map.addLayer(slush_ri_negative, visParams, 'negative richardson for slush');

var mask_slush_ri_positive = rich_slush_2.lt(0);
var slush_ri_positive = rich_slush_2.updateMask(mask_slush_ri_positive);
Map.addLayer(slush_ri_positive, visParams, 'positive richardson for slush');

// Calculate Richardson Number at ice regions

var rich_ice = (airtemp_kelvin.subtract(convert_irrad_ice)).multiply(98);
var rich_ice_2 = rich_ice.divide((wind_image.pow(2)).multiply(airtemp_kelvin));
var mask_ice_ri_negative = rich_ice_2.gt(0);
var ice_ri_negative = rich_ice_2.updateMask(mask_ice_ri_negative);
Map.addLayer(ice_ri_negative, visParams, 'negative richardson for ice');

var mask_ice_ri_positive = rich_ice_2.lt(0);
var ice_ri_positive = rich_ice_2.updateMask(mask_ice_ri_positive);
Map.addLayer(ice_ri_positive, visParams, 'positive richardson for ice');

// Calculate Ct... If Ri < 0   lake

var ct_lake_numerator = lake_ri_negative.multiply(-0.0452).add(0.0013);
var ct_lake_denominator = (lake_ri_negative.pow(0.5).multiply(50.986)).add(1);
var Ct_lake_ri_negative = ct_lake_numerator.divide(ct_lake_denominator);

// // Calculate Ct... If Ri < 0   slush - commented because slush ri is always positive

// var ct_slush_numerator = rich_slush_2.multiply(-0.0452).add(0.0013);
// var ct_slush_denominator = (rich_slush_2.pow(0.5).multiply(50.986)).add(1);
// var Ct_slush_ri_negative = ct_slush_numerator.divide(ct_slush_denominator);

// Calculate Ct... If Ri < 0   ice

var ct_ice_numerator = ice_ri_negative.multiply(-0.0452).add(0.0013);
var ct_ice_denominator = (ice_ri_negative.pow(0.5).multiply(50.986)).add(1);
var Ct_ice_ri_negative = ct_ice_numerator.divide(ct_ice_denominator);

// Calculate Ct... If Ri > 0  lake

var Ct_lake_ri_positive_step1 = (lake_ri_positive.multiply(20)).add(1);
var Ct_lake_ri_positive = (Ct_lake_ri_positive_step1.pow(-2)).multiply(0.0013);

// Calculate Ct... If Ri > 0  slush

var Ct_slush_ri_positive_step1 = (slush_ri_positive.multiply(20)).add(1);
var Ct_slush_ri_positive = (Ct_slush_ri_positive_step1.pow(-2)).multiply(0.0013);

// Calculate Ct... If Ri > 0  ice
var Ct_ice_ri_positive_step1 = (ice_ri_positive.multiply(20)).add(1);
```

```
var Ct_ice_ri_positive = (Ct_ice_ri_positive_step1.pow(-2)).multiply(0.0013);

// Calculate sensible heat lakes (for both Ri positive and negative)

var sensible_heat_lakes_negative = sens_step2_lake.multiply(Ct_lake_ri_negative);
var sensible_heat_lakes_positive = sens_step2_lake.multiply(Ct_lake_ri_positive);
var visParamsRineg = {
  min: -64,
  max: 54,
  palette: ['green', 'yellow', 'red'],
};
var visParamsRipos = {
  min: -64,
  max: 54,
  palette: ['cyan','green'],
};

Map.addLayer(sensible_heat_lakes_negative, visParamsRineg,'sensible heat lakes negative RI');
Map.addLayer(sensible_heat_lakes_positive, visParamsRipos,'sensible heat lakes positive RI');

// Calculate sensible heat slush (assuming that Ct is generally negative)

var sensible_heat_slush = sens_step2_slush.multiply(Ct_slush_ri_positive);
Map.addLayer(sensible_heat_slush,visParams,'sensible heat slush');

// Calculate sensible heat ice (for both Ri positive and negative)

var sensible_heat_ice_negative = sens_step2_ice.multiply(Ct_ice_ri_negative);
var sensible_heat_ice_positive = sens_step2_ice.multiply(Ct_ice_ri_positive);

// Plot sensible heat for ice regions
Map.addLayer(sensible_heat_ice_negative, visParams,'sensible heat ice negative RI');
Map.addLayer(sensible_heat_ice_positive, visParams,'sensible heat ice positive RI');


// Calculate average sensible heat slush
var sensible_average_slush = sensible_heat_slush.reduceRegion({
  reducer: ee.Reducer.mean(),
  geometry: slushmask.geometry(),
  scale: 10,
  maxPixels: 1e9
});
print(sensible_average_slush, 'mean sensible heat slush');

// Calculate average sensible heat lakes
var sensible_average_lakes_negative = sensible_heat_lakes_negative.reduceRegion({
  reducer: ee.Reducer.mean(),
  geometry: lakemask.geometry(),
  scale: 10,
  maxPixels: 1e9
});
```

```
// Calculate average sensible heat lakes
var sensible_average_lakes_positive = sensible_heat_lakes_positive.reduceRegion({
  reducer: ee.Reducer.mean(),
  geometry: lakemask.geometry(),
  scale: 10,
  maxPixels: 1e9
});
print(sensible_average_lakes_positive, 'mean of sensible heat lakes positive');
print(sensible_average_lakes_negative, 'mean of sensible heat lakes negative');

// Calculate average sensible heat ice
var sensible_average_ice_negative = sensible_heat_ice_negative.reduceRegion({
  reducer: ee.Reducer.mean(),
  geometry: icemask.geometry(),
  scale: 10,
  maxPixels: 1e9
});

// Calculate average sensible heat ice
var sensible_average_ice_positive = sensible_heat_ice_positive.reduceRegion({
  reducer: ee.Reducer.mean(),
  geometry: icemask.geometry(),
  scale: 10,
  maxPixels: 1e9
});

print(sensible_average_ice_positive, 'mean of sensible heat ice positive');
print(sensible_average_ice_negative, 'mean of sensible heat ice negative');


////////// CALCULATE LATENT HEAT FLUX //////////////

var specific_hum_air = dataset.select(['specific_humidity_2m_above_ground']);
var visParams_wind = {
  min: 0,
  max: 0.03,
  palette: ['blue', 'purple', 'cyan', 'green', 'yellow', 'red'],
};
var listOfImages_humidity = specific_hum_air.toList(specific_hum_air.size());
var humidity_list = listOfImages_humidity.get(0);
var specific_hum_image = ee.Image(humidity_list);
Map.addLayer(specific_hum_image,visParams_wind,'specific humidity GFS');

var latent_step1 = wind_image.multiply(3188775);
var latent_step2_lakes = latent_step1.multiply(Ct_lake_ri_positive);
var latent_step2_lakes_negativeCt = latent_step1.multiply(Ct_lake_ri_negative);
var latent_step2_slush = latent_step1.multiply(Ct_slush_ri_positive);
var latent_step2_ice = latent_step1.multiply(Ct_ice_ri_positive);
var latent_step2_ice_negativeCt = latent_step1.multiply(Ct_ice_ri_negative);
```

```
// Create image array of constant value - use precipitation image

var specific_precip = dataset.select(['total_precipitation_surface']);
var visParams_wind = {
  min: 0,
  max: 627,
  palette: ['blue', 'purple', 'cyan', 'green', 'yellow', 'red'],
};
var listOfImages_precip = specific_precip.toList(specific_precip.size());
var precip = listOfImages_precip.get(3);
var precip_image = ee.Image(precip);
var image_253000000_constant = precip_image.multiply(0).add(253000000);

var entire_precip = dataset.select(['precipitable_water_entire_atmosphere']);
var visParams_wind = {
  min: 0,
  max: 627,
  palette: ['blue', 'purple', 'cyan', 'green', 'yellow', 'red'],
};
var listOfImages_entire = entire_precip.toList(entire_precip.size());
var precip_1 = listOfImages_entire.get(1);
var precip_image_1 = ee.Image(precip_1);
var image_5420_constant = precip_image_1.multiply(0).subtract(5420);

Map.addLayer(image_5420_constant, visParams);
Map.addLayer(image_253000000_constant, visParams);

// Calculate pv

var power_slush = image_5420_constant.divide(convert_irrad_slush);
var power_lake = image_5420_constant.divide(convert_irrad_lake);
var power_ice = image_5420_constant.divide(convert_irrad_ice);

var p_v_slush = image_253000000_constant.pow(power_slush);
var p_v_lake = image_253000000_constant.pow(power_lake);
var p_v_ice = image_253000000_constant.pow(power_ice);

// Calculate surface specific humidity (qs) (assume atmospheric pressure at sea level - 100 kPa)

var numerator_surface_humidity_lake = p_v_lake.multiply(0.622);
var numerator_surface_humidity_slush = p_v_slush.multiply(0.622);
var numerator_surface_humidity_ice = p_v_ice.multiply(0.622);

var denominator_surface_humidity_lake = (p_v_lake.multiply(-0.378)).add(1000000);
var denominator_surface_humidity_slush = (p_v_slush.multiply(-0.378)).add(1000000);
var denominator_surface_humidity_ice = (p_v_ice.multiply(-0.378)).add(1000000);

var qs_lake = numerator_surface_humidity_lake.divide(denominator_surface_humidity_lake);
var qs_slush = numerator_surface_humidity_slush.divide(denominator_surface_humidity_slush);
var qs_ice = numerator_surface_humidity_ice.divide(denominator_surface_humidity_ice);
```

```
// Final step to calculate latent heat

var latent_heat_lake = (specific_hum_image.subtract(qs_lake)).multiply(latent_step2_lakes);
var latent_heat_lake_negative =
(specific_hum_image.subtract(qs_lake)).multiply(latent_step2_lakes_negativeCt);
var latent_heat_slush = (specific_hum_image.subtract(qs_slush)).multiply(latent_step2_slush);
var latent_heat_ice = (specific_hum_image.subtract(qs_ice)).multiply(latent_step2_ice);
var latent_heat_ice_negative =
(specific_hum_image.subtract(qs_ice)).multiply(latent_step2_ice_negativeCt);

Map.addLayer(latent_heat_lake, visParams, 'latent heat lake');
Map.addLayer(latent_heat_slush, visParams, 'latent heat slush');
Map.addLayer(latent_heat_ice, visParams, 'latent heat ice');

// Calculate average latent heat lakes
var latent_average_lakes = latent_heat_lake.reduceRegion({
  reducer: ee.Reducer.mean(),
  geometry: lakemask.geometry(),
  scale: 10,
  maxPixels: 1e9
});
print(latent_average_lakes, 'average latent heat for lakes');

// Calculate average latent heat lakes negative Ct
var latent_average_lakes_negative = latent_heat_lake_negative.reduceRegion({
  reducer: ee.Reducer.mean(),
  geometry: lakemask.geometry(),
  scale: 10,
  maxPixels: 1e9
});
print(latent_average_lakes_negative, 'average latent heat for lakes with negative Ct');

// Calculate average latent heat slush
var latent_average_slush = latent_heat_slush.reduceRegion({
  reducer: ee.Reducer.mean(),
  geometry: slushmask.geometry(),
  scale: 10,
  maxPixels: 1e9
});
print(latent_average_slush, 'average latent heat for slush');

// Calculate average latent heat ice
var latent_average_ice = latent_heat_ice.reduceRegion({
  reducer: ee.Reducer.mean(),
  geometry: icemask.geometry(),
  scale: 10,
  maxPixels: 1e9
});

print(latent_average_ice, 'average latent heat for ice');
```

```
// Calculate average latent heat ice negative Ct
var latent_average_ice_negative = latent_heat_ice_negative.reduceRegion({
  reducer: ee.Reducer.mean(),
  geometry: icemask.geometry(),
  scale: 10,
  maxPixels: 1e9
});

////////////////// CALCULATE TOTAL SEB ////////////////// i.e sum of SW, LW, latent and sensible heat fluxes (average per pixel at 10m)

var SEB_lake1 = total_SW_lake.add(net_LW_lake_per_metre);
//var SEB_lake2 = sensible_heat_lakes_positive.add(latent_heat_lake); // excluded because negligible effect
//var SEB_lake3 = sensible_heat_lakes_negative.add(latent_heat_lake_negative); // excluded because negligible effect
var SEB_slush = total_SW_slush.add(net_LW_slush_per_metre);//.add(sensible_heat_slush).add(latent_heat_slush);
var SEB_ice = total_SW_ice.add(net_LW_ice_per_metre);

//// Calculate average SEB
var average_SEB_lake1 = SEB_lake1.reduceRegion({
  reducer: ee.Reducer.mean(),
  geometry: lakemask.geometry(),
  scale: 10,
  maxPixels: 1e9
});
//// Calculate sum SEB
var sum_SEB_lake1 = SEB_lake1.reduceRegion({
  reducer: ee.Reducer.sum(),
  geometry: lakemask.geometry(),
  scale: 10,
  maxPixels: 1e9
});

//// Calculate average SEB
// var average_SEB_lake2 = SEB_lake2.reduceRegion({
//   reducer: ee.Reducer.mean(),
//   geometry: latent_heat_lake.geometry(),
//   scale: 10,
//   maxPixels: 1e9
// });
//// Calculate average SEB
// var average_SEB_lake3 = SEB_lake3.reduceRegion({
//   reducer: ee.Reducer.mean(),
//   geometry: latent_heat_lake_negative.geometry(),
//   scale: 10,
//   maxPixels: 1e9
// });
//// Calculate average SEB
var average_SEB_slush = SEB_slush.reduceRegion({
```

```
  reducer: ee.Reducer.mean(),
  geometry: slushmask.geometry(),
  scale: 10,
  maxPixels: 1e9
});
//// Calculate sum SEB
var sum_SEB_slush = SEB_slush.reduceRegion({
  reducer: ee.Reducer.sum(),
  geometry: slushmask.geometry(),
  scale: 10,
  maxPixels: 1e9
});

// Calculate average SEB ice
var average_SEB_ice = SEB_ice.reduceRegion({
  reducer: ee.Reducer.mean(),
  geometry: icemask.geometry(),
  scale: 10,
  maxPixels: 1e9
});
// Calculate total SEB ice
var total_SEB_ice = SEB_ice.reduceRegion({
  reducer: ee.Reducer.sum(),
  geometry: icemask.geometry(),
  scale: 10,
  maxPixels: 1e9
});
print(average_SEB_lake1, 'mean SEB lakes');
print(average_SEB_lake2, 'total SEB lakes');
print(average_SEB_lake3, 'total SEB lakes');
print(average_SEB_slush, 'mean SEB slush');
print(sum_SEB_lake1, 'total SEB lakes');
print(sum_SEB_slush, 'total SEB slush');
print(average_SEB_ice,'mean SEB ice');
print(total_SEB_ice,'sum SEB ice');

//////////////////        END OF SURFACE ENERGY BALANCE MODEL 2020 ////////////////
```

Code (2) for calculating lake/slush extent based on PCA-histogram thresholds:

Sentinel-2 images*:* https://code.earthengine.google.com/a4aff4d14b437f4159d69d0a60887e46
Landsat 8 images: https://code.earthengine.google.com/0fa5a7d0f5462ff932d21d5a5394970d

Code (3) for calculating lake/slush extent based on blue-red normalised threshold (adapted from Arnold, 2019, code): https://code.earthengine.google.com/a4aff4d14b437f4159d69d0a60887e46

Code (4) for identifying minima and maxima of histograms in Python: contact author for text file.

Code (5) for calculating lake bottom albedo:

Landsat 8 images: https://code.earthengine.google.com/5b124e2db14998a99a03a0788853cfef
Sentinel-2 images: https://code.earthengine.google.com/6b03b35180ed061173a11163d4c30b64

8.3 Spectral Data Histograms

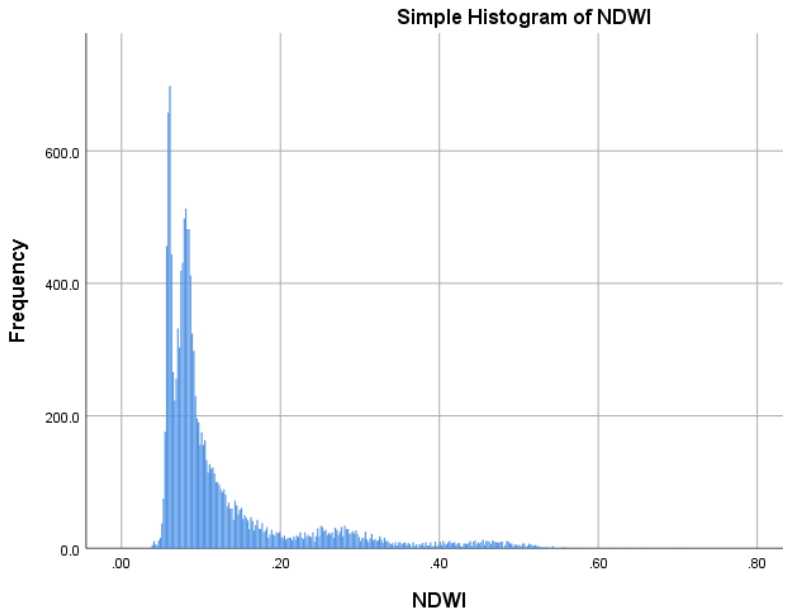

Figure S1. Blue (B2) to red (B4) NDWI ratio calculated for each pixel over the whole region from Sentinel-2 image captured on 31/01/2019. Pixel data binned into 400 bins. Distinct snow, slush and lake peaks can be identified with narrower bins. Positive tail indicates the presence of lakes and implies NDWIs of > 0.2.

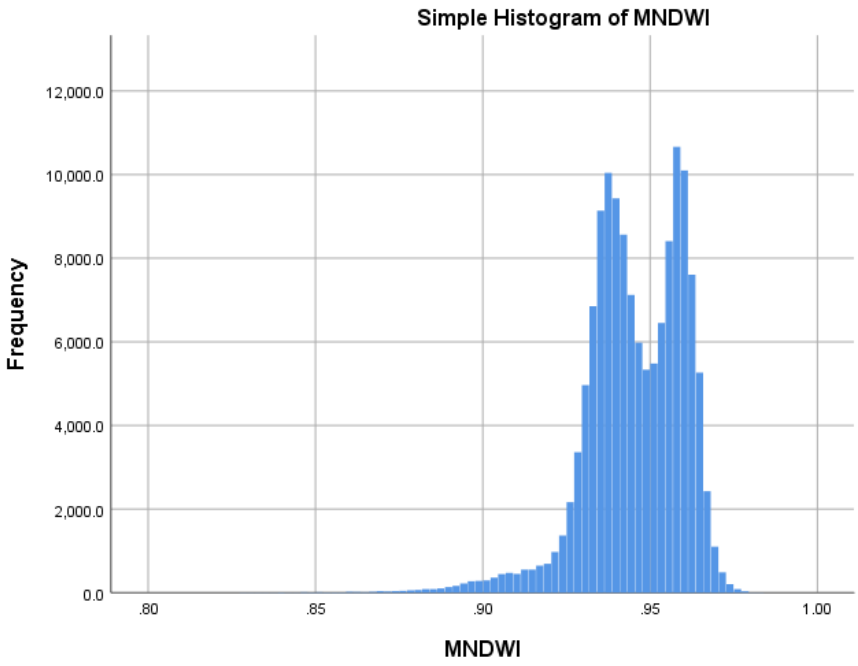

Figure S2. NIR (B8) to SWIR (B11) NDWI ratio calculated for each pixel over the whole region from Sentinel-2 image captured on 31/01/2019. Pixel data binned into 100 bins. Distinct lake and slush peaks calculated at 0.93 and 0.96 respectively. Lake peak not clearly identified.

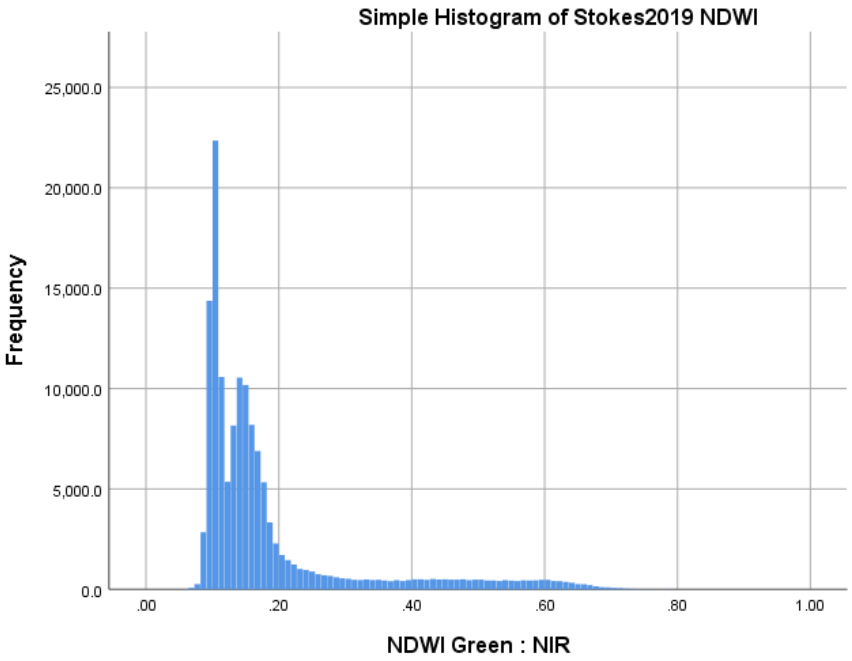

Figure S3. Green (B3) to SWIR (B11) NDWI ratio calculated for each pixel over the whole region from Sentinel-2 image captured on 31/01/2019. Pixel data binned into 400 bins. Distinct snow and slush peaks with positively skewed plateau indicating lake covered regions. Lakes with modified NDWI of > 0.3 which agrees with threshold applied by Stokes et al. (2019) for East Antarctica.

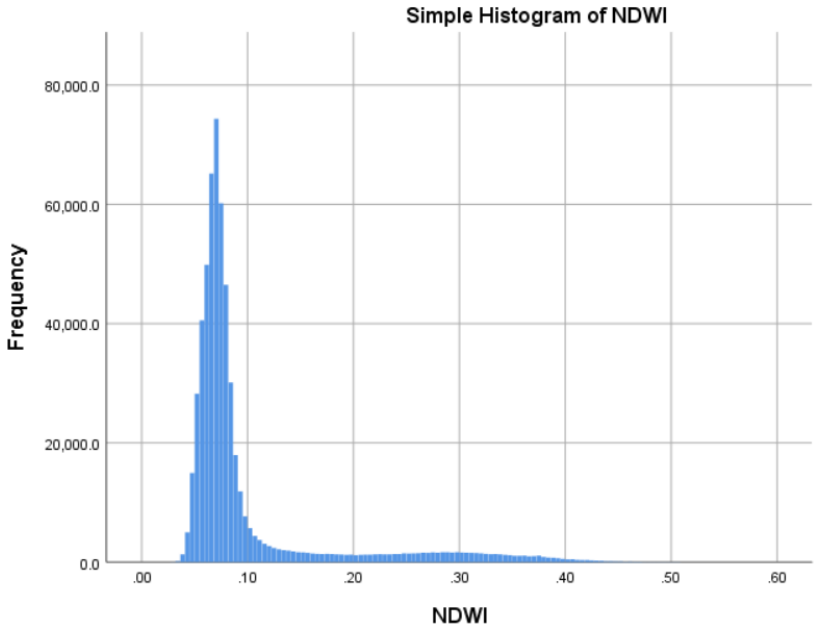

Figure S4. Blue (B2) to red (B4) NDWI ratio calculated for each pixel over the whole region from Landsat 8 image captured on 14/01/2020. Pixel data binned into 400 bins. Distinct snow, slush and lake peaks can be identified with narrower bins. Positive tail indicates the presence of lakes and implies NDWIs of > 0.3.

8.4 Pixel Training Data

	Pixel No.	Spectral Irradiance for Band (W/m^2)								
		B1	B12	B2	B3	B4	B5	B6	B7	B8
	11.38,-70.49, 11.39,-70.49									
Lakes	0	7052	35	6350	4611	2314	1820	1380	1283	1042
	1	7090	36	6416	4731	2579	2024	1550	1415	1192
	2	7185	33	6552	4805	2637	2136	1819	1579	1325
	3	7061	23	6283	4573	2256	1721	1343	1208	1010
	4	7013	46	6290	4713	2731	2303	1888	1793	1527
	5	7090	27	6476	4625	2161	1668	1181	1101	859
	6	7187	31	6609	4899	2752	2275	1819	1649	1387
	7	6995	38	6367	4624	2255	1782	1313	1218	981
	8	7069	27	6392	4529	2049	1522	1127	1011	820
	9	7125	29	6526	4901	2941	2455	2033	1860	1571
	10	6935	42	6197	4528	2445	2010	1654	1496	1264
	11	6982	26	6321	4521	2133	1620	1228	1100	905
	12	7013	38	6300	4577	2374	1851	1497	1339	1157
Slush	11.49,-70.50, 11.50,-70.49									
	13	8562	142	8287	7314	6950	6725	6498	6097	5615
	14	8527	124	8233	7247	6789	6528	6277	5863	5382
	15	8509	124	8213	7179	6675	6395	6172	5737	5285
	16	8556	127	8212	7112	6413	6121	5858	5406	4892
	17	8554	137	8257	7226	6714	6451	6208	5834	5328
	18	8537	124	8155	7134	6568	6298	6087	5634	5116
	19	8549	130	8192	7181	6657	6413	6174	5775	5259
	20	8537	122	8142	7076	6422	6143	5920	5411	4910
	21	8542	136	8187	7148	6528	6273	5997	5634	5120
	22	8521	128	8149	7061	6293	5974	5659	5175	4666
	23	8539	137	8241	7179	6566	6326	6076	5647	5095
	24	8554	124	8268	7238	6721	6479	6210	5765	5305
	25	8548	130	8260	7239	6759	6547	6260	5872	5344
	26	8549	134	8239	7172	6593	6275	6071	5563	5145
	27	8510	132	8181	7151	6569	6252	5973	5565	5102
	28	8499	126	8145	7090	6430	6110	5791	5356	4910
	29	8566	131	8272	7248	6755	6477	6238	5802	5357
Snow/Ice	11.28,-70.47, 11.29,-70.47									
	30	9153	200	8826	7894	7902	7757	7582	7183	6620
	31	9135	185	8808	7854	7810	7623	7460	7035	6500
	32	9134	188	8805	7862	7780	7576	7433	6980	6453
	33	9146	194	8823	7891	7854	7663	7516	7119	6567
	34	9154	194	8827	7906	7906	7731	7549	7148	6612
	35	9139	185	8751	7796	7723	7552	7361	6979	6392
	36	9143	187	8788	7822	7728	7558	7374	6935	6404
	37	9131	187	8770	7834	7760	7559	7429	6994	6447
	38	9146	179	8800	7844	7773	7600	7405	6992	6450
	39	9146	178	8811	7861	7813	7619	7479	7035	6492

40	9148	198	8823	7877	7844	7677	7494	7101	6542
41	9147	184	8791	7866	7808	7600	7439	7045	6503
42	9124	185	8804	7866	7794	7631	7458	7056	6490
43	9145	182	8795	7853	7809	7611	7468	7070	6505
44	9145	185	8785	7844	7813	7634	7469	7041	6468
45	9137	203	8821	7901	7870	7683	7530	7122	6580
46	9123	177	8817	7863	7794	7595	7421	7038	6465
47	9135	173	8776	7835	7754	7575	7376	6954	6426
48	9149	190	8801	7866	7827	7655	7478	7086	6544

Table S3. Spectral data for training pixels extracted from Sentinel-2 image captured on 31/01/2019. Supraglacial features were identified by manual delineation (Figures S5-9).

	Pixel No.	Reflectance					
		B2	B3	B4	B5	B6	B7
Lakes	0	0.697248	0.362151	0.102314	0.044137	0.008827	0.007496
	1	0.641583	0.289819	0.081273	0.043376	0.010425	0.008637
	2	0.64866	0.294652	0.08835	0.050681	0.01111	0.009626
	3	0.682714	0.354122	0.111902	0.057492	0.013203	0.011719
	4	0.685644	0.330037	0.11312	0.071342	0.017617	0.0156
	5	0.617574	0.239861	0.086067	0.055095	0.011339	0.010463
	6	0.649497	0.272013	0.088883	0.056389	0.01229	0.010654
	7	0.583862	0.217184	0.085991	0.055285	0.011529	0.009969
	8	0.663879	0.493382	0.299408	0.151397	0.029298	0.027624
	9	0.713457	0.508563	0.315541	0.185908	0.038277	0.036946
	10	0.717376	0.555364	0.414126	0.306028	0.057606	0.056693
	11	0.618487	0.450691	0.293662	0.187658	0.038239	0.03607
Slush	12	0.832627	0.702157	0.660265	0.571534	0.059356	0.058405
	13	0.853934	0.739939	0.7173	0.640289	0.059851	0.058748
	14	0.830268	0.670576	0.526522	0.323112	0.040256	0.038506
	15	0.824637	0.652959	0.481853	0.261435	0.036489	0.034739
	16	0.835443	0.685948	0.57397	0.391372	0.050986	0.047752
	17	0.806754	0.648355	0.509933	0.339588	0.053231	0.051633
	18	0.851842	0.711707	0.608366	0.440722	0.057758	0.054372
	19	0.853782	0.71361	0.637093	0.510808	0.070809	0.067689
	20	0.851728	0.722475	0.657792	0.583634	0.07568	0.073549
	21	0.838334	0.688764	0.562365	0.340577	0.038696	0.03687
	22	0.843281	0.703641	0.602963	0.440341	0.050719	0.047105
	23	0.851461	0.72784	0.670652	0.567654	0.056275	0.055361
	24	0.815162	0.645464	0.482538	0.276731	0.048436	0.045963
	25	0.825169	0.671033	0.532496	0.310024	0.050948	0.047637
Snow/Ice	26	0.980447	0.878933	0.870828	0.778217	0.059433	0.060802
	27	0.979801	0.885173	0.884298	0.813374	0.072598	0.075375
	28	0.927445	0.826691	0.820489	0.754056	0.072712	0.075641
	29	0.925695	0.821479	0.819119	0.763264	0.087931	0.089377

30	0.954802	0.849597	0.843167	0.769161	0.065825	0.067727
31	0.916944	0.813564	0.80428	0.738836	0.085458	0.085839
32	0.941181	0.842862	0.841606	0.791534	0.088654	0.091394
33	0.945709	0.840655	0.835861	0.753903	0.067423	0.06845
34	0.886733	0.773423	0.756567	0.684692	0.06963	0.069668
35	0.903284	0.79492	0.780538	0.714332	0.066091	0.067499
36	0.926532	0.816722	0.804014	0.727916	0.064379	0.064721
37	0.961423	0.860136	0.851005	0.773879	0.063884	0.065406

Table S4. Spectral data for training pixels extracted from Landsat 8 image captured on 14/01/2020. Supraglacial features were identified by manual delineation (Figures S5-9).

8.5 PCA and SEB Model Results and Validation

				GFS data			SEB model slush		SEB model lakes			
Date	Time	Timestamp	SW incoming	Air temp	Specific humidity	Wind speed	SW flux	LW flux	SW flux	LW flux	Air temp	LW flux
30/01/2019	00:00	2019/01/30/00/00	0	273.4	0.0032	3.87	0	-30.5	0	-12.6	273.4	-12.6
30/01/2019	06:00	2019/01/30/06/00	300	274.4	0.0033	2.35	73.2	-25.7	131.9	-8.1	274.4	-8.1
30/01/2019	12:00	2019/01/30/12/00	660	274.5	0.0038	1.36	154.3	-25.2	283.6	-7.5	274.5	-7.5
30/01/2019	18:00	2019/01/30/18/00	180	271.6	0.00277	2.11	42.9	-37.6	79.3	-19.9	271.6	-19.9
31/01/2019	00:00	2019/01/31/00/00	0	266.1	0.00137	2.69	0	-59	0	-41.1	266.1	-41.1
31/01/2019	06:00	2019/01/31/06/00	400	268.8	0.0019	1.65	94.1	-47.4	173.2	-29.9	268.8	-29.9
31/01/2019	12:00	2019/01/31/12/00	680	271.98	0.00279	-0.752	160	-35.5	294.8	-17.7	271.98	-17.7
31/01/2019	18:00	2019/01/31/18/00	180	268.2	0.00169	1.87	43.1	-50.9	79.5	-33.3	268.2	-33.3
01/02/2019	00:00	01/02/2019/00/00	0	264.7	0.001	1.79	0	-63.5	0	-45.9	264.7	-45.9
01/02/2019	06:00	01/02/2019/06/00	390	267.7	0.0017	2.34	93.2	-52	170.9	-34.5	267.7	-34.5
01/02/2019	12:00	01/02/2019/12/00	680	277.3	0.000022	-0.35	160	-45.3	294.9	-27.7	277.3	-27.7
01/02/2019	18:00	01/02/2019/18/00	180	266.3	0.0017	1.27	42.2	-58.1	77.8	-40.5	266.3	-40.5
10/01/2018	00:00	2018/01/10/00/00	40	264.8	0.0018	-1.07	9.4	-109.2	17.9	-55.7	264.8	-55.7
10/01/2018	06:00	2018/01/10/06/00	490	269.5	0.0025	-1.16	118.4	-90.9	220.7	-36.9	269.5	-36.9
10/01/2018	12:00	2018/01/10/12/00	760	272.8	0.0035	-0.16	170.1	-77.4	341.7	-24.2	272.8	-24.2
10/01/2018	18:00	2018/01/10/18/00	260	271.6	0.0029	0.18	63.1	-82.7	117.5	-29.3	271.6	-29.3
11/01/2018	00:00	11/01/2018/00/00	30	266.3	0.0018	1.21	7.3	-103.2	15	-48.6	266.3	-48.6
11/01/2018	06:00	11/01/2018/06/00	490	270.9	0.0026	-0.38	118.7	-85.2	220.3	-31.1	270.9	-31.1
11/01/2018	12:00	11/01/2018/12/00	760	272.9	0.0028	-0.57	184.1	-77.2	341.7	-25.1	272.9	-25.1
11/01/2018	18:00	11/01/2018/18/00	260	269.8	0.0025	0.56	63	-89.9	117.5	-37	269.8	-37
12/01/2018	00:00	2018/01/12/00/00	30	265.5	0.0015	1.25	7.3	-106.6	15	-52.5	265.5	-52.5
12/01/2018	06:00	2018/01/12/06/00	500	269.8	0.0022	0.32	120.4	-89.8	224.1	-35.6	269.8	-35.6
12/01/2018	12:00	2018/01/12/12/00	770	271.8	0.0024	-0.44	186.4	-81.9	346.3	-29.3	271.8	-29.3
12/01/2018	18:00	2018/01/12/18/00	260	268.4	0.0022	0.42	63	-95.2	117.5	-42	268.4	-42
25/01/2017	00:00	2017/01/25/00/00	0	260.8	0.001	-0.98	0	-116.1	0	-77.4	260.8	-77.4
25/01/2017	06:00	2017/01/25/06/00	430	265.4	0.0016	0.039	101.5	-94.5	188.4	-55.9	265.4	-55.9
25/01/2017	12:00	2017/01/25/12/00	710	270	0.0022	-1.09	168.6	-77.7	314.2	-39.5	270	-39.5
25/01/2017	18:00	2017/01/25/18/00	210	238.7	0.0011	-0.969	49.6	-121.4	93	-83.1	268.7	-83.1
26/01/2017	00:00	2017/01/16/00/00	0	262.3	0.0012	2.43	0	-107.4	0	-69.1	262.3	-69.1
26/01/2017	06:00	2017/01/16/06/00	430	265.7	0.0015	2.09	102	-94.9	190.2	-56.8	265.7	-56.8
26/01/2017	12:00	2017/01/16/12/00	710	271	0.0025	0.66	168.6	-74.1	314.7	-36.7	271	-36.7
26/01/2017	18:00	2017/01/16/18/00	210	267.8	0.0019	3.35	48.3	-86.8	91.8	-49.2	267.8	-49.2
27/01/2017	00:00	2017/01/27/00/00	0	267.1	0.0019	2.55	0	-89.6	0	-51.2	267.1	-51.2
27/01/2017	06:00	2017/01/27/06/00	330	268.7	0.0021	3.08	81.1	-83.9	151.4	-46.2	268.7	-46.2
27/01/2017	12:00	2017/01/27/12/00	710	270.5	0.0025	0.349	168.6	-76.4	314.7	-38.7	270.5	-38.7
27/01/2017	18:00	2017/01/27/18/00	210	267.3	0.0018	3.34	48.3	-89.1	91.8	-50.9	267.3	-50.9

Table S5. Meteorological data from Global Forecast System Data from day of Sentinel-2 image acquisition and one day either side. Cell highlighted green is the timestamp of GFS data closest to image capture. Sentinel-2 images selected to represent each year from 2017-2019.

			GFS data			SEB model slush		SEB model lakes	
Date	Time	Timestamp	SW incoming	Air temp	Specific humidity	SW flux	LW flux	SW flux	LW flux
13/01/2020	00:00	13/01/2020/00	30	266.3	0.0018	8.1	-100.5	11.8	-111.9
13/01/2020	06:00	13/01/2020/06	490	269.7	0.0025	129.8	-88.2	192.1	-99.6
13/01/2020	12:00	13/01/2020/12	760	272.1	0.0031	202.3	-78.3	299.9	-89.7
13/01/2020	18:00	13/01/2020/18	180	270.8	0.0029	47.2	-84.2	70.9	-95.7
14/01/2020	00:00	14/01/2020/00	20	269.7	0.0026	8.24	-88.5	8.24	-99.9
14/01/2020	06:00	14/01/2020/06	330	272.4	0.0032	134.5	-78.7	135.4	-90.1
14/01/2020	12:00	14/01/2020/12	620	273.2	0.0038	250	-74.3	250	-85.8
14/01/2020	18:00	14/01/2020/18	200	272.1	0.003	82.6	-79.8	82.6	-91.2
15/01/2020	00:00	15/01/2020/00	30	266.8	0.0017	11.8	-99.5	11.8	-110.9
15/01/2020	06:00	15/01/2020/06	480	270.9	0.0024	190.2	-84.8	190.2	-96.3
15/01/2020	12:00	15/01/2020/12	750	272.8	0.003	294.5	-76.6	294.5	-88.1
15/01/2020	18:00	15/01/2020/18	220	270.8	0.0022	86.7	-84.2	86.7	-95.6
24/01/2019	00:00	24/01/2019/00	0	261.1	0.0008	0.03	-63.1	0.61	-72.7
24/01/2019	06:00	24/01/2019/06	410	265.7	0.0015	113.4	-46.7	162.4	-56.3
24/01/2019	12:00	24/01/2019/12	720	269.4	0.0019	197.9	-32.4	283.8	-42
24/01/2019	18:00	24/01/2019/18	220	265.1	0.0015	59.1	-48.9	86.5	-58.6
25/01/2019	00:00	25/01/2019/00	0	262.1	0.001	0	-60.3	0	-69.9
25/01/2019	06:00	25/01/2019/06	440	265.8	0.0015	120.9	-46.7	173.7	-53.4
25/01/2019	12:00	25/01/2019/12	720	269.9	0.0022	197.9	-30.6	284.2	-40.2
25/01/2019	18:00	25/01/2019/18	190	267.7	0.0018	50.9	-39.2	73	-48.9
26/01/2019	00:00	26/01/2019/00	0	267.1	0.0015	0	-41.6	0	-51.3
26/01/2019	06:00	26/01/2019/06	320	268.9	0.0019	86	-34.5	127.7	-44.2
26/01/2019	12:00	26/01/2019/12	540	271.9	0.0025	149.5	-22.7	215.9	-32.3
26/01/2019	18:00	26/01/2019/18	140	270.8	0.002	38.5	-27.2	56.3	-36.9
07/01/2018	00:00	07/01/2018/00	40	265.5	0.0018	10.3	-80.1	17.8	-90.7
07/01/2018	06:00	07/01/2018/06	480	269.3	0.0026	117.4	-64.9	192.9	-75.5
07/01/2018	12:00	07/01/2018/12	740	272.8	0.0035	175	-52.6	302.4	-63.3
07/01/2018	18:00	07/01/2018/18	250	270.7	0.0029	58.6	-61.5	102	-72.1
08/01/2018	00:00	08/01/2018/00	40	265.3	0.0019	8.7	-79.9	15.9	-90.6
08/01/2018	06:00	08/01/2018/06	480	270.1	0.0027	177.8	-61.6	195.9	-72.2
08/01/2018	12:00	08/01/2018/12	760	272.8	0.0034	185	-51.9	307.4	-62.5
08/01/2018	18:00	08/01/2018/18	250	270.7	0.003	60.5	-60.7	102.5	-71.4
09/01/2018	00:00	09/01/2018/00	30	266.4	0.002	7.3	-77.66	13.5	-88.2
09/01/2018	06:00	09/01/2018/06	450	270.6	0.0027	106.2	-59.6	186	-70.3
09/01/2018	12:00	09/01/2018/12	760	272.9	0.0034	177	-50.2	305.3	-60.8
09/01/2018	18:00	09/01/2018/18	260	271.3	0.0032	61.7	-57.1	105.1	-67.7

Table S6. Meteorological data from Global Forecast System Data from one day either side of Landsat 8 image acquisition. Landsat 8 images are selected to represent each year from 2018-2020.

		Lake Extent (km^2)	
	Least cloudy image	PCA	NDWI
Sentinel-2	2017	50.3	32
	2018	68.9	49.4
	2018	8.4	3.4
	2019	29.3	11
	2019	89.4	33.9
Landsat 8	2016	20.8	7.9
	2017	105.2	37.5
	2018	78.4	67.8
	2019	45.9	30.3
	2020	88.2	44.7

Table S7. Comparison of lake area calculated using NDWI (threshold 3) and PCA-histogram method.

Image ID (COPERNICUS/S2/…)	Date	Area selected (co-ordinates)	Description	Figure
20190111T080929_20190111T080926_T32DNG	11/01/2019	11.645, -70.604, 11.798, -70.591	Lake/slush	S6a
20190111T080929_20190111T080926_T32DNG	11/01/2019	11.571, -70.524, 11.643, -70.505	Slush zone	S6b
20190111T080929_20190111T080926_T32DNG	11/01/2019	11.398, -70.533, 11.470, -70.511	Open water	S6c
20190131T080929_20190131T080941_T32DNG	31/01/2019	11.645, -70.604, 11.798, -70.591	Lake/slush	S7a
20190131T080929_20190131T080941_T32DNG	31/01/2019	11.398, -70.533, 11.470, -70.511	Open water	S7c
20190131T080929_20190131T080941_T32DNG	31/01/2019	11.571, -70.524, 11.643, -70.505	Slush zone	S7b
20181222T080929_20181222T080923_T32DNG	22/12/2018	11.376, -70.705, 11.448, -70.686	Open water	S8a
20181222T080929_20181222T080923_T32DNG	22/12/2018	11.638, -70.499, 11.710, -70.480	Slush zone	S8b
20180111T080921_20180111T080919_T32DNG	11/01/2018	11.643, -70.493, 11.715, -70.474	Open water	S9a
20180111T080921_20180111T080919_T32DNG	11/01/2018	11.499, -70.523, 11.571, -70.504	Slush zone	S9b
20170126T080921_20170126T080920_T32DNG	26/01/2017	11.746, -70.590, 11.826, -70.572	Open water	S10a
20170126T080921_20170126T080920_T32DNG	26/01/2017	11.779, -70.536, 11.859, -70.518	Slush zone	S10b

Table S8. Images selected from Sentinel-2 collection with polygons for manually delineated lake and slush areas defined. Figures refer to image cropped to area of interest and displayed with RGB bands in QGIS (Figures S5-9).

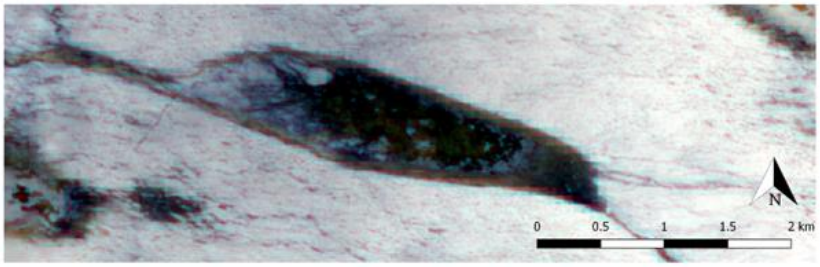

Figure S5a. Manually delineated lake with snow cover in Sentinel-2 RGB false colour image captured on 11/01/2019.

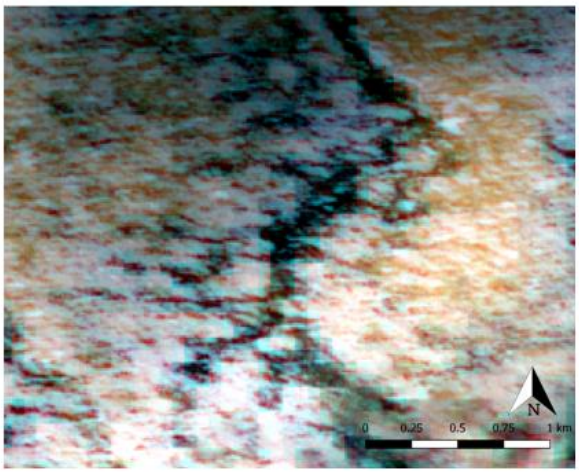

Figure S5b. Manually delineated slush region in Sentinel-2 RGB false colour image captured on 11/01/2019.

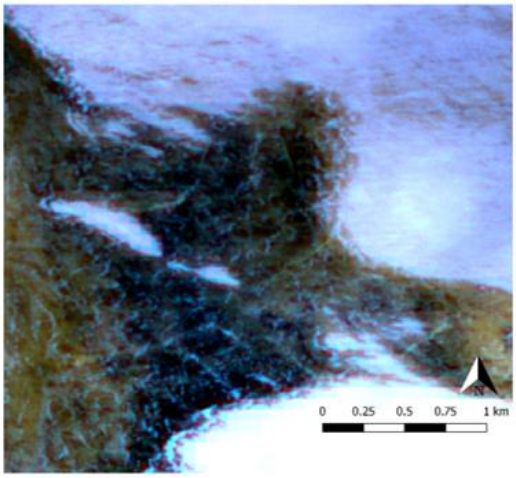

Figure S5c. Manually delineated open water lake in Sentinel-2 RGB false colour image captured on 11/01/2019.

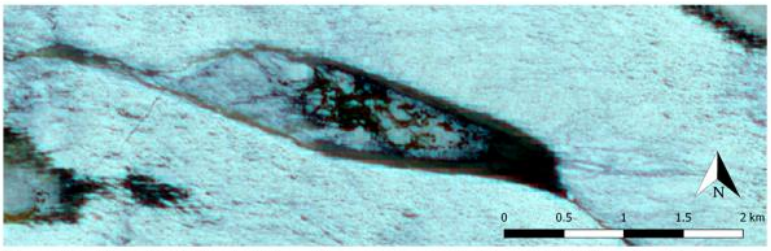

Figure S6a. Manually delineated lake with snow cover in Sentinel-2 RGB false colour image captured on 31/01/2019.

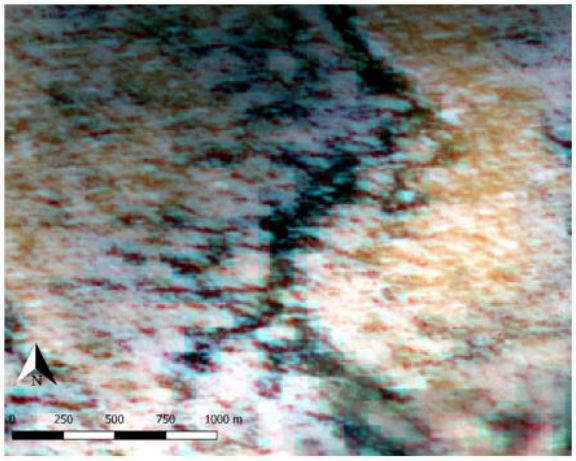

Figure S6b. Manually delineated slush region in Sentinel-2 RGB false colour image captured on 31/01/2019.

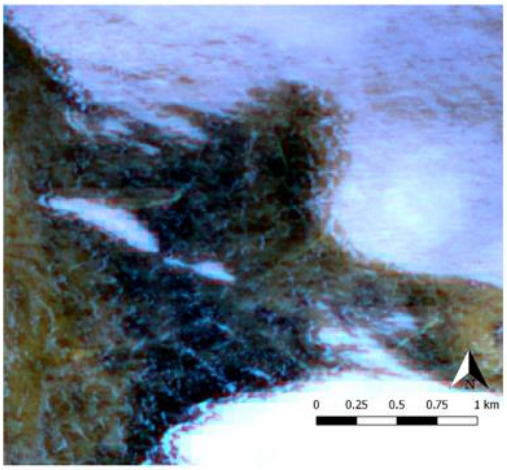

Figure S6c. Manually delineated open water lake in Sentinel-2 RGB false colour image captured on 31/01/2019.

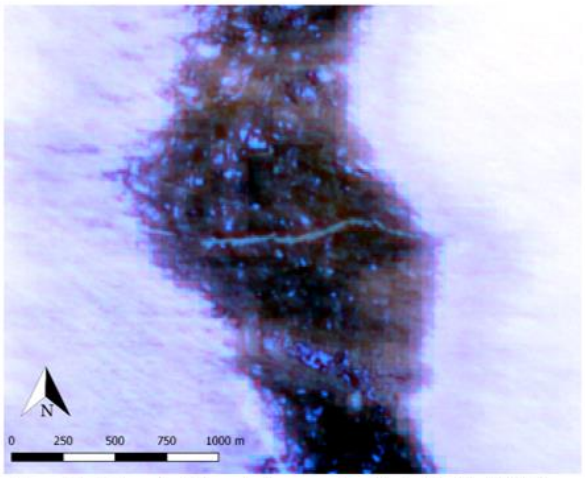

Figure S7a. Manually delineated open water lake in Sentinel-2 RGB false colour image captured on 22/12/2018.

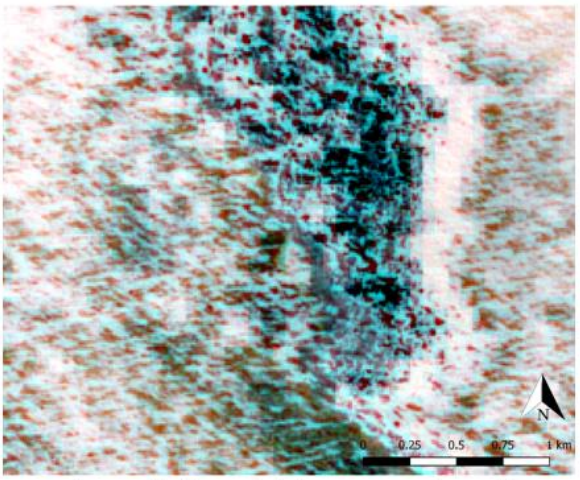

Figure S7b. Manually delineated slush area in Sentinel-2 RGB false colour image captured on 22/12/2018.

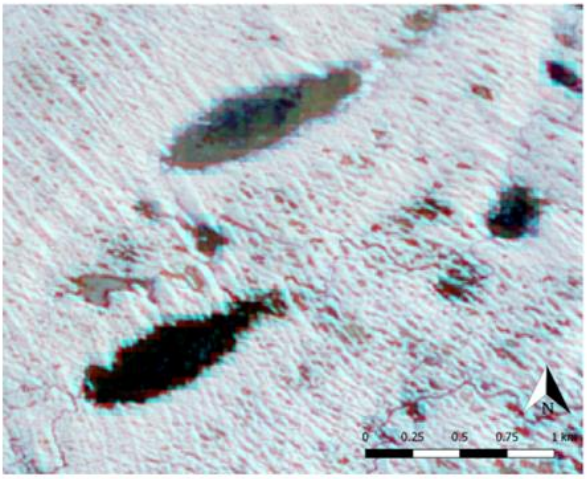

Figure S8a. Manually delineated open water lake in Sentinel-2 RGB false colour image captured on 11/01/2018.

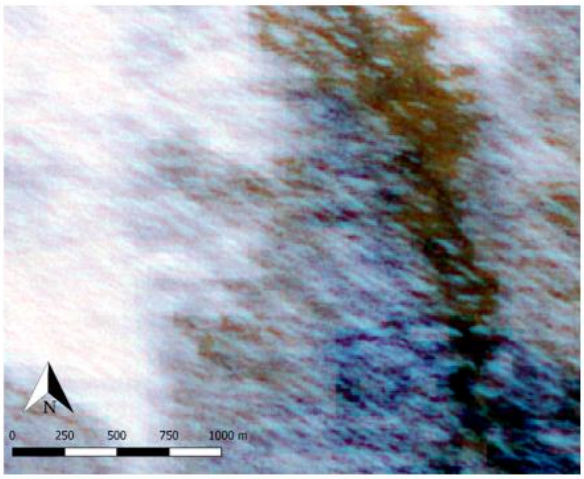

Figure S8b. Manually delineated slush area in Sentinel-2 RGB false colour image captured on 11/01/2018.

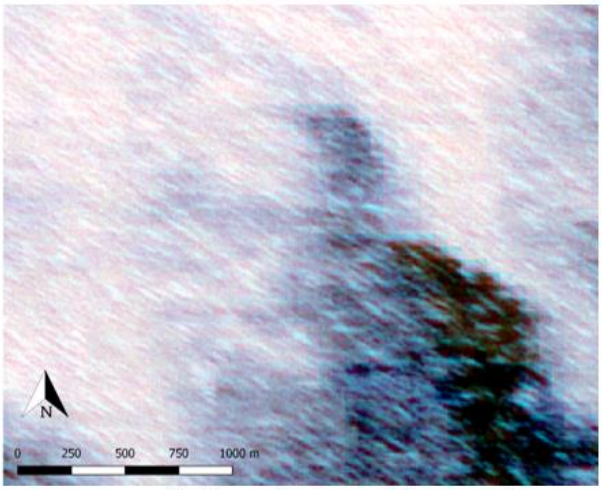

Figure S9a. Manually delineated open water lake in Sentinel-2 RGB false colour image captured on 26/01/2017.

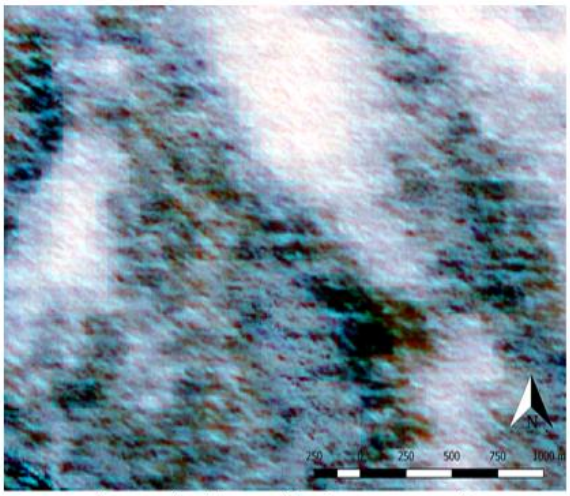

Figure S9b. Manually delineated slush area in Sentinel-2 RGB false colour image captured on 26/01/2017.

Image Date	Average Daily Lake SEB	Average Daily Slush SEB	Average Daily Ice SEB	Sum SEB Lake	Sum SEB Slush	Sum SEB Ice
01/11/2016	78.93	4.73	-69.17	181706072.9	-26051.4	-3553874327
02/11/2016	81.15	15.00	-81.03	199055290.8	-25725.8	-3729331351
03/11/2016	101.03	2.60	-88.33	161925220.7	471568.9	-976398515.4
03/12/2016	100.05	-2.18	-14.87	175448505.8	653060.575	-817193929
04/12/2016	90.00	-0.43	-9.20	166630624.7	543141	-915984798.1
05/12/2016	116.28	41.23	-12.73	194511611	881171.84	-1128625801
10/12/2016	126.73	56.63	-15.77	179658750	575127.475	-1258650201
11/12/2016	111.05	61.17	-21.07	199293009.2	888089.02	-1070223425
12/12/2016	68.90	54.37	-16.53	169898698.5	-9870460.45	-2676340529
19/12/2016	72.25	49.63	-63.40	168968321.9	-10107097	-2720309069
20/12/2016	116.85	51.73	-64.20	186337781.9	-9047978.55	-2601114479
21/12/2016	173.73	36.93	-60.17	435167133.1	12150928.25	-763703931.3
26/12/2016	150.75	38.37	-10.87	487832105.8	14634890.15	-381344157.6
27/12/2016	82.10	37.57	0.83	381582411.4	5078891.5	-527480526.3
28/12/2016	108.75	38.13	-2.60	382906023.5	-1114480.175	-1566890706
04/01/2017	101.30	36.30	-30.03	378715642.3	-991599.6	-1538031164
05/01/2017	135.13	30.00	-33.30	347972471.7	-2229743.45	-1649161043
06/01/2017	131.53	9.00	-38.13	470308312.7	4469664.375	-1406195123
11/01/2017	141.40	8.84	-28.47	447436955.2	1445903.4	-1659164540
12/01/2017	116.15	3.53	-40.40	490320054	9882553.07	-1088900359
13/01/2017	102.43	51.57	-22.17	586302144.7	-538274.15	-952903691.8
18/01/2017	98.30	72.70	-17.43	540469674	-3491532.2	-1031727980
19/01/2017	129.00	49.80	-19.93	519717295.5	-7418732.025	-1264026366
20/01/2017	95.38	31.20	-26.20	129209829.4	-23430689.78	-3726932414
25/01/2017	93.18	32.97	-68.43	146417048	-11537025.4	-3232719301
26/01/2017	100.13	26.73	-65.13	141011704.2	-10679682.35	-3108514674
27/01/2017	81.55	-24.93	-60.90	432823614.7	-17965132.75	-1261779955
03/02/2017	91.83	-34.63	-86.73	537187371	-17417065.28	-1111879668
04/02/2017	81.95	-34.27	-18.77	466077421.2	-18280184.55	-1316240087
05/02/2017	61.15	19.07	-26.83	367757139.4	-40270.84	-868738530.6
12/02/2017	47.58	64.60	-11.10	332144445.9	-41732.6	-1034816816
13/02/2017	73.50	65.63	-15.60	174310206.4	-69188.425	-1662269439
20/12/2017	140.10	74.20	25.07	243775726.2	5147673.025	-539144120.1
21/12/2017	144.45	77.23	21.53	240651380.1	4794017.475	-419889811.9
22/12/2017	80.85	77.97	22.47	247283334.8	5370635.15	-529088355.9
07/01/2018	123.18	19.77	-75.10	297473037.1	-134597552.7	-2957110535
08/01/2018	123.83	-5.97	-71.57	305694724.6	-128367763.2	-2851835964
09/01/2018	149.93	3.37	-72.73	302380829.8	-133302338.1	-2836605693
31/01/2018	46.23	-6.80	-58.10	95508181.83	-42188663.33	-2912007304
01/01/2018	50.08	-13.90	-54.83	105316740.4	-42852195.98	-2799838073
02/01/2018	95.90	-11.37	-58.37	105314302.1	-41937713.53	-2978003734
06/02/2018	75.93	-29.80	-74.80	128258194.4	-4488232.775	-2998291108
07/02/2018	75.75	-36.50	-77.60	132951775.7	-5033053.025	-3192855989
08/02/2018	51.18	-32.73	-79.13	113310505.1	-5387634.85	-3238108835

09/12/2018	27.20	-43.20	-88.80	179238.475	-15269875.94	-3692809372
10/12/2018	45.03	-47.90	-87.73	149980.65	-15800305.75	-3679255592
11/12/2018	63.15	-46.37	-79.40	286657.225	-10392709.3	-3302364498
21/12/2018	149.38	36.47	-41.37	41471993.03	144451864.7	-2148565660
22/12/2018	149.83	78.20	-44.03	42652225.68	145890601.2	-2257247828
23/12/2018	59.00	83.43	-46.43	42334924.89	146366553.3	-2241428240
23/12/2018	161.13	23.55	-18.07	188889346.3	2185010.925	-920236803.5
24/12/2018	159.15	-2.90	-6.83	200260215.9	3113416.148	-595373612.4
25/12/2018	150.63	-12.23	-11.03	194433312.9	2753104.825	-726945452
10/01/2019	12.38	-47.13	-129.73	1753852.05	-168543033.4	-6046060713
11/01/2019	11.88	-61.10	-117.50	17692194.05	-137647256.9	-5443084020
12/01/2019	104.63	-53.60	-123.33	-422962.65	-162857490.1	-5798707826
24/01/2019	111.40	-14.77	-17.07	424860437.3	-3089219.1	-881029056.8
25/01/2019	103.13	19.80	-19.50	435879822.3	-661350.15	-952572883.8
26/01/2019	24.75	16.97	-27.70	326206750	-7617512.6	-1191504504
30/01/2019	106.13	26.43	6.03	300585136.2	279124395.8	-120888981.1
31/01/2019	101.18	27.40	-6.47	286181115.5	120282823.7	-636970571.3
01/02/2019	97.83	23.23	-13.30	265660146.9	86600932.6	-939721164.6
18/02/2019	77.18	34.33	-56.57	73798.15	-317964.175	-992209932.4
19/02/2019	71.65	42.07	-48.40	78035.1	-203243.1825	-868261647.7
20/02/2019	106.05	48.40	-55.95	68104.775	-339351.725	-1001647450
24/11/2019	62.40	35.23	-37.93	46659198.34	202031.3375	-1828137498
25/11/2019	59.15	35.70	-39.10	44120965.18	69401.865	-1914416936
26/11/2019	61.23	28.03	-44.83	40959804.65	-250948.75	-2185073319
03/12/2019	86.38	43.10	-47.07	11441879.85	-637685.125	-2151985548
04/12/2019	80.50	64.73	-35.80	13834726.4	832364.9075	-1750800741
05/12/2019	68.85	50.97	-40.77	12193225.38	523553.925	-1864068375
10/12/2019	139.30	-3.17	5.13	113009406.2	1712555.125	-193773618.1
11/12/2019	139.33	-16.80	0.80	114388997.1	1551476.775	-358121788.4
12/12/2019	95.50	-12.77	1.93	114899945.7	1590465.7	-372660318.1
12/12/2019	141.10	35.83	16.23	224031608.9	4214131.118	234054669.8
13/12/2019	142.25	56.53	11.53	215280865.4	3452589.875	27333530.35
14/12/2019	141.45	58.77	15.87	219148476.3	4420803.35	229258019.5
28/12/2019	67.53	59.37	-16.60	201515642	-67489084.08	-1056265556
29/12/2019	67.78	60.20	-14.57	210354859.8	-61119138.58	-946325413.3
30/12/2019	128.79	58.33	-16.70	206348824.8	-64200215.43	-1003219642
13/01/2020	74.31	31.97	-71.50	219854331.4	-81719331.93	-1636999080
14/01/2020	88.08	12.90	-58.90	324213986.5	-48454183.77	-1445991737

Table S9. Average and net SEB model results for lake, slush and clean ice for each model run. Image dates correspond to Landsat 8 and Sentinel-2 image acquisition dates where < 20% cloud cover was found.

	Date for Cumulative Energy Calculation	Image ID for Lake Volume Calculation	Inferred Energy (J)	Cumulative Modelled Energy (J)
Landsat 8	13/02/2017	LANDSAT/LC08/C01/T2_TOA/LC08_166110_20170213	2595374324	422964962.9
	04/02/2017	LANDSAT/LC08/C01/T2_TOA/LC08_167110_20170204	3017049206	1641747149
	08/01/2018	LANDSAT/LC08/C01/T2_TOA/LC08_165110_20180108	2120028928	522277526.7
	07/02/2018	LANDSAT/LC08/C01/T2_TOA/LC08_167110_20180207	1309112202	465633619.3
	19/02/2019	LANDSAT/LC08/C01/T2_TOA/LC08_166110_20190219	3494263916	743139648.2
	14/01/2020	LANDSAT/LC08/C01/T2_TOA/LC08_165110_20200114	1936382291	1058112150
Sentinel 2	26/01/2017	COPERNICUS/S2/20170126T080921_20170126T080920_T32DNG	6880876877	1136679213
	11/01/2018	COPERNICUS/S2/20180111T080921_20180111T080919_T32DNG	9118001284	808004393.5
	22/12/2018	COPERNICUS/S2/20181222T080929_20181222T080923_T32DNG	449548085.7	1180446.7
	11/01/2019	COPERNICUS/S2/20190111T080929_20190111T080926_T32DNG	2001844240	399135379.7
	31/01/2019	COPERNICUS/S2/20190131T080929_20190131T080941_T32DNG	9140319035	1216075059

Table S10. Inferred energy (J) from peak lake volume at the end of each austral summer and cumulative modelled energy (J) calculated for whole lake region. Inferred energy derived from lake volume calculated from images listed. Cumulative energy calculated across total lake area summed up until same image date as used for lake volume derivation.